KU LEUVEN

FACULTY OF SCIENCE

# Towards Alpha Dosimetry with Laser Ionized and Mass Separated $^{225}$Ac:

## Setup Development and Source Characterization



**Viktor VAN DEN BERGH**

Thesis presented in fulfillment of the requirements for the degree of Master of Science in Physics

Supervisor: Prof. T.E. Cocolios
Institute for nuclear and radiation physics

Mentor: J.D. Johnson
Institute for nuclear and radiation physics

Academic year 2021-2022

# Acknowledgements

When I started my education in physics, I had no clue about where I would end up. Despite my unwavering interest and motivation over the years, there was never a real passion for what I was studying. But thanks to the people around me this past year, I have finally found a goal worth pursuing. This is their story, as much as it is mine, and I will be forever indebted.

First, I would like to offer my greatest thanks to Thomas E. Cocolios. Despite his insane schedule, he always found the time to help me in my endeavours, no matter how small. Moreover, his (sometimes pushy) encouragement helped me to present the best possible version of my research. What started as vague drawings on a chalkboard and lots of hand gesturing culminated in my perhaps proudest achievement. I would not be where I am today without the many opportunities he has granted me. Of course, as a professor, he could not hold my hand ALL the time.
Hence, I would like to thank Jake D. Johnson. As my mentor, he was by my side every step of the way. He and the many other people at the IKS in Leuven gave me not only a workspace to go to, but more importantly, a home.

I would be amiss if I didn't mention the contributions of professor Carmen Bartic, Olivier Deschaume and Lens Dedroog of the KU Leuven Laboratory of Soft Matter and Biophysics. Their work was the inspiration for large parts of this thesis, and it couldn't have been realized without their expertise. Thank you, Olivier and Lens, for all the work put into sample preparation. I'm also very grateful for the work done by Philippe Mispelter of the mechanical workshop and Ludwig Henderix in manufacturing of the DIRAC setup and the sources used in cell irradiations.

The past year has been a rollercoaster with many ups and downs, especially during the first semester when I suffered from persistent illnesses. Therefore, I would like to thank all the people who were there to pick me up when it was needed. Special thanks go to our cat Moustache and also to my housemates Ian and Nando for being my home away from home. Of course, these thanks also extend to all the friends whose support kept me going throughout the year. Finally, I will never be able to repay the debt to my parents and family for giving me the opportunity to do what I love. They have been there for me, unconditionally, ever since my first day on this spinning ball.

Thank you, everyone, for turning my life around and giving me the motivation to go beyond my limits.

# Abstract

Metastatic cancers are responsible for ∼90% of cancer-related deaths. Yet when patients are faced with metastasis, they often have little choice but to resort to chemotherapy. A possible alternative can be found in targeted therapies. In these, radionuclides are chelated to vector molecules, designed to bind with cancer cells. Since 2013, Targeted Alpha Therapy (TAT) has become a clinical reality with the approval of the first alpha-emitting radiopharmaceutical, Xofigo$^{TM}$[1]. Thanks to the alpha-particle's short path length (<100$\mu$m) and high energy (4-10 MeV), TAT is particularly appropriate for targeting distributed cancers[2]. A promising radionuclide for TAT, $^{225}$Ac, is currently under clinical investigation yet supply issues persist. Furthermore, the radiobiological effects of alpha particles are still not fully understood.

To respond to supply shortages, a new, accelerator-based production route for $^{225}$Ac is being explored. In this method, high energy (>70 MeV) protons are used to induce spallation reactions on solid uranium or thorium-based targets. Afterwards, produced isotopes can be extracted and purified via laser ionization and mass separation. A sample from CERN-MEDICIS which was produced using this technique was characterized. End Of Collection (EOC) activity was obtained via $\gamma$-$\gamma$ coincidence measurements and compared to in-target yields. Furthermore, suitability for medical applications was investigated by determining the suppression factor of $^{227}$Ac via alpha spectroscopy. An EOC activity of 201 kBq was achieved for a target of 4.52 MBq, resulting in a collection efficiency of 4.44 %. The activity of $^{227}$Ac on the sample was estimated to be 0.080 Bq or $5.8 \times 10^{-5}$ % of the $^{225}$Ac activity based on preliminary analysis.

One of the main reasons that microbiological effects of alpha particles are poorly understood is the lack of precise and accessible research methods[3]. To this end, DIRAC, a setup for the irradiation of cells with alpha particles was developed. Exploiting the properties of cells suspended in a hydrogel, it can irradiate cells with access to neither radiopharmaceuticals nor specialized equipment. Simulations were performed in Geant4 to investigate the feasibility of the technique and a protocol for cell irradiation was developed. Proof of concept was then achieved over an experimental campaign where HeLa cancer cells were irradiated by sources of $^{225}$Ac and $^{241}$Am. Life/death assays using fluorescence microscopy confirmed the response of cancer cells to radiation. To the author's knowledge, DIRAC is the first-ever setup to use this technique exploiting hydrogels in conjunction with alpha radiation. Its success can provide useful radiobiological data for the development of TAT. Further investigation and development of this technique is thus warranted.

# Summary for General Audience

The term 'nuclear radiation' is often associated with nuclear weapons or catastrophes. Images of the Chernobyl disaster and the result of the atomic bombs dropped on Hiroshima and Nagasaki are burned into the collective memory. But in truth, it can be found all around us in the form of background radiation. However, nuclear radiation can still be extremely harmful when you are exposed to high amounts, especially when directed at vital organs. But what if instead of damaging the body, these radioactive properties could be used to kill harmful cells within the body?

Medical experts have tried to use nuclear radiation to treat cancer ever since the discovery of X-rays in 1896. In modern medicine, its application is mostly found in external beam therapy. These treatments irradiate tumors with a beam of for example protons from outside of the body. The downside is the fact that to reach a tumor, particles have to pass through healthy tissue, potentially damaging it. Beam therapy is also limited to one region and can thus not be used to treat metastatic cancers, where tumors fragment and spread throughout the whole body. These metastatic cancers are responsible for $\sim$90% of cancer-related deaths. Yet when faced with metastasis, patients often have little choice but to resort to chemotherapy.

In an effort to overcome these challenges, scientists have been researching new nuclear treatments in the form of targeted therapies. In these, unstable, radioactive nuclei are attached to so-called 'targeting vectors'. These are special molecules, designed to stick to a specific type of cancer cell if they encounter them in the body. When the unstable nucleus then decays, it emits the radiation right next to the cell, killing it in the process. The targeted nature of those treatments means that even if the location of cancer cells is unknown, the radioactive nuclei can get to them and kill them, without damaging healthy cells.

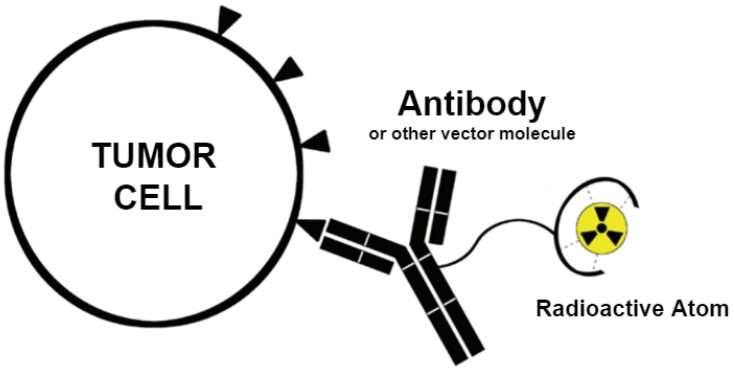


[4]

The slowest and heaviest form of conventional nuclear radiation comes from alpha decay. Particles emitted in this process consist of 2 neutrons and 2 protons, equivalent to the nucleus of a helium atom. Their large size and mass mean that they can be easily stopped in the body, with path lengths as small as the width of a human hair. While they can not penetrate even our skin, alpha particles are extremely deadly to cancer cells when emitted in close proximity via targeted therapy. Because they are so easily stopped, they also leave healthy tissue unharmed if administered correctly. This form of Targeted Alpha Therapy or TAT is still in its infancy, with only one treatment using alpha particles approved for medical use so far. Currently, there is an insufficient and limited supply of suitable nuclides for TAT. Moreover, the biological effects of alpha particles are still not fully understood, mainly due to a lack of precise and accessible research methods.

A promising type of radioactive nuclide for TAT, $^{225}$Ac, is currently under clinical investigation. While the initial response in patients is spectacular, the current production routes for the material are insufficient for widespread adoption. One of the methods proposed to increase production is by the use of particle accelerators. In this work, a sample of $^{225}$Ac produced in this way was analyzed. The gathered data provides insight into the performance of the method used to collect the nuclide. Furthermore, a setup for the irradiation of cancer cells with alpha particles was developed. Proof of concept for this setup and a novel way to study the effect of alpha radiation on cells is presented.

# List of Symbols and Abbreviations

| | |
|---|---|
| A | Atomic mass number |
| ADC | Analog to Digital Converter |
| AML | Acute Myeloid Leukemia |
| ASET | Alpha Setup |
| CERN | European Organization for Nuclear Research |
| DAS | Digital Acquisition System |
| EBRT | External Beam RadioTherapy |
| EOC | End Of Collection |
| GANIL | Great National Heavy Ion Accelerator |
| GEANT4 | Geometry And Tracking 4 software package |
| HPGe | High Purity Germanium |
| ISOLDE | Isotope Separation On-Line Device |
| mCRPC | Metastatic Castrate Resistant Prostate Cancer |
| MEDICIS | Medical Isotopes Collected from Isolde |
| PRISMAP | PRoduction of high purity Isotopes by mass Separation for Medical Application |
| PSA | Prostate-Specific Antigen |
| PSMA | Prostate-Specific Membrane Antigen |
| SRIM | Stopping Range of Ions in Matter software package |
| $T_{1/2}$ | Half-life |
| $\sigma$ | Gaussian standard deviation |
| $\lambda$ | Nuclear decay constant |
| eV | Electronvolt |

# Contributions

Many people helped in the realization of this thesis. Their contributions as well as those of the author Viktor Van den Bergh will now be listed.

**Measurements:**
Measurements in chapter 3 were completed by Jake Johnson (JJ). All other measurements in this work were performed by Viktor Van den Bergh (VVdB) under the supervision of JJ.
**Data analysis, Image analysis and Simulations:**
All data analysis in the work was performed by VVdB with the exception of chapter 3 and the EOC fit in chapter 2, where analysis was done by JJ. All image analysis from fluorescent and confocal microscopy was performed by VVdB. All simulations with the SRIM and Geant4 software packages were performed by VVdB.
**Sample preparation:**
All gel samples used in irradiation experiments were prepared by Olivier Deschaume (OD) and Lens Dedroog (LD) of the KU Leuven Laboratory of Soft Matter and Biophysics.
**Microscopy:**
The first 5 out of 20 microscopy sessions were performed by LD with VVdB in attendance. All microscopy afterwards was performed by VVdB. The imaging session with the Confocal microscope was performed by LD with VVdB present.
**Setup Development:**
The design and 3D model of the DIRAC setup were made by VVdB. Technical drawings and manufacturing were completed by the mechanical workshop of the KU Leuven Department of Physics and Astronomy.
**Cell irradiation experiments:**
All cell irradiations were performed by VVdB under the supervision of JJ.

**Extra notes:**
Chapter 2.3 made heavy use of code written by Michael Heines (MH) of the KU Leuven Institute for Nuclear and Radiation Physics (IKS). MH also offered technical support in its operation.

# Contents

# Chapter 1

# Introduction

There have been medical applications of ionizing radiation ever since its discovery. The first-ever radiotherapy treatment already took place on the 29th of January 1896, a mere 3 days after the announcement that X-rays were discovered[5]. What followed were decades where radioactive materials were recklessly applied to everything from cancers to afflictions of the skin. A lack of understanding regarding the biological effects often made these efforts cause more harm than good. Nevertheless, treatments evolved together with scientific understanding.

Today, ionizing radiation is an important tool in cancer treatments. The most common use comes in the form of External Beam RadioTherapy or EBRT. In these treatments, a beam of photons, electrons or protons is applied to a tumor from outside the body. The resulting therapeutic effect has seen success over time with demand surging in recent years. Especially proton therapy has seen a lot of growth due to its safer and more precise dose targeting[6]. However, despite advancements and the growing importance of EBRT, it still faces two inherent limitations.

First of all, there is the nature of these beams themselves. Even with advancements like proton therapy, radiation inevitably has to pass through healthy tissue. While tuned to deposit the majority of energy in the tumor, damage is still done on its way there and to the surrounding tissue. Depending on where the tumor is located, this limits the dose that it can be given before a patient is put at risk. Secondly, treatment is limited to only one area. When parts of a tumor break off and spread throughout the body, it is called metastasis. These metastatic cancers are responsible for $\sim$90% of cancer-related deaths. A number that has seen little change over time[7]. When faced with metastasis, patients often have little choice but to resort to more traditional treatments like chemotherapy. The limited therapeutic effects and harm done by these in the process urged the development of new treatments.

A promising solution was found in the form of targeted therapies. Instead of using a beam from outside of the body, patients are injected with radioactive isotopes that are left to decay in the body. To make sure that this decay only happens in the vicinity of tumors, the radioactive element is attached to a targeting vector. These can be biomolecules like antibodies, designed to attach to cancer cells when encountered. Molecules called chelating agents serve as the glue to bind the two parts together. A visual repre-

sentation of such a system is shown in figure 1.1. As these targeting vectors traverse the body, they attach to cancer cells after which the radioactive isotope can decay in close proximity. This allows targeted therapies to selectively treat metastatic cancer and it thus offers a clear advantage over the likes of chemotherapy and EBRT.

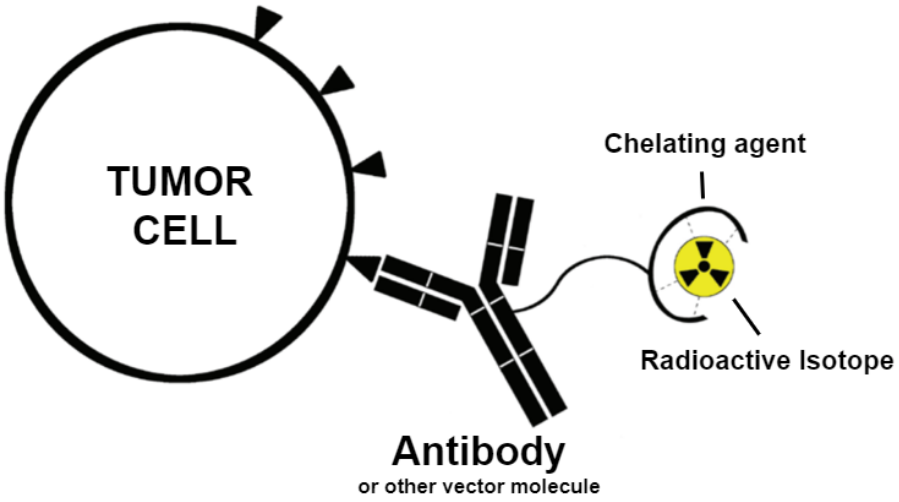


Figure 1.1: Graphical representation of a targeted radiopharmaceutical attached to a tumor cell via an antibody vector molecule[4].

This work will focus on Targeted Alpha Therapy (TAT), where the radioactive isotope used is an alpha emitter. The physical properties of alpha radiation are well matched to satisfy the criteria of effective targeted therapies. Their short path lengths in water ($<$100 μm) leave healthy tissue untouched if administered correctly. Moreover, they are very energetic (4-10 MeV) which results in large, localized energy deposits with low quantities of radionuclides. Despite these attractive properties, only one radiopharmaceutical has been approved for medical use. Namely Xofigo$^{TM}$, which uses the alpha emitter $^{223}$Ra. This is not due to a lack of demand or efficacy, but rather a supply problem. To understand why, a closer look at the nuclear chart is warranted.

To be eligible for TAT, an isotope generally needs three things. First of all, it needs to have substantial alpha branching. This means that one generally has to look at heavy (A$>$200) nuclei. Secondly, an appropriate half-life is required for medical application. This usually means a half-life in between half an hour and 20 days. Last of all, the isotope needs a plausible production route. When all of these criteria are considered, only a handful of isotopes are currently eligible. Most of these situate themselves in one 'goldilocks' zone on the nuclear chart between $^{223}$Ra and $^{230}$U. This zone and some candidates for TAT are shown in image 1.2 but it is not an exhaustive list.

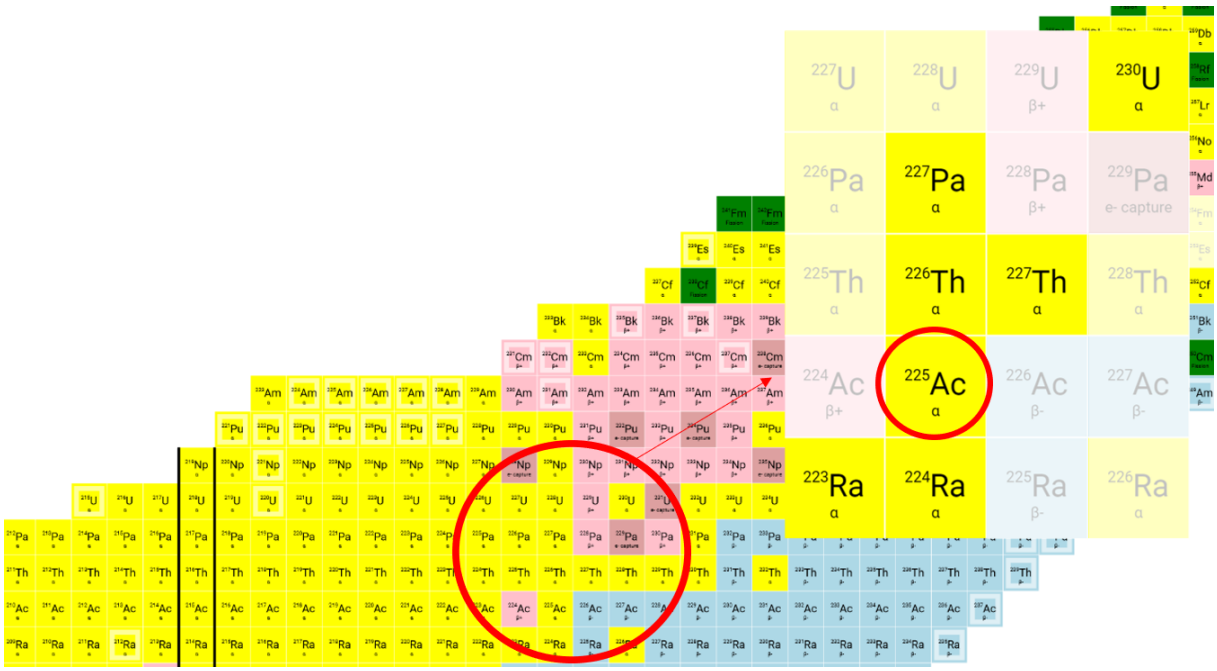


Figure 1.2: The 'goldilocks' zone with 7 radionuclides eligible for TAT. Image adapted from [8].

None of the eligible isotopes, nor generators of them occur naturally in medically relevant quantities. This means they have to be synthesized before being used in medical applications. It is this production process that is delaying the development and widespread adoption of TAT radiopharmaceuticals. In this work, the focus will be on the promising isotope $^{225}$Ac and the feasibility of a new production route.

Another bottleneck in the development of TAT is the poor understanding of the micro radiobiological effects of alpha radiation[2]. This primarily stems from a lack of accurate and accessible research methods. In this work, DIRAC, a new setup for in vitro alpha dosimetry studies was developed and tested. Exploiting the properties of collagen-based hydrogels in conjunction with DIRAC, a novel way of irradiating cells with alpha particles will be presented.

# Chapter 2

# Alpha Emitters for Targeted Alpha Therapy: Overview

Multiple radionuclides are currently under investigation for TAT. Of these, the focus of this work will be on the promising radionuclide $^{225}$Ac. The decay chain for this isotope is shown in figure 2.1.

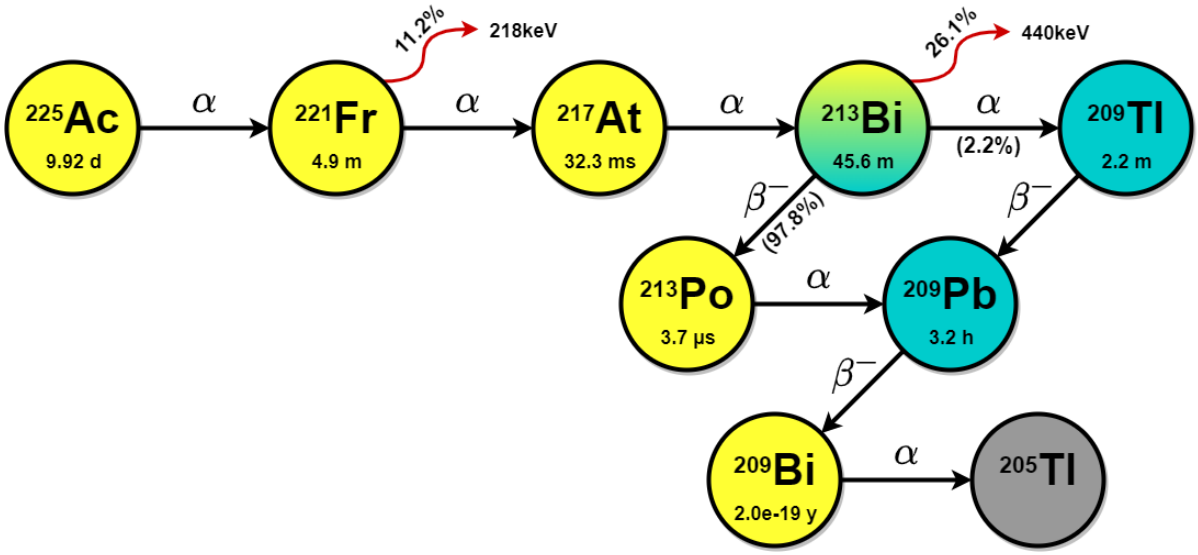


Figure 2.1: Decay chain of $^{225}$Ac color coded in yellow, blue,red and gray for $\alpha$ decay, $\beta^-$ decay, $\gamma$ decay and stable elements respectively. Half-lives are indicated in the bottom. The 2 shown $\gamma$ emissions have been visually indicated because of their importance in medical imaging techniques.

First of all, there is the half-life of $T_{1/2} = 9.92$ days[9]. One of the most common targeting vectors for TAT are antibodies. These are relatively large molecules that can take hours to diffuse throughout the body and can circulate for days [10]. The half-life of $^{225}$Ac complements this, being long enough for administration and diffusion, yet short enough that substantial amounts can decay before being excreted.

Secondly, there is the matter of the decay chain itself. As can be observed, daughter isotopes of $^{225}$Ac are relatively short-lived. Combining the predominant alpha decays

from the daughter isotopes $^{221}$Fr ($T_{1/2}$ = 4.9 minutes)[11] , $^{217}$At ($T_{1/2}$ = 32.3 ms)[12] and $^{213}$Po ($T_{1/2}$ = 3.7 µs)[13], 4 alpha particles with a cumulative energy of 28 MeV are emitted. Multiple alpha decays per nucleus make the emitted radiation from $^{225}$Ac highly cytotoxic. Capable of depositing large amounts of energy in low doses. Additionally, 2 beta particles with $Q_\beta$'s of 1.6 and 0.6 MeV are released by $^{213}$Bi and $^{209}$Pb[14] respectively.

Technically speaking, the end of the chain is the stable isotope $^{205}$Tl. But with a half-life of $2 \cdot 10^{19}$ or 20 quintillion years, $^{209}$Bi is stable for all practical purposes[14]. Finally, it is worth mentioning that there are 2 gamma decays in the $^{225}$Ac decay chain that are intense enough for in vivo medical imaging. One in $^{221}$Fr(218keV) with an emission probability of 11.2% and one in $^{213}$Bi(440keV) with an emission probability of 26.1% , indicated in red on figure 2.1.

These selectively destructive properties make $^{225}$Ac an attractive candidate for TAT although they can pose problems as well. Significant challenges still need to be overcome before widespread adoption of TAT and $^{225}$Ac can be achieved. A non-exhaustive list of the most pressing issues includes[15]:

- Retention of recoiling daughters
- Unwanted non-targeted effects
- Production and procurement of isotopes
- Waste handling implications due to impurities in production routes

The retention of daughter nuclei will be discussed first. When a nucleus decays, it emits an alpha particle at an energy between 4-10 MeV. Due to the laws of conservation of momentum and total energy, it induces a recoil in the parent nucleus as illustrated in figure 2.2. In the A$\sim$200 regime, the recoil is of the order of 100 keV which far exceeds the electrostatic potential energies of chemical bonds (E $\sim$ 1 eV). Meaning that while $^{225}$Ac is in the body, its recoiling daughter nuclei have sufficient energy to overcome the binding potential of the chelating agent. This causes the biodistribution of these nuclei to no longer be defined by the targeting molecules. In turn, they will decay and deposit energy in healthy tissue. Especially concerning in this regard is $^{213}$Bi which has a tendency of accumulating in the kidneys[16]. An effective chelating agent that leads to a stable complex that can contain recoils is necessary to counteract these effects. Unfortunately, this task is far from trivial and research is still ongoing to date [17] [18].

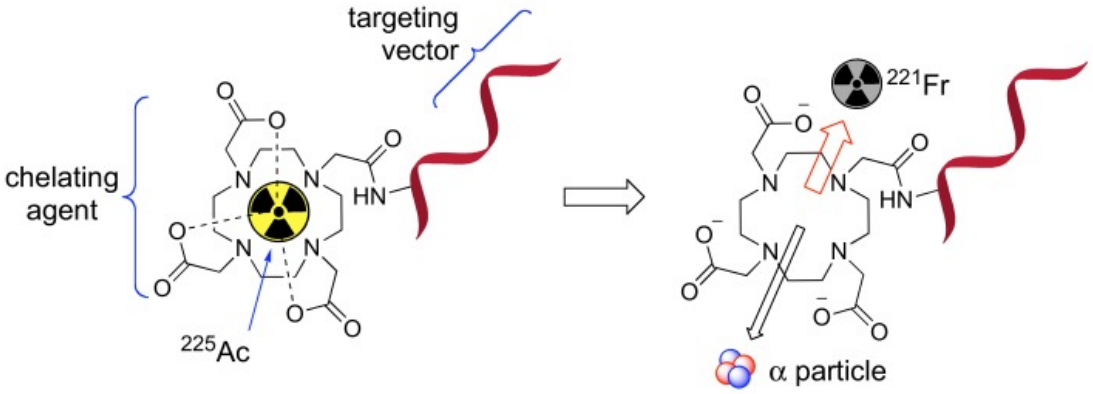


Figure 2.2: Illustration of the recoil from $^{225}$Ac after alpha decay. $^{221}$Fr overcomes the binding energy of the chelating agent in opposite direction relative to the alpha particle and is now free to decay further in healthy tissue. [16]

While the fate of the daughter nuclei of $^{225}$Ac is a serious concern, its efficacy as a medical isotope can't be denied. Preclinical trials have shown remarkable results so far, especially in the treatment of Acute Myeloid Leukemia(AML)[19] and metastatic Castrate Resistant Prostate Cancer (mCRPC) [20]. Perhaps one of the most striking images comes from a trial by Kratochwil et al. where 2 patients with advanced mCRPC were treated after exhausting all conventional therapies. Both patients showed an excellent and almost complete response to the treatment as shown in image 2.3. The patient in question received 3 doses of 9-10 MBq of $^{225}$Ac (100 kBq per kg of body weight) on a bimonthly basis and one consolidation treatment of approximately 6 Mbq afterward. The $^{225}$Ac was delivered by antibody targeting vectors called PSMA (prostate-specific membrane antigens).

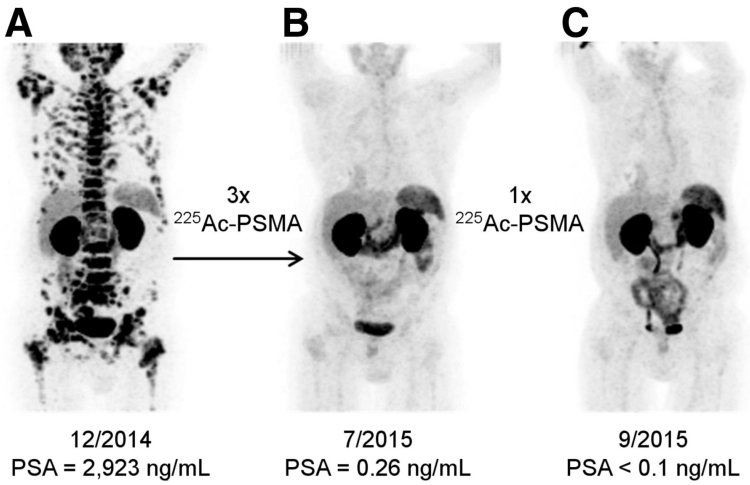


Figure 2.3: Imaging of PSA (prostate specific antigens) by PET/CT of a patient undergoing treatment with $^{225}$Ac-PSMA. An almost complete response can be observed, highlighting the potential of $^{225}$Ac as a radionuclide [20].

The remarkable therapeutic effects of $^{225}$Ac are also coupled with a number of undesirable non-targeted ones. In a recent study with $^{225}$Ac-PSMA for mCRPC on a group of

26 patients, over one-third had to stop the treatment due to serious side effects. Most commonly Hematological toxicities like anemia and leucopenia which are shortages of red and white blood cells respectively. All patients also suffered from varying degrees of xerostomia where the salivary glands are not able to produce enough saliva anymore to keep the mouth wet [21]. The origin of these side effects can be found with decay in unwanted regions like the blood and in the salivary glands where $^{225}$Ac-PSMA tends to accumulate.

The next and perhaps biggest obstacle to be discussed is the supply of carrier-free $^{225}$Ac itself. Current supply routes, as well as new potential production methods to respond to this issue, will be discussed in the next section.

## 2.1 Supply of $^{225}$Ac

No primordial $^{225}$Ac remains on earth, nor are there naturally occurring generators of the isotope. This means that it has to be artificially produced for usage in the medical field. As of the time of writing this work, the main method by which this is done is by chemical separation from leftover $^{229}$Th($T_{1/2} = 7880$ y) stocks that slowly decay to $^{225}$Ac [22]. First considered as a leftover waste product from nuclear programs in the '40s and '50s, these stocks are now being repurposed for $^{225}$Ac production. Almost all of the available $^{225}$Ac is produced via these channels in 3 main facilities located in the US, Germany and Russia. Potential production capacities are listed in table 2.1.

Table 2.1: The Three organizations/facilities supplying most of the world's $^{225}$Ac as of 2018. [15]

| *Facility* | *Approximate Annual Production Capacity* $[Bq]$ |
|---|---|
| *US D.O.E , Washington D.C., USA* | $37GBq$ |
| *JRC , Karlsruhe, Germany* | $13GBq$ |
| *JSC , Obninsk, Russia* | $16GBq$ |

While efforts are underway to increase production of and from $^{229}$Th stocks, these will not be enough to fuel the ever-growing interest in TAT. A typical treatment plan with $^{225}$Ac requires in the order of 10's of MBq's. With the current worldwide production capacity, little more than 1000 patients could be treated each year. Clinical trials and ongoing research in TAT are severely constrained by this limited supply.

Multiple alternative production routes are currently under investigation to respond to this problem. The two most promising routes involve the production of $^{225}$Ac from $^{226}$Ra and inducing spallation reactions on thorium and uranium targets. In the first method, protons are accelerated in medical cyclotrons to optimal energies of around 14 MeV and induce the $^{226}$Ra(p,2n) reaction to directly create $^{225}$Ac [23]. Alternatively, photons of MeV energies can be used to induce the $^{226}$Ra($\gamma$,n) reaction in order to create $^{225}$Ra($T_{1/2} = 14.9$ days) which is a generator of $^{225}$Ac[24]. The second method utilizes high energy (>70 MeV) protons for $^{232}$Th(p,x) and $^{23x}$U(p,x) spallation reactions on solid targets. Various isotopes are produced in these reactions among which $^{225}$Ac. The desired isotope can

subsequently be extracted from the target and purified by laser ionization and mass separation (LIMS). Using this method, the procured actinium for this work was synthesized at CERN-MEDICIS. A discussion of this facility and how the production of $^{225}$Ac was achieved will now follow.

## 2.2 Purification of $^{225}$Ac at CERN-MEDICIS

The idea of producing pure beams of exotic isotopes with the isotope separation on line (ISOL) technique has a rich history. There are currently multiple facilities in Europe dedicated to this endeavour such as ISotope Separation On Line DEvice(ISOLDE) in CERN and SPIRAL-1 at GANIL in France. While these facilities could theoretically be used to produce medical isotopes, their research is mostly focused on fundamental and applied nuclear physics. Not only have these facilities not been designed for medical isotope production but the operating times required to produce substantial amounts (e.g. 65 MBq/g target material / Coulomb protons ) would interfere with ongoing research. Due to this issue, CERN initiated a project in 2010 to provide hospitals and other institutes with the needed radionuclides for treatment, imaging and research. This initiative culminated in the MEdical Isotopes Collected from ISolde (MEDICIS) facility which entered commission in the autumn of 2017 [25].

MEDICIS is to date the only facility in Europe dedicated purely to the production of medical isotopes via mass separation. It is also a crucial facility in the 'PRoduction of high purity Isotopes by mass Separation for Medical APplication' (PRISMAP) European project [26]. This initiative was created to translate the production of up-and-coming medical isotopes into actual treatments.

To induce the desired spallation reactions with sufficient cross-sections in solid targets, high energy protons are needed. In MEDICIS, these are provided by the CERN Proton Synchrotron Booster (PSB). Here, protons are accelerated up to 1.4 GeV before being transferred/delivered to other facilities. This proton beam has an intensity of up to 2 μA and was originally intended for fundamental research in the adjacent ISOLDE facility. However, a large fraction (>65%) passes through their targets without interacting with them [25]. A second target could hence be placed behind the primary one in a so-called 'parasitic' mode, still receiving a sizable portion of the beam. These latter targets are the ones typically reserved for the production of medical isotopes.

After irradiation, the targets containing the desired isotopes are transported to a separate bunker for subsequent extraction and purification. MEDICIS is hence not necessarily an on line facility. During the long shutdown periods of CERN, it was one of the few facilities that kept operating thanks to a supply of medical isotopes from other production sites[25].

To make the produced isotopes effuse out of the target, it is first heated to high temperatures above 2000K . The atomic vapor created in this process is guided towards an ion source where laser ionization takes place. Three lasers are used in this process of

which one excites the ground state. Subsequently, two others are used to excite atoms further into auto-ionizing states above the ionization potential. This process is illustrated in figure 2.4a. Desired isotopes are then accelerated by a 60kV electrode and sent through a dipole magnet which affects the trajectory of the charged, ionized particles according to their mass-over-charge ratio. The end result is an isotopically pure, Gaussian beam of $\sim$ $\sigma$=1.175mm which is implanted on aluminium-coated gold foils. The implantation energy will become important later on and is 60 keV while a representation of the experimental setup is shown in figure 2.4b.

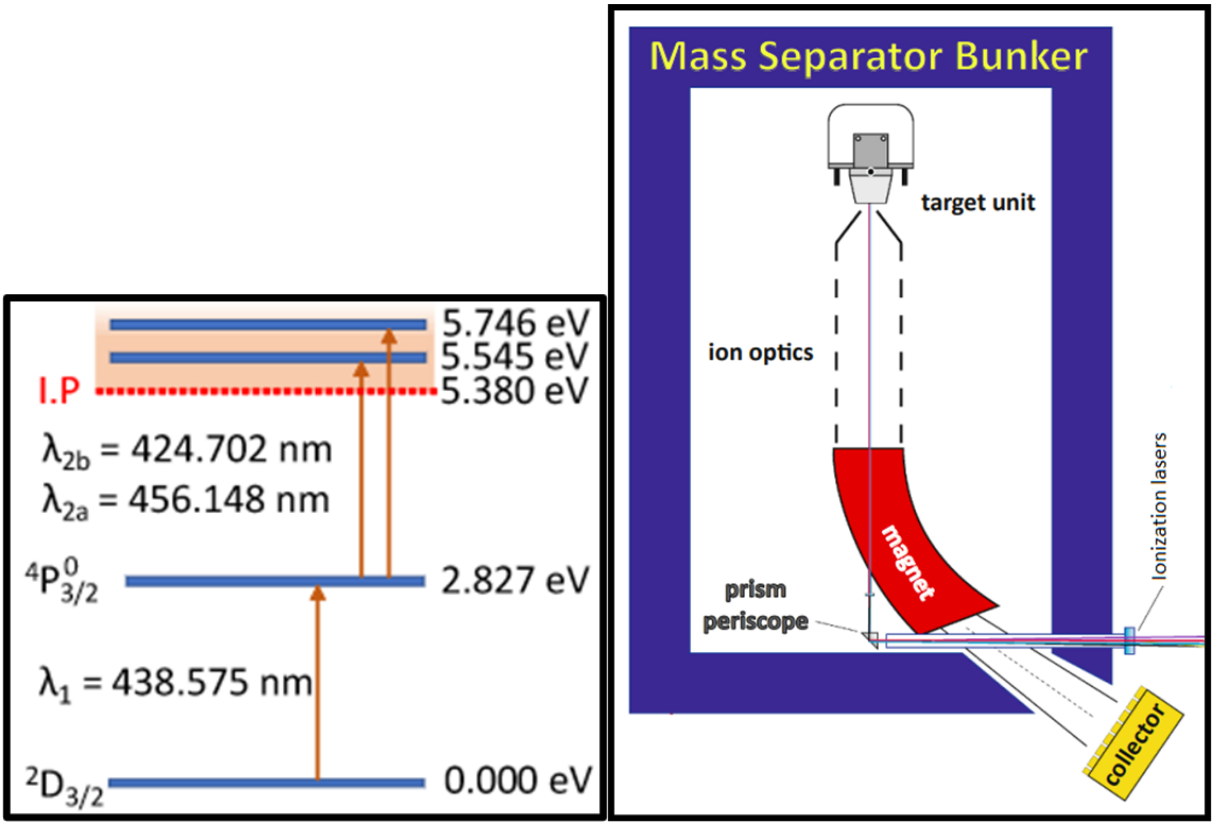


(a) (b)

Figure 2.4: (a) Example of a two step laser ionization scheme (b) Experimental setup for mass separation in MEDICIS [27]

One of these coated gold foils with implanted $^{225}$Ac, designated as sample M171 is a major subject of study in this work. Its characterization will now be discussed.

## 2.3 Activity at End Of Collection with $\gamma$ - $\gamma$ Coincidence Measurements

One of the challenges of this work was to accurately determine activities at end of collection (EOC) of sample M171. By comparing this to in-target yields, the collection efficiency of $^{225}$Ac in MEDICIS could be determined. It also serves to determine the purity of the

sample by comparing activities of other isotopes to the obtained EOC activity. Last but not least, it is imperative to know the activity on the sample for later cell irradiation with foil M171.

Determining EOC activity could be done with spectroscopic techniques but as previously discussed, alpha emissions induce a recoil on the decaying nucleus. In the case of heavy (A$\sim$200) nuclei, this recoil is of the order of 100 keV which exceeds the implantation energy in MEDICIS. As a consequence, a considerable fraction ($>$50%) of $^{225}$Ac daughter nuclei recoil out of the sample. Hence, the geometric source distribution for a given isotope depends on the number of alpha decays that have preceded it. For example, when placed in front of a detector in vacuum, these recoils can implant on its surface. A subsequent alpha decay in this daughter can then cause it to recoil out again and potentially implant on the sample once more. This 'ping-pong' effect shown in figure 2.5 necessitates involved geometric modelling. For a thorough discussion on this topic, the reader is directed towards the thesis by Heines [28].

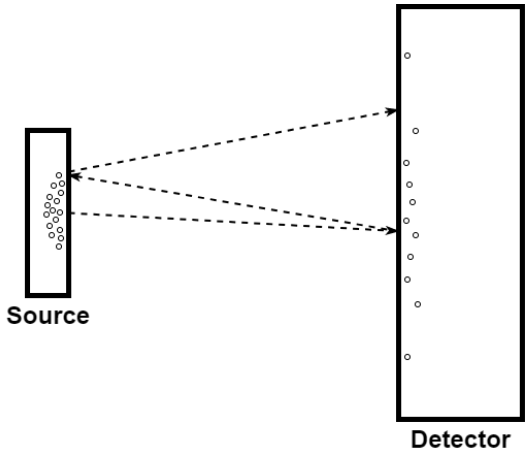


Figure 2.5: Illustration of the 'ping-pong' implantation effect.

Instead, it was decided to determine the activity via a method that is not dependent on geometric efficiencies. A $\gamma - \gamma$ coincidence measurement was chosen for this task.

Coincidence measurements are an essential tool in the detection of ionizing radiation. Following transmutative decay, daughter nuclei are often in excited states. One possible relaxation channel is via the emission of a photon. In some nuclei, multiple photons can be emitted on a timescale of picoseconds or 'in cascade' after a decay event. Two detectors can be used to measure both the single gamma spectra and the count rate of these coincidence photons. Afterwards, the activity of a sample can be obtained by combining them in a specific way as shown by equation 2.1.

$$\begin{aligned} N_1 &= \varepsilon_1(E_1) I_1 A \\ N_2 &= \varepsilon_2(E_2) I_2 A \\ N_{12} &= \varepsilon_1(E_1)\varepsilon_2(E_2) I_{12} A \end{aligned}$$

$$A = \frac{N_1 N_2}{N_{12}} \frac{I_{12}}{I_1 I_2} \tag{2.1}$$

With $\varepsilon_{1,2}$ the response of detector 1,2 at $E_{1,2}$, $I_{1,2}$ the single gamma-ray intensity relative to each parent decay, $I_{12}$ the intensity of both $\gamma$-rays emitted sequentially in cascade and A the activity of the source. By combining these factors, an 'efficiency-free activity measurement' can be made. Due to the combination of the intensities, all geometric, electronic and intrinsic efficiency considerations are canceled out. The need for a $\gamma$-cascade, possible branching in decay chains and the detection efficiency of coincidences themselves often results in low count rates, however.

There are two transitions in the $^{225}$Ac decay chain that were considered as candidates for $\gamma - \gamma$ coincidences. More precisely the cascades after the $\beta^-$ decay of $^{213}$Bi and $^{209}$Tl shown in figure 2.1. Other decays miss the necessary $\gamma$ intensity or don't have a suitable cascade for coincidences. Only 0.56% of $^{213}$Bi $\beta^-$ decay results in the sought-after cascade. For the case of $^{209}$Tl on the other hand, 95.4% of decays result in a suitable cascade, yet the efficiency is limited by the low (2.14%) alpha branching of $^{213}$Bi. Detection efficiencies of the order of 0.2% and 2% for $^{213}$Bi and $^{209}$Tl respectively are the result. After considering these efficiencies, only $^{209}$Tl was considered as a viable option due to the relatively low activity of the sample (<100 kBq). For analysis of a higher activity foil where the coincidences after $^{213}$Bi-decay are also considered, the reader is directed towards the master thesis by Heines [28].

Energy levels of $^{209}$Pb after the decay of $^{209}$Tl are shown in figure 2.6. The main decay branch is highlighted in red on this figure and it is the last 2 gamma decays that will be considered. Their energies and relevant quantities for use in equation 2.1 are listed in Table 2.2.

Table 2.2: Relevant quantities for the 2 $\gamma$ transitions used for coincidences after the decay of $^{209}$Tl. $I_{12}$ was obtained by accounting for electron conversion branching between the 2 transitions.

| $E_1$ [$keV$] | $E_2$ [$keV$] | $I_1$ [%] | $I_2$ [%] | $I_{12}$ [%] |
|---|---|---|---|---|
| 465.14(1) | 1567.08(3) | 95.4(10) | 99.963(7) | 95.1(11) |

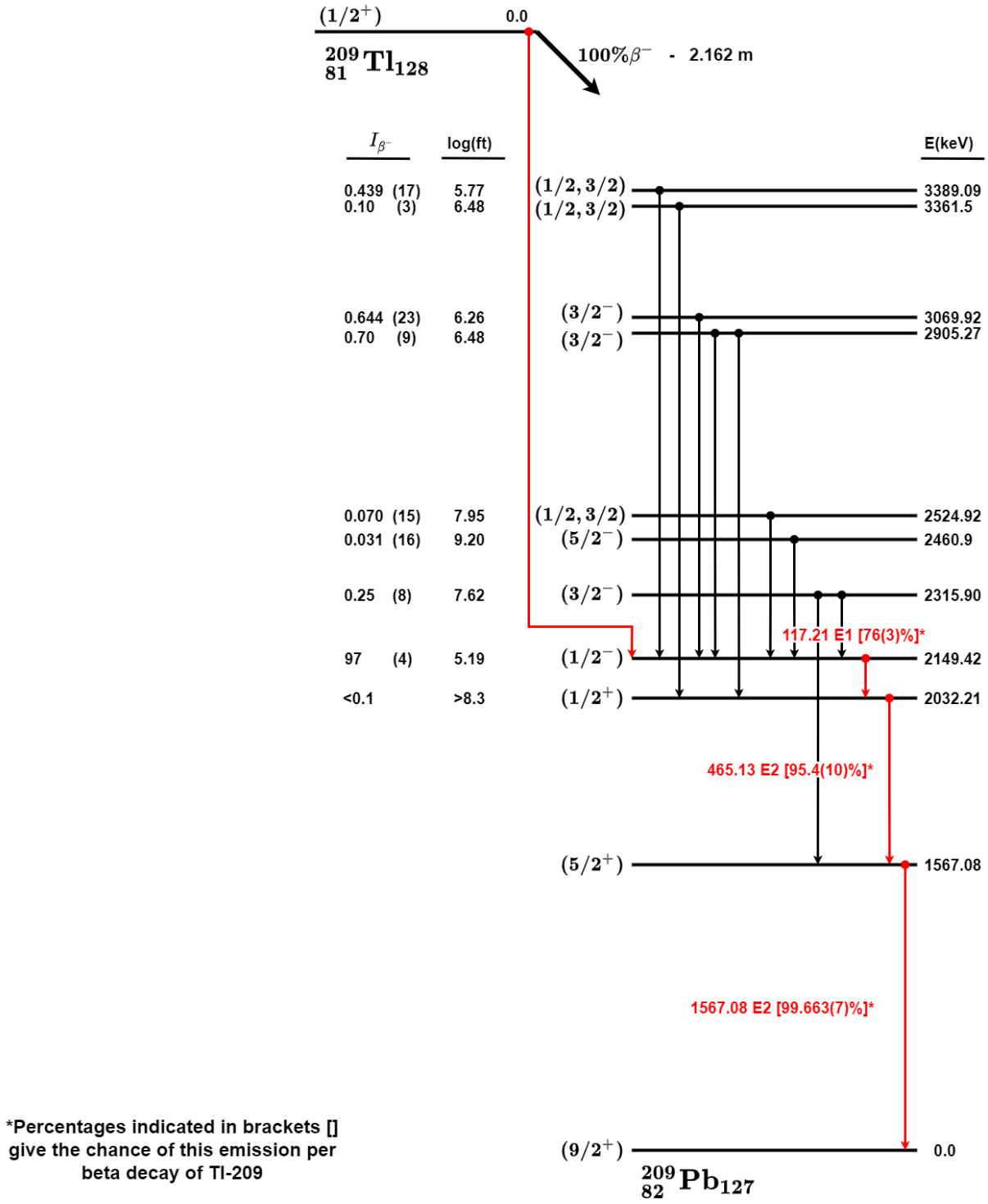


Figure 2.6: Gamma emissions after $\beta^-$ decay of $^{209}$Tl. The path where the majority of decays used for coincidences came from is indicated in red.

Coincidence measurements make it possible to cancel out many considerations related to efficiencies. One correction still needs to be calculated, however, namely the angular correlation between the photons. An angular correlation factor is a combination of sine and cosine terms. To this end, 2 detectors are placed at a 90° angle respective to each other.

This way, all cosine terms in the angular correlation factor become 0, leaving only the sine terms. The sine terms however only need to be considered if the 2 transitions in question are of different multipolarities. In the case of the $^{209}$Tl transitions, they are of the same E2 type. Hence, angular correlation factors can be ignored as long as the detectors are kept at sufficient distances from the sample and at a right angle. The further detectors are from the sample, however, the lower the geometric efficiency. This is one of the main reasons why a high activity source is typically required.

Pictures of the experimental setup and accompanying electronics scheme that was used to measure the coincidences are shown in figures 2.7a and 2.7b respectively. First, two High Purity Germanium detectors (HPGe) were cooled down to cryogenic temperatures. The sample foil contained in a glass vial was subsequently placed on the measuring table and the detectors were angled to 90°. Each detector is connected to a preamplifier after which the signal is sent to a Caen N6724 digital acquisition system (DAS). Classical modules such as shaping amplifiers are replaced by this DAS which stores the relevant data of each recorded pulse and transfers it to a PC via USB connection.

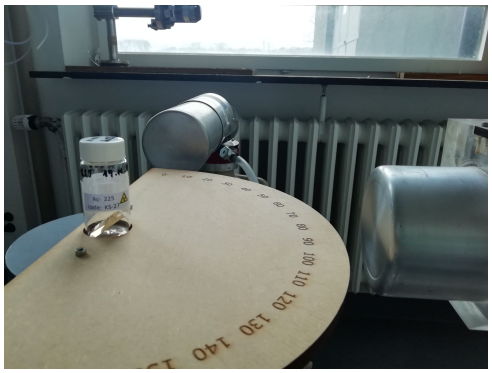

(a)

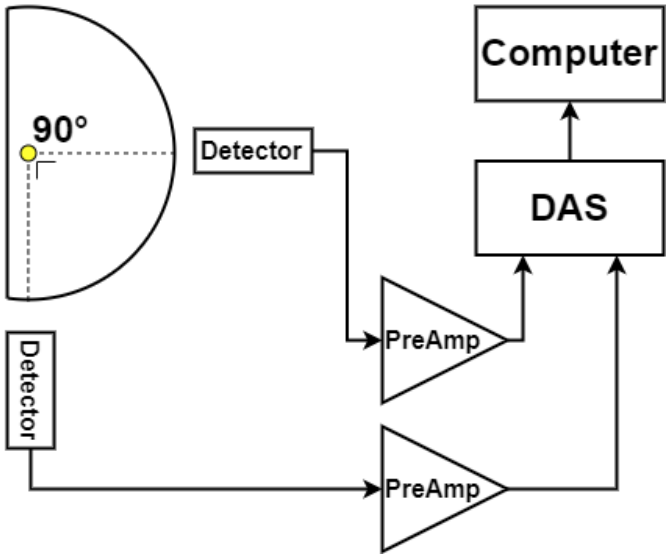


(b)

Figure 2.7: (a) Glass vial with foil M171 in the coincidence setup. The 2 HPGe detectors are shown oriented at a right angle. (b) Experimental and Electronics scheme for the coincidence setup.

During the measurements, gamma spectra are recorded in both detectors. By analyzing the times at which events happen and using these to filter for coincidences, the necessary quantities for use in equation 4.7 can be obtained. To process the data, specialized ROOT code written by Michael Heines was used [29][28]. A flowchart of the steps that this code takes to determine the activity of a sample is shown in figure 2.8.

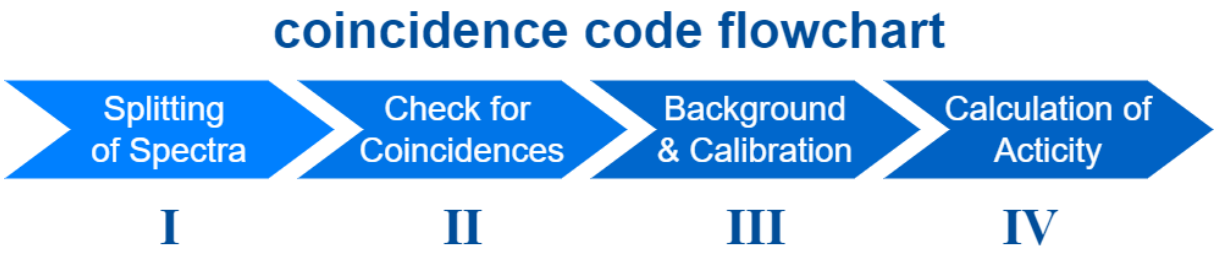


Figure 2.8: Flowchart of the major steps taken by the coincidence code.

An in-depth explanation of the code will now follow. If the reader wishes to skip this discussion, they are directed towards the end result shown in figure 2.12.

(I)
The process starts by considering raw event data obtained during measurements. Two spectra were built from the detected gamma radiation, one for each detector. These spectra were obtained over long periods of time, so they are first split up into different batches that are analyzed separately. Each batch provides one data point for the activity at their mean time and thus as many data points as possible are preferential. However, as obtained coincidences in a batch decrease, the error on obtained activities increases following $\sqrt{n}$ Poisson statistics. Hence, to determine in how many batches the data should be split up, the code first ran to determine the total number of coincidence counts. This resulted in a number of 187 coincidences over a period of 12 days. It was decided to split them into 8 batches of around 20-25 coincidence counts each yielding errors in the vicinity of 20%. After the data is split up in batches, mean times are calculated. These are the times after which the sample has decayed to the average activity from start to finish of the batch. Since nuclear decay is an exponential process, this is not simply the middle point but a time closer to the start of each batch.

(II)
After this preparatory phase is over, the spectra of each detector are taken separately. For each event, another is sought within the detector resolution of 200 ns in the other detector to check for potential coincidences. If one is found, the times of detection and energies are saved for later use. Histograms of the single-count energy spectra are also constructed after which a background subtraction is performed.

(III)
For this subtraction, a specialized algorithm called SNIP is employed which is able to estimate the background accurately and leaves a very clean spectrum [30]. An example of a single-count energy spectrum and its background estimation, as well as a subtracted spectrum, are shown in figure 2.9.

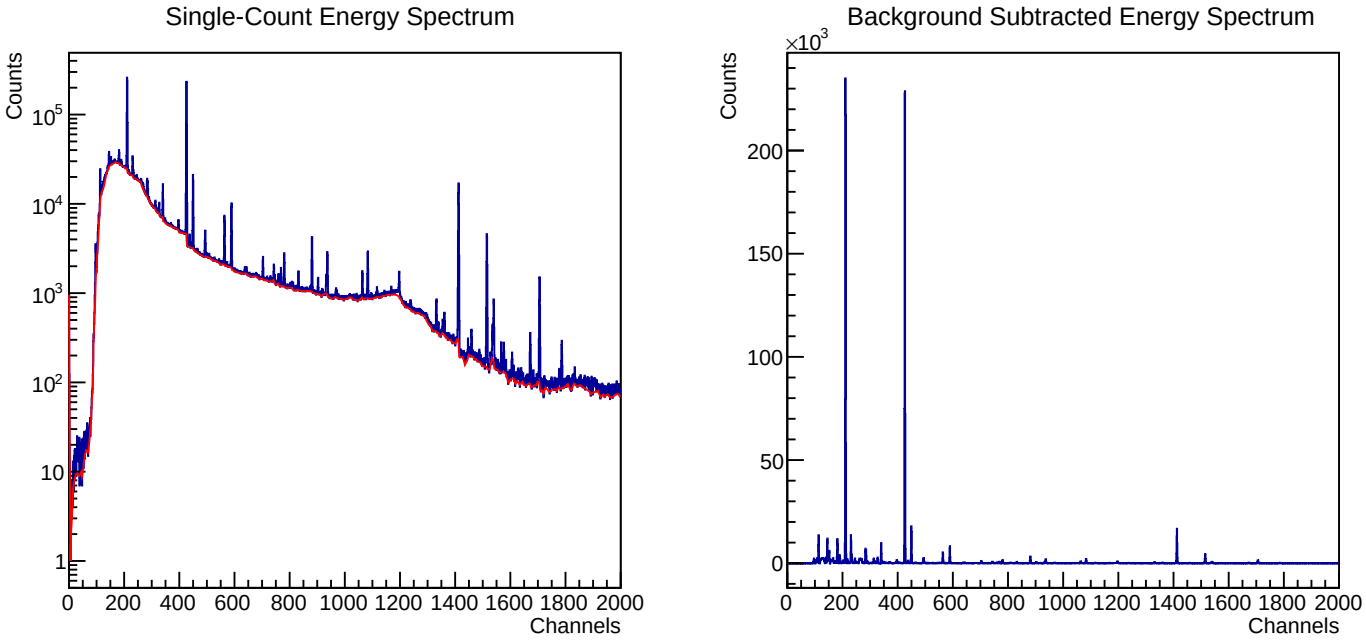


Figure 2.9: (Left) Single-count energy spectrum with its background estimation indicated in red. (right) Same spectrum with the background subtracted.

The number of counts, N, in each peak is then obtained from summing over the bins. The error on the total number of counts in a peak is then given by $\sqrt{N}$.

After background subtraction, an energy calibration is made with the obtained peaks. For this calibration, the peaks of 218 keV, 440 keV and 1567 keV gamma-rays were considered. These gamma-rays follow the alpha decay of $^{221}$Fr, the $\beta^-$ decay of $^{213}$Bi and the alpha decay of $^{209}$Tl respectively. The 2 former ones are also indicated in figure 2.1 since they could be used for in vivo medical imaging techniques. The peaks are located by finding the largest one in a user-defined interval. Care has to be taken when selecting this interval to make sure that there are no larger peaks in the vicinity of the desired decay. If the activity of a sample is low enough, it is for example possible that a natural background peak is larger than the sought-after one. In foil M171 for example, the peaks of natural $^{40}$K at 1460 keV had roughly ∼1.4 times the count rate of the peaks at 1567 keV.

(IV)
Finally, the bin integrals of the relevant peaks are taken in the background-free single gamma spectra. To get the count rates of the coincidences, integration in these energy windows is then performed for the previously saved potential coincidences. Both detectors have to be taken into account since the first emission or 'trigger photon' at 465 keV can of course be detected in either one. The resulting coincidences after the trigger photon of a sample spectrum are shown in figure 2.10.
Looking at this spectrum, some noteworthy peaks can already be distinguished by eye. There is the sought-after coincidence peak at 1567 keV (1). Additionally, there is the peak at 465 keV (2) and the 218 and 440 keV peaks (3,4) from the $^{221}$Fr and $^{213}$Bi decay respectively. All other counts come from either a Compton continuum or random coincidences.

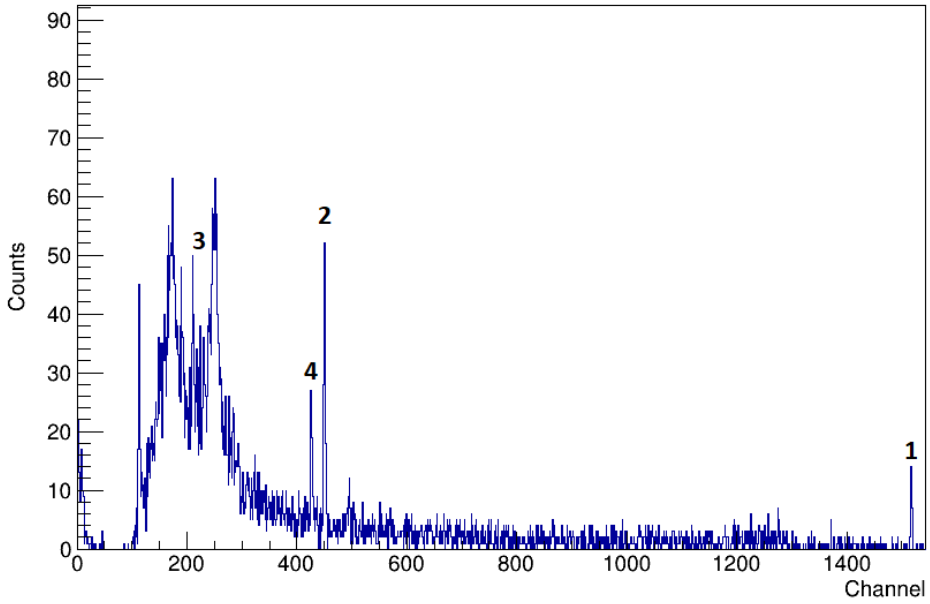


Figure 2.10: Coincidences after the detection of a 465 keV photon. Relevant peaks are indicated and discussed below.

The counts of the relevant peak, the mean time and the relative error based on $1/\sqrt{n}$ Poisson statistics are saved for each batch. Finally, this allows for a fit through the 8 points obtained from the batches. Resulting in the activity of the sample at end of collection in MEDICIS.

While calculating these activities, a physical factor called the Bateman correction has to be taken into account. As a parent isotope decays, it takes time for its daughter to also decay depending on its half-life. A population of daughter isotopes will hence grow until secular equilibrium is reached, where as many daughter isotopes are generated as there are decaying. Because the decay is not instantaneous, there will eventually be a slightly higher activity of daughter isotopes due to time lag. This behavior is described by the Bateman equation in 2.2 Since the coincidence measurements of the $^{209}$Tl give its activity and not that of the $^{225}$Ac, this factor has to be incorporated on top of the branching ratio's.

$$N_n(t) = N_1(0) \times \left( \prod_{i=1}^{n-1} \lambda_i \right) \times \sum_{i=1}^{n} \frac{e^{-\lambda_i t}}{\prod_{j=1, j\neq i}^{n} (\lambda_j - \lambda_i)} \tag{2.2}$$

With $N_i$ the population of isotope i that decays into isotope i+1 and $\lambda_i$ its decay rate. In secular equilibrium, the activity of a daughter isotope can be described using the simplified equation 2.3 [31].

$$\frac{A_n}{A_1} = \prod_{i=2}^{n} \frac{\tau_1}{\tau_1 - \tau_i} \tag{2.3}$$

With n indicating the n'th daughter isotope and $\tau_i$ indicating the half-lives of the daughter isotopes at position i in the decay chain. To find the time after which this secular equilibrium is reached and equation 2.3 can be used, the activities can first be plotted using the full Bateman equation. When starting from the activity at EOC, the result in figure 2.11 is obtained. Daughter isotopes of the actinium slowly grow depending on their decay times and decay chain position until secular equilibrium is reached approximately 10 hours later. Omitting $^{209}$Pb since it is not an alpha emitter, it is justified to use equation 2.3 beyond this point to determine the activities of daughter Isotopes. This first secular equilibrium point is also when the total activity of the foil peaks at around ∼820 kBq. It is important to note that a significant amount of $^{225}$Ra($T_{1/2} = 14.9$ days) was also present after EOC. Since this is a generator of $^{225}$Ac, the time behaviour of the decay is described by exponential decay with actinium half-life, and a second-order Bateman term given by 2.2.

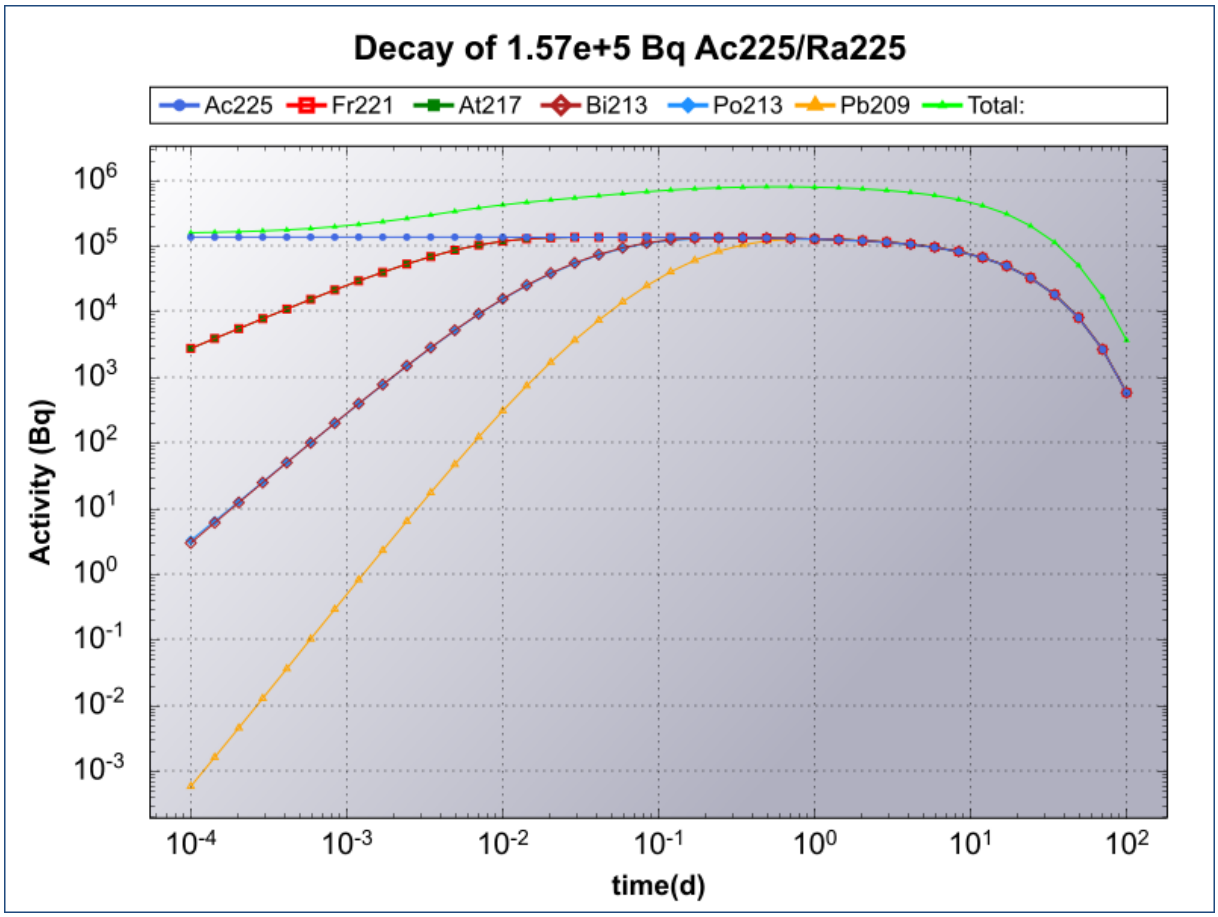


Figure 2.11: Activity of the primary daughter isotopes of $^{225}$Ac calculated using the Bateman equations as laid out in [31] and [32]. The lines of $^{217}$At and $^{213}$Po overlap heavily with their parent isotopes due to their short decay times.

Since the uncertainties on the activity derived from the coincidence data are large, it was chosen to employ Monte Carlo techniques when fitting. To this end, random samples were taken over the uncertainty intervals of the data points and a fit was performed. The equation used in this fit is the exponential decay of $^{225}$Ac supplemented with a second-order Bateman term for $^{225}$Ra present in the sample. This was repeated multiple times

to derive a distribution of the free fitting parameters ($^{225}$Ra initial activity and $^{225}$Ac initial activity). The final fit is performed with the mean parameter values from these distributions, with uncertainty given by the error on the mean (red band). Results are shown in figure 2.12 together with an estimated activity from gamma spectroscopy, taken 7 days after collection in MEDICIS.

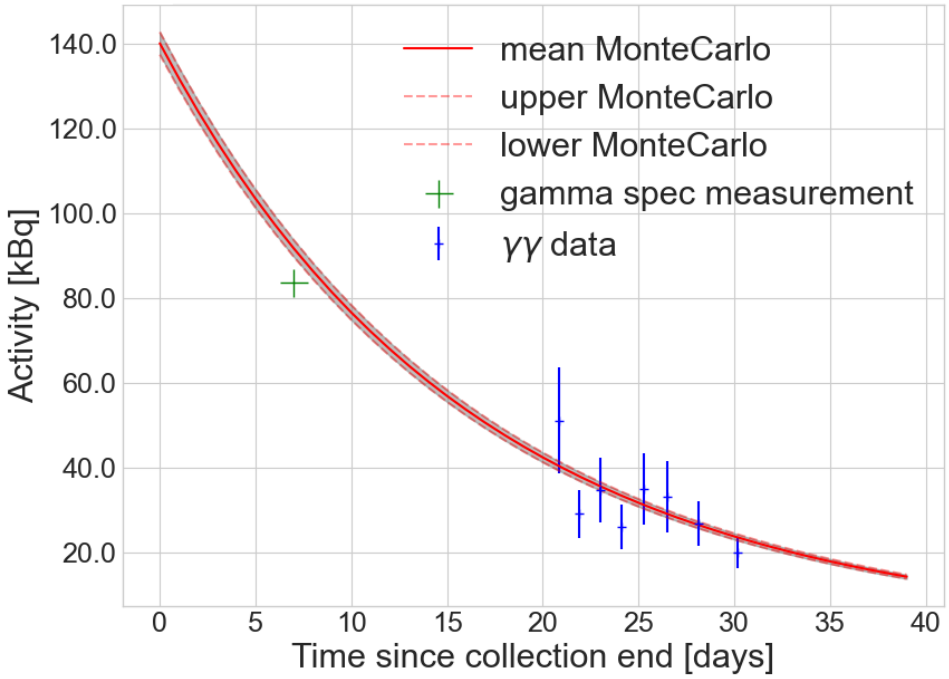


Figure 2.12: Activity of $^{225}$Ac in the M171 sample after EOC. Fit was performed using monte carlo methods.

Results for EOC, the time of $\gamma$ spectroscopy in MEDICIS and the activity from these measurements are listed in table 2.3. Given the relatively low activity for coincidence measurements, a satisfactory result within ∼10-15% of the $\gamma$-spec data was obtained. This activity can now be compared to in-target production yields in MEDICIS. Two foils were produced from the target of foil M171. By adding the EOC activity of M171 with the other source, a total production of 200949 Bq was recorded. Compared to the in-target yield of 4.52 MBq, a collection efficiency of 4.44±0.12 % is obtained.

Table 2.3: Activities of sample m171 obtained from $\gamma$-$\gamma$ coincidence measurements and $\gamma$ spectroscopy performed in MEDICIS.

| Isotope | A at EOC [kBq] | A at time of $\gamma$-spec [kBq] | A from $\gamma$-spec [kBq] |
|---|---|---|---|
| $^{225}$Ac | $138.8 \pm 2.7$ | 90.4±2.1 | 83.8 |
| $^{225}$Ra | $17.9 \pm 1.1$ | 12.9±0.9 | 11.1 |

The next section will now use these obtained activities to investigate the isotropic purity of foil M171.

# Chapter 3

# Determining the Purity of $^{225}$Ac Collected in MEDICIS

Accelerator-based production of $^{225}$Ac could potentially provide a solution for persisting supply issues. Just like with the chemical separation from thorium stocks, however, it has to be purified before it can be used for medical applications. In the case of laser ionized and mass separated $^{225}$Ac, this happens via element selective laser ionization and mass selective separation via dipole magnet. The main contaminant that MEDICIS tries to suppress this way is $^{227}$Ac whose decay chain is shown in figure 3.1. It has a half-life of 21.7 years with 3 $\beta^-$ decays and 5 alpha decays in short succession before stable $^{207}$Pb is reached[33]. These properties and long half-life make any waste containing this isotope difficult and expensive to handle.

Impurities from long-lived nuclides like $^{227}$Ac generally don't pose a physiological risk, on the condition that the radionuclide is eventually excreted. Contaminated materials from the treatment as well as waste from the patient itself can contain these long-lived radionuclides however and must hence be handled appropriately. Some long-lived radiopharmaceutical waste contains isotopes with manageable lifetimes like e.g. $^{177m}$Lu with a half-life of approximately half a year. This means that waste can be stored and left to decay, even in the hospitals themselves. This luxury can not be afforded for $^{227}$Ac since if sizable contamination occurs, it could take decades to centuries before waste can be safely disposed of.

The question of when this waste becomes safe and what levels of contaminants should be allowed is a complex one. Usually, the criteria of exemption and clearance levels are used. An exemption level indicates an activity below which a source of radioactivity can be handled without oversight by authorities. A clearance level on the other hand indicates activities below which the waste is considered to be safe for disposal. These levels do not only depend on scientific considerations, but also on how strict regulation is in the country where the therapy is performed. To add to the confusion, standards for radiopharmaceuticals are often different from the general exemption and clearance levels. In Germany for example, the exemption level for $^{227}$Ac is 1 kBq, yet medically approved $^{223}$Ra can contain up to 24 kBq of $^{227}$Ac in a 6 Mbq dose [15]. In October 2018, the International Atomic Energy Agence (IAEA) and the Joint Research Centre (JRC) of the European Commission held a two-day workshop on the demand and supply of $^{225}$Ac. To

have a goal for production, the general consensus in the report of this workshop will be taken. It advised that $^{227}$Ac concentrations should be kept at least below 0.01% of the total activity [15].

With this in consideration, it is imperative to evaluate the contaminant activity in the laser ionized and mass separated sample of $^{225}$Ac collected at CERN MEDICIS. Its suitability for medical purposes can thus be evaluated, and the performance of the mass separator can be benchmarked. One plan involved waiting until all traces of $^{225}$Ac had disappeared from foil M171. Afterwards, the activity of $^{227}$Ac could be determined using spectroscopic techniques with minimal interference. Unfortunately, the sample was rendered unusable and had to be disposed of due to a technical incident. A report of this event is included in appendix B. Fortunately, measurements to determine $^{227}$Ac activity on foil M171 were already made. These were performed in the ASET with a technique that will now be explained.

A significant fraction of alpha recoil daughters in the $^{225}$Ac decay chain (>50%) is ejected from sample M171. Even after leaving the foil, these can still have energies in the range of several 10's of keV. Small enough that these heavy recoils are stopped by less than 100 µm of air. However, sufficient for implantation on a detector surface in vacuum. This implantation leads to the previously discussed 'ping-pong' effect shown in figure 2.5.

When implanting recoils on a detector surface with foil M171, not only daughters of $^{225}$Ac are implanted. The same physical behaviour is also expected for the daughters of the $^{227}$Ac decay chain shown in figure 3.1. Initial $\beta^-$ decay in the chain doesn't offer the energy needed to recoil out of the foil due to (in general) lower decay energies and the lower mass of electrons. This makes $^{227}$Th essentially the starting point for a chain of alpha decay comparable to that of the $^{225}$Ac in terms of recoils. Key here is the longer half-life of $^{223}$Ra which is ∼3000 times longer than that of $^{221}$Fr[34]. Meaning that activities from $^{227}$Ac daughters/recoils persist for a much longer time than those of $^{225}$Ac.

The longer half-lives can be exploited by putting foil M171 in front of a detector, leaving it to implant daughters on its surface. After implanting for several days and then removing the foil, they will slowly decay. By waiting for a sufficient amount of time, only the long-lived $^{223}$Ra would remain alongside its daughters who haven't escaped the detector surface. This waiting time would be constrained by the longest decay time in the $^{225}$Ac chain, namely $^{213}$Bi with a half-life of 45.6 minutes. Activity of the contaminant on the foil could afterwards be calculated with the right geometric considerations.

In the end, the required data are the implantation efficiencies or A(detector)/A(foil) of $^{227}$Ac daughters after implantation. It is not impossible to model these recoils yet a different approach was considered. After recoiling out of the sample, daughter nuclei travel in a straight line in vacuum. Since the recoils have comparable energies as shown in table 3.1, the spatial distribution of each of the alpha recoil daughters should be comparable. If one wants to know what the implantation efficiency of a daughter of $^{227}$Ac is, it suffices to look at the same generation in the $^{225}$Ac chain as shown in figure 3.1. The sought-after implantation efficiency of $^{223}$Ra can e.g. be obtained by looking at the activity of $^{221}$Fr after implantation. By then relating it to that of the total $^{225}$Ac activity obtained from co-

incidence measurements, the implantation efficiency can be obtained. This efficiency can then be used to calculate $^{227}$Ac on sample M171 by looking at the activity of implanted daughters on the detector.

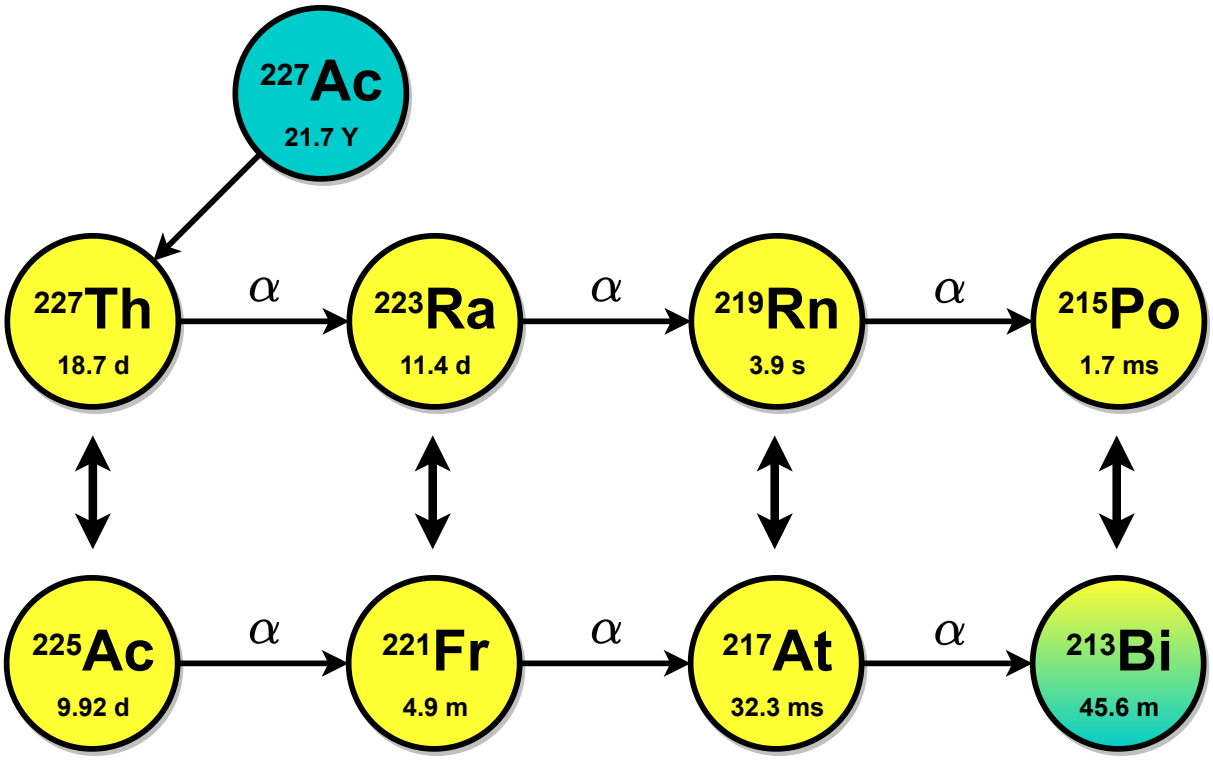


Figure 3.1: Primary decay chains of $^{225}$Ac and $^{227}$Ac. Same generation alpha daughters are displayed alongside each other. Colors indicate primary decay modes with blue for $\beta^-$ and yellow for $\alpha$ decay respectively.
-Elements of the decay of $^{227}$Ac which are not included are chronologically: $^{211}$Pb ($\beta^-$,36.1m), $^{211}$Bi($\alpha$,2.14m), $^{207}$Tl($\beta^-$,4.77m) and $^{207}$Pb(Stable).
-For a complete decay chain of $^{225}$Ac, the reader is directed to figure 2.1.

Table 3.1: Recoil energies of the first 4 generation alpha decays in both the $^{225}$Ac and $^{227}$Ac chain.

| Generation | $^{225}$Ac chain | Recoil E (keV) | $^{227}$Ac chain | Recoil E (keV) |
|---|---|---|---|---|
| 1 | $^{225}$Ac | 105(3) | $^{227}$Th | 105.8(1.7) |
| 2 | $^{221}$Fr | 117.1(0.9) | $^{223}$Ra | 102.8(1.5) |
| 3 | $^{217}$At | 132.65(0.14) | $^{219}$Rn | 125.7(1.6) |
| 4 | $^{213}$Bi | 125.15(0.21) | $^{215}$Po | 140.11(0.03) |

Just like the Bateman equations modelled in figure 2.11, $^{223}$Ra will slowly grow in on the detector surface. However, due to its long half-life, and the half-life of $^{227}$Th, secular equilibrium was not reached within the time allocated to this experiment. Instead, the optimal ratio between implantation time and removal of foil M171 was calculated analytically. The cut-off time between implantation and decay measurement that would maximize total counts subject to a total time constraint was calculated. Implanting for too long would result in too little time for spectroscopy while removing the foil too early

would result in most implanted activity decaying away before the end of the experiment. Assuming an arbitrary activity of $^{227}$Ac on foil, the number of relative measured counts is given by equation 3.

$$N_{\alpha}^{rel}(t) = \frac{\exp\left(-\lambda_A t\right)}{\left(\lambda_B - \lambda_A\right)\left(\lambda_C - \lambda_A\right)} + \frac{\exp\left(-\lambda_B t\right)}{\left(\lambda_A - \lambda_B\right)\left(\lambda_C - \lambda_B\right)} + \frac{\exp\left(-\lambda_C t\right)}{\left(\lambda_A - \lambda_C\right)\left(\lambda_B - \lambda_C\right)} - \exp\left(-\lambda_C T_f\right) \cdot \left( \frac{\exp\left(-\left(\lambda_A - \lambda_C\right) t\right)}{\left(\lambda_B - \lambda_A\right)\left(\lambda_C - \lambda_A\right)} + \frac{\exp\left(-\left(\lambda_B - \lambda_C\right) t\right)}{\left(\lambda_A - \lambda_B\right)\left(\lambda_C - \lambda_B\right)} + \frac{1}{\left(\lambda_A - \lambda_C\right)\left(\lambda_B - \lambda_C\right)} \right) \tag{3.1}$$

With $\lambda_A$,$\lambda_B$ and $\lambda_C$ the decay constants of $^{227}$Ac, $^{227}$Th and $^{223}$Ra respectively. A plot of this function given a total time of 60 days is shown in figure 3.2. The cutoff time represents the moment that foil M171 would be removed from the setup, stopping further implantation of daughters.

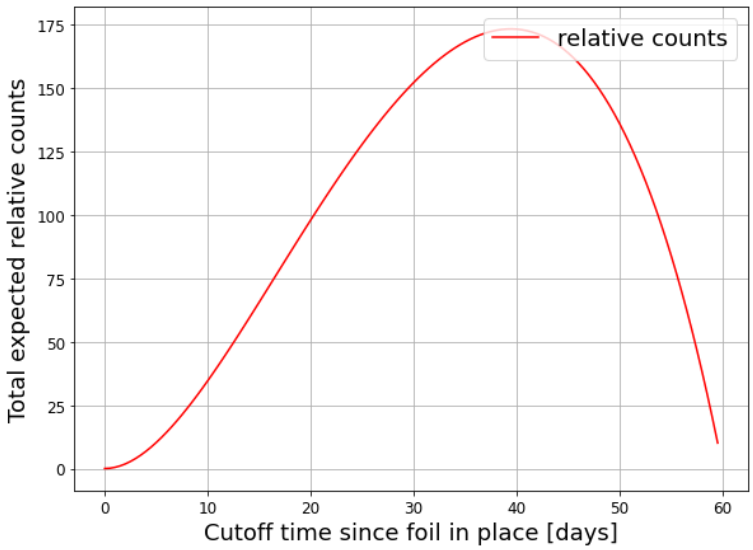


Figure 3.2: Relative number of counts by cutoff time given 60 days for implantation and measuring.

For 60 days, the optimal removal time would be 39.25 days after starting implantation or roughly two-thirds implantation, one-third measuring time. The sample was inserted on 20/12/2021 and removed on 27/01/2022, almost two-thirds of the time until the end of measurements on 22/02/2022. The experimental setup used in these measurements will now be discussed.

In this work, two setups were used to characterize alpha sources that operate in nearly identical ways. The Alpha SETup (ASET) and the so-called "cozy chamber". Shown in figures 3.3a and 3.3b respectively. However, only the ASET was used for measurements of foil M171.

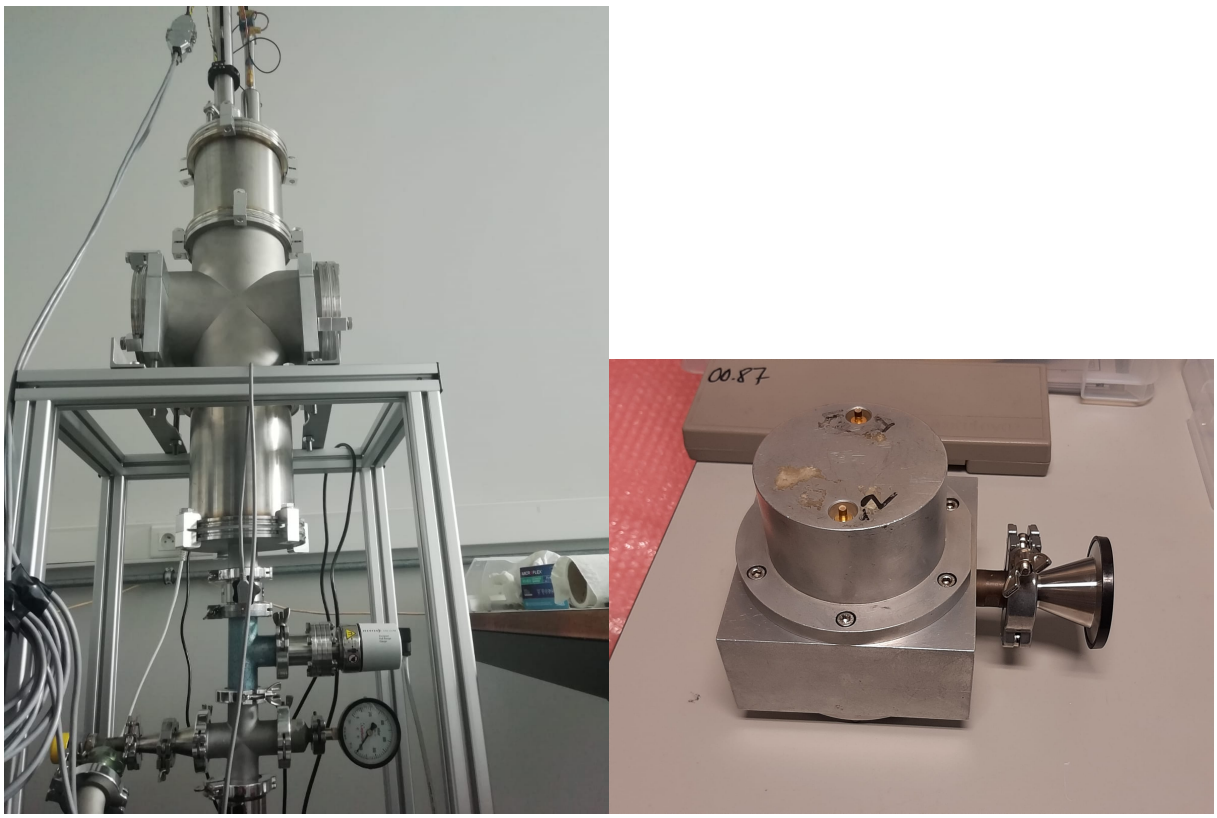

(a) (b)

Figure 3.3: (a) ASET vacuum chamber. (b) Cozy Chamber.

The ASET consists of three major components: a vacuum chamber, movable ladder and detector. The ladder's primary function is to hold sources in place at fixed distances from the detector. Moreover, it allows a user to house and swap multiple sources without having to vent the vacuum chamber in-between measurements. It was custom-made to accommodate both standardized, circular, 25 mm diameter sources as well as 15x25 mm rectangular foils received from MEDICIS.

The cozy chamber shown in figure 3.3b works via the exact same principle minus the ladder and is usually used for its simplicity and compactness. The small size of the chamber makes it difficult to measure accurate source-detector distances however.

Both setups use the same experimental scheme as shown in figure 3.4. First, the source and detector are placed in a vacuum chamber which is pumped down to a pressure of roughly $10^{-6}$ mbar. A good vacuum is necessary since the path lengths of alpha particles are short, even in air($\sim$5-10cm). Afterwards, a Silicon surface-barrier detector is reverse biased with a high voltage supply. When alpha particles impact on the detector, they create electron-hole pairs which induce an electrical signal that is sent to a preamplifier. Here, the signal is amplified into an exponential pulse before being sent to a shaping amplifier that both amplifies the signal further and shapes it into a Gaussian form. Finally, it is sent to an analog to digital converter (ADC) that converts the received electrical signal into a digital one. By using data acquisition software, this digital signal is sorted into bins/channels depending on the energy of the incoming alpha particle. Eventually,

this allows the user to analyze an acquired spectrum.

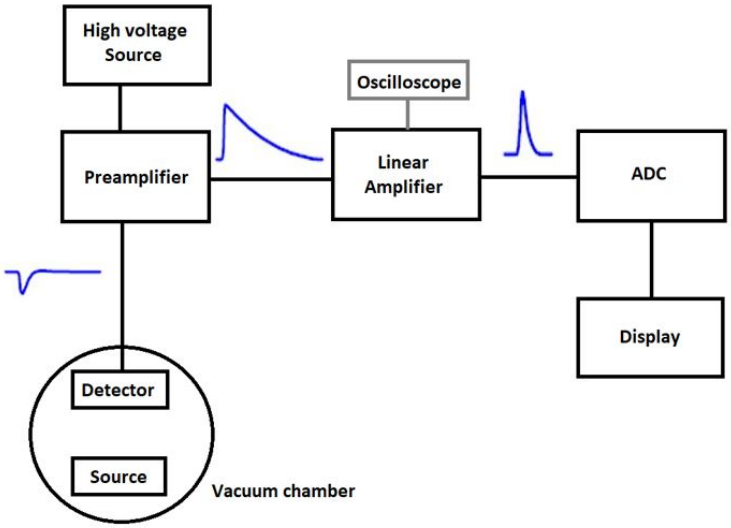


Figure 3.4: Experimental scheme of the two utilized alpha spectroscopy setups. The shape of the electrical signal between the various steps is shown in blue.

Now that the experimental setup is understood, data obtained from the experiment can be discussed. Firstly, foil M171 was positioned in front of the detector to allow alpha recoil daughters to accumulate on the detector for 38 days. Then, the ASET ladder was moved and the foil was positioned far away from the detector. Afterwards, a measurement was started. Spectra from the first day and the entire 19 days are shown in figure 3.5 to illustrate the appearance of $^{227}$Ac daughters over time.

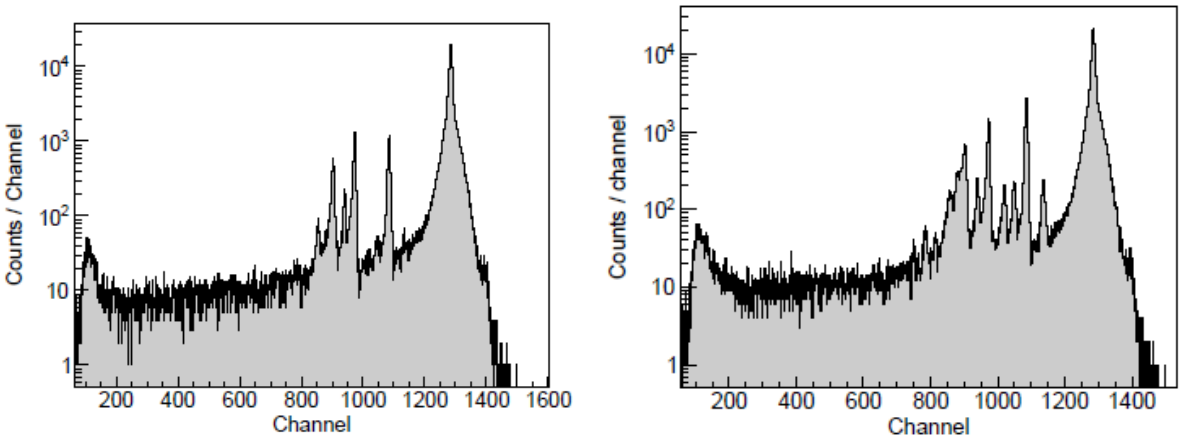


(a) (b)

Figure 3.5: (a) Spectra of the first 24 hours of measurement (b) Counts over the full 19 days of measurement.

During the first 24 hours of measurement shown in figure 3.5a, the daughters of $^{225}$Ac still dominate the spectrum. After they have decayed away, however, the peaks of $^{227}$Ac daughters start to appear in between channels 800-1200 as shown in figure 3.5b. These

spectra were calibrated on the well defined peaks of $^{221}$Fr(6341 keV), $^{217}$At(7067 keV) and $^{213}$Po (8376 keV). A calibrated figure 3.5b with the first day of measurements excluded to remove the influence from $^{225}$Ac daughters is shown in figure 3.6. Peaks of $^{227}$Ac daughters are indicated in red.

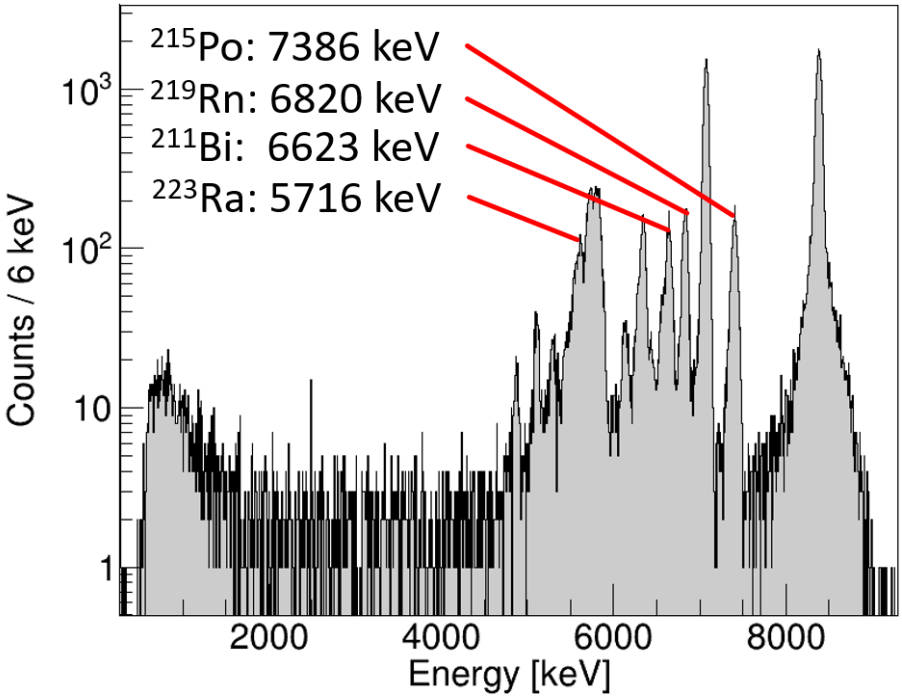


Figure 3.6: Calibrated spectrum over the full measurement with the first 24 hours excluded to remove influence from $^{225}$Ac daughters.

Despite giving the sample 24 hours to decay, counts from $^{225}$Ac daughters were still registered, albeit much less. Two hypotheses were brought forward to explain this behavior. On one hand, it could be self-sputtering, where an atom of $^{225}$Ac is ejected from the sample following a collision with a recoiling daughter or alpha particle. Because of its long half-life relative to the measurement, these sputtered atoms could still contribute to the counts. Alternatively, decay from the foil could somehow still find its way to the detector despite its position.

After an intervention where the foil was removed from the setup completely, measurements still revealed decay events of $^{221}$Fr and $^{213}$Po, indicating that traces of $^{225}$Ac were present on the detector. Because they were less intense, the presence of the foil must also have had an effect. The most likely explanation for these counts is thus a combination of stray alpha particles from foil M171 and self-sputtering.

Because of these residual counts, peaks in figure 3.6 can overlap with $^{225}$Ac daughters like e.g. the $^{223}$Ra peak at 5719 keV with the one of $^{213}$Bi (5875 keV). As a consequence, the very well-defined peak of $^{215}$Po at 7386 keV was chosen to determine the activity of $^{227}$Ac on sample M171. From figure 3.1, the equivalent daughter of $^{225}$Ac to compare $^{215}$Po to would be $^{213}$Bi. Unfortunately, its most intense peak is too convoluted to get an accurate result. The alpha branching of this isotope is only 2.14% however, with the

vast majority decaying to $^{213}$Po via $\beta^-$ decay. Since this type of decay does not induce a significant recoil, the standalone peak of $^{213}$Po at 8376 keV can be used instead.

It was assumed that the initial ratio of activities of daughter isotopes would be equivalent. However, secular equilibrium was not reached from EOC until the start of implantation. Nor was it reached from the start of implantation until the time the foil was removed. This combination means that a model incorporating the combination of geometric and decay-related factors would be required to estimate the population of $^{227}$Ac daughters on the foil and on the detector. The same model could be applied to $^{225}$Ac decay chain to obtain a comparison between the two decay chains however this is beyond the scope of this thesis. An ongoing investigation is being performed by J.D.Johnson on this subject. The true activity of $^{227}$Ac would hence be a convolution of the Bateman equation and geometric considerations. An ongoing investigation to account for these effects is taking place at the time of writing this work. Here, a preliminary analysis is presented to give a first-order approximation of the activity.

The measured count rate of $^{215}$Po at the time the foil was removed was determined to be $2{\cdot}10^{-3}$ counts/s. Three conversion factors were applied to this number for a preliminary result on the activity of $^{227}$Ac in sample M171.

The first is the geometric consideration. After removal of the foil 70 days after EOC, a count rate of 79 counts/s was recorded for $^{213}$Po. This rate was compared to the obtained activity of $^{225}$Ac and therefore $^{213}$Po on foil from the coincidence measurements. Dividing these numbers gave a factor of $79Bq/A(\gamma - \gamma) = 0.031$. Hence, count rates on the detector after removal of the foil would be 3.1% of the total collected activity.

Secondly, a correction has to be applied for the fact that secular equilibrium of $^{227}$Ac daughters has not yet been reached on the foil. The growing population was simulated like in figure 2.11 up to the removal of the foil, 70 days after EOC. This resulted in a ratio of A($^{215}$Po)/A($^{227}$Ac) = 0.833. Lastly, the branching ratio of $^{213}$Bi has to be accounted for yielding a correction factor of 0.9786.

Applying the corrections, a $^{227}$Ac activity of A($^{227}$Ac)= 0.002 Bq/0.031/0.833/0.9786=0.079Bq at the time of removal of the foil was obtained. This corresponds to an activity of 0.080 Bq at EOC, 70 days earlier. By comparing this number to the $^{225}$Ac activity, the ratio of $^{227}$Ac to $^{225}$Ac was found to be 0.080 Bq/138.8 kBq = $5.8{\cdot}10^{-7}$ or 0.00000058%.

The obtained fraction of $^{227}$Ac lies well below the advised maximum of 0.01%. In conclusion, this preliminary result thus indicates that the suppression of $^{227}$Ac by laser ionization and mass separation of accelerator-produced $^{225}$Ac at MEDICIS is sufficient for medical applications. However, to achieve isotopic purity, $^{225}$Ra would have to be purified from samples as well. Since $^{225}$Ra has a lower boiling point, it could be extracted from an ISOL target at lower temperatures than $^{225}$Ac, opening up the possibility of performing separate collections of $^{225}$Ra and $^{225}$Ac. Another foil designated as M119 which was collected from the same target after foil M171 didn't show any signs of $^{225}$Ra being present. It would hence suffice to deplete a target from $^{225}$Ra first before collecting samples, however, this remains to be demonstrated experimentally. In the next chapter, foil M171 will be used

to study the medical applications of this collected $^{225}$Ac by irradiating cells with alpha particles.

# Chapter 4

# Studying the Radiobiological Effects of Alpha Particles

Despite the gathering momentum behind TAT, the biological effects of alpha radiation are still not fully understood. This is in part due to a lack of accessible and accurate research methods [35]. Contrary to electron, photon and proton therapy, in vitro studies of TAT are challenging due to the short path lengths of alpha particles in water (<100µm). In this work, we present a novel approach for in-vitro alpha-particle dosimetry studies that requires access to neither radio-pharmaceuticals nor specialized equipment.

The scheme by which these irradiations were performed is shown in figure 4.1. The idea is to suspend cells in a gel close to the interface with air, and thus in range of an external source of alpha particles. Before discussing more details, a closer look at collagen is warranted, since it is key in the sedimentation process that allows cells to be suspended in this gel. Collagen is the most abundant protein found in the human body and it consists of amino acids that form a triple helix structure or fibril. In sufficient concentrations, they can polymerize to form stable three-dimensional matrices. These serve as the main structural component of many tissues in mammals. As such, it provides a good environment to simulate conditions in the human body[36].

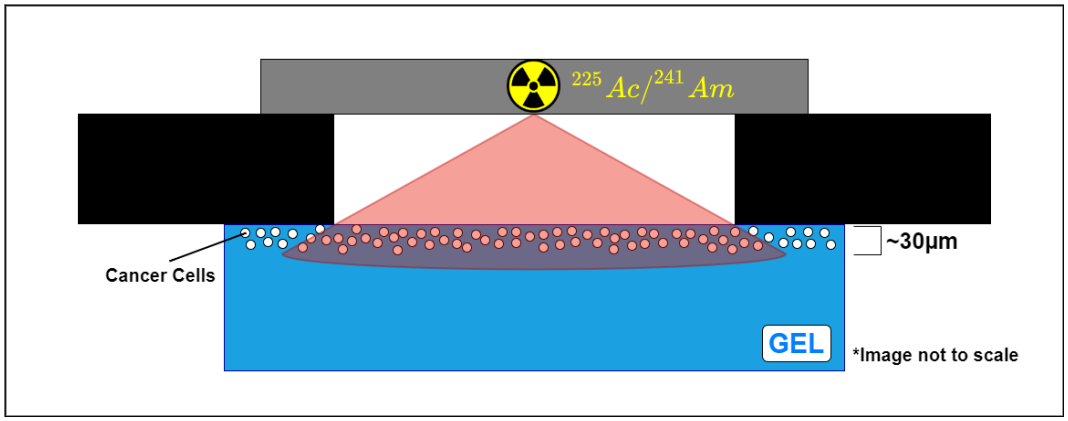


Figure 4.1: Schematic representation of the irradiation scheme on which development of the setup was based.

It is possible to keep watery solutions containing such collagen at low temperatures in which the collagen itself stays mobile and won't polymerize. Such a solution can then be poured into a mold and left to heat up. As the temperature increases, the collagen fibrils will start to cross-link and form the 3D matrix structure. A gel, closely resembling the structure in some human tissues is the end result. This process is illustrated in figure 4.2.

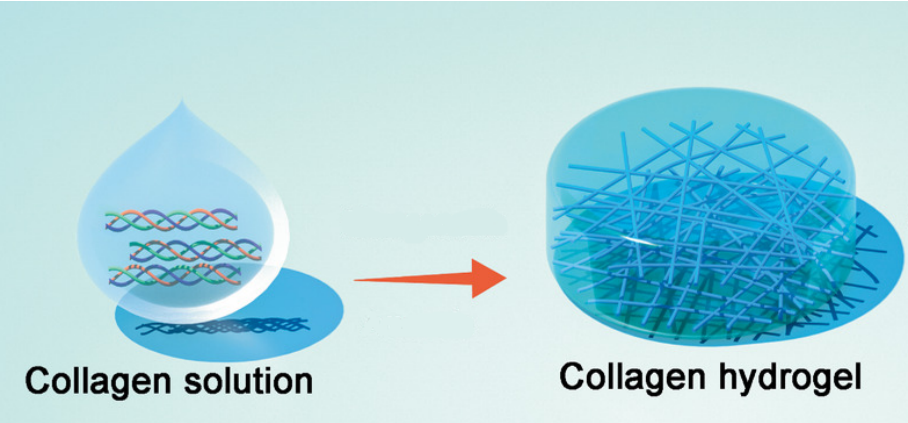


Figure 4.2: Polymerization of collagen resulting in a 3D matrix which is able to support and suspend cells for research. Figure adapted from [36].

By mixing cells with the solution before polymerization, they can use the collagen fibrils as anchoring points when the hydrogel forms. This process results in a gel with suspended cells throughout its volume, similar to biological tissue. By keeping the gel in contact with a suitable liquid medium, these cells can be kept alive for extended periods of time. Such a medium serves to keep the gel hydrated and to provide necessary nutrients. Insufficient hydration would result in a collapse of the 3D-matrix and eventual cell death.

These hydrogels were the inspiration for a new method of alpha dosimetry. If one could be made in a way that the cells would be accessible by alpha particles, any external source could be used to irradiate them. For this to happen, the gel would either need to be thin enough so that alpha particles could penetrate the entire volume, or cells would have to be suspended sufficiently close to the gel-air interface. The latter was achieved by ensuring a long enough polymerization process so that cells could sediment to the bottom of a collagen solution before being fixed in place by the solidifying gel. Further discussion of this topic will follow in section 4.2.

Hydrogels for this work were realized by Lens Dedroog and Olivier Deschaume of the KU Leuven Laboratory for Soft Matter and Biophysics. A method of sedimenting cells close to the air-gel boundary was developed. Therefore a setup was designed with the criteria of positioning a source as close to the gel as possible, without direct contact. In this way, the energy loss of alpha particles in air was minimized while reducing contamination hazards.

## 4.1 DIRAC, From Concept to Reality

Design specifications for the setup were laid out and the main features would have to include:

- The ability to bring alpha sources into close proximity of a gel in a safe and reproducible way
- The ability to control the distance between source and gel with micrometer precision
- The capability to house both standard (NIST) circular sources of 25 mm diameter and 15x25 mm MEDICIS foils

Design work started with a 3D model, developed to satisfy these requirements. A concept was chosen that would allow a hydrogel to be irradiated from above as shown in figure 4.1.

The 3D model was iterated over time until a satisfactory design was reached. A technical drawing, shown in figure 4.3 was then made and submitted for manufacturing by the mechanical workshop of the Department of Physics and Astronomy. The completed setup is shown in figure 4.4.

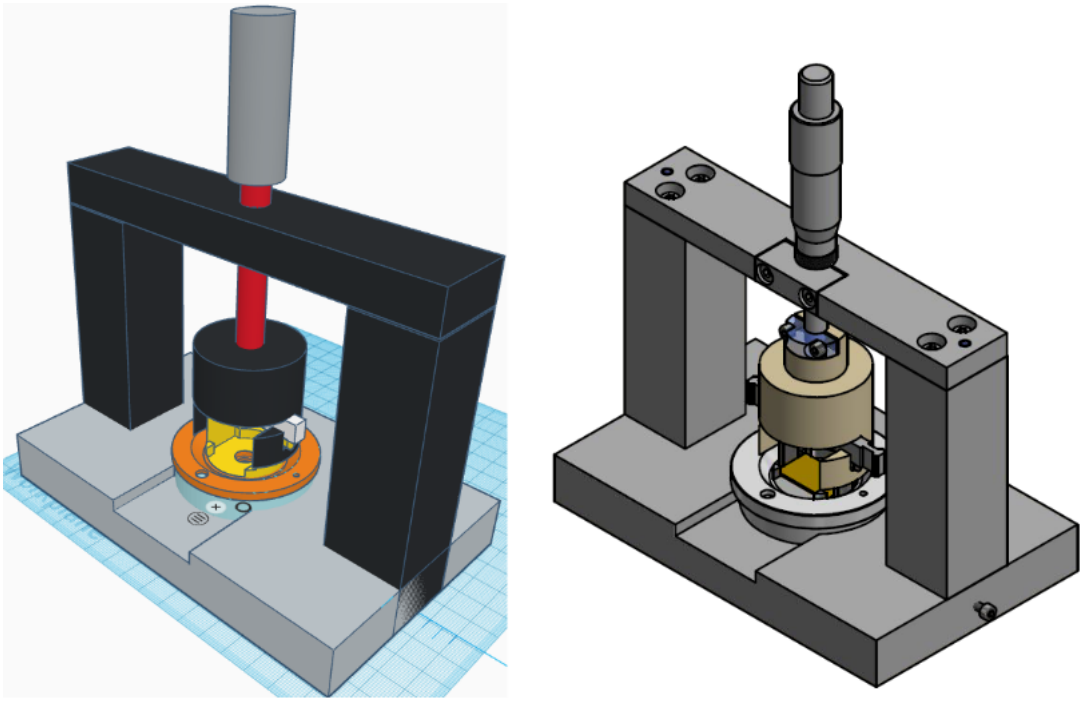


Figure 4.3: Initial 3D model of the setup (left) and technical drawing used during manufacturing (right).

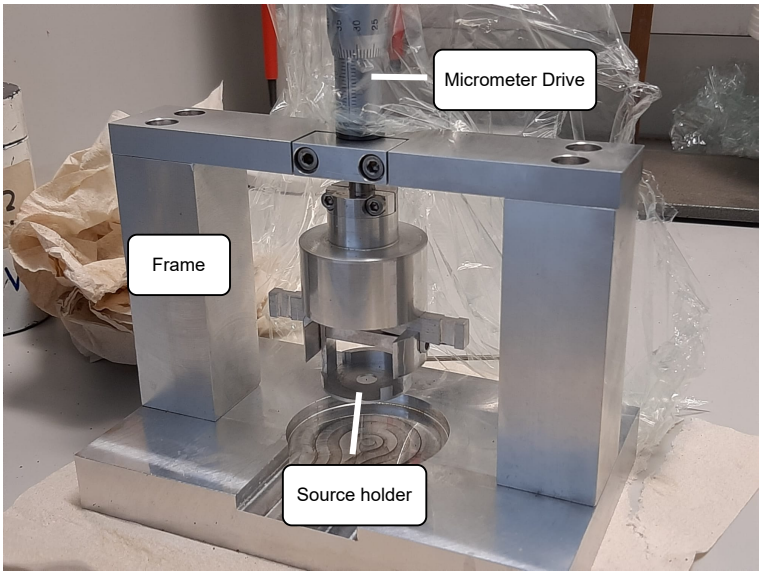


Figure 4.4: Finalized setup with inserted source holder, held in place by 2 wedges.

The setup consists of 3 major parts: first, a frame with a movable centre piece attached to a micrometer drive; secondly, a source holder able to house both circular sources of 25 mm in diameter and MEDICIS foils of 15x25 mm dimensions. This holder can be inserted into the centrepiece, held in place by wedges. It allows sources to be moved up and down with micrometer precision. The collimator in the centre of the holder is 7 mm in diameter and the bottom plate has a thickness of 1.27mm. The thickness of this plate also sets the limit on how close a source can be brought in proximity to a gel.

A cover made to fit petri dishes of 27 mm in diameter constitutes the final part. It features a central part in which collagen solutions can be cast. To allow a gel to be fed and hydrated from below, the cover is lowered into a petri dish filled with medium after gel preparation. Additionally, some holes are present to refill medium when necessary. After initial testing of the components, the setup was finalized during the month of February 2022. It was baptized as the DIRAC setup for Direct IRradiation with Alphas on Cells. Additionally, a risk assessment for irradiations with this setup was made which is included in appendix C.

## 4.2 Development of a Cell Irradiation Protocol

Before consistent experiments with the DIRAC setup could be carried out, it was necessary to develop a robust protocol. An overview of a finalized version used during cell irradiation is shown in figure 4.5. The steps will be thoroughly discussed in the following sections.

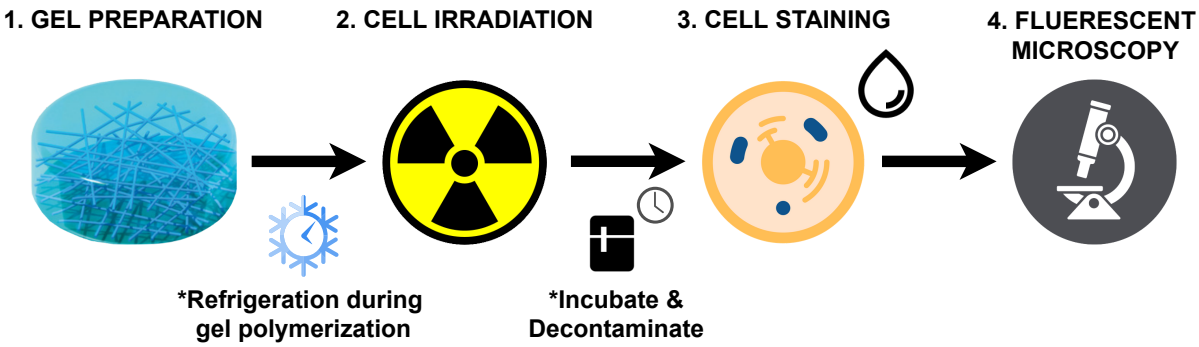


Figure 4.5: Schematic of the protocol by which cell irradiation experiments were performed.

Every cell irradiation experiment starts with hydrogel preparation. Collagen is mixed with unmodified HELA cancer cells procured from the UZ St-Rafael hospital and cast into a petri dish cover. Solutions with a collagen concentration of 1.5 mg/ml were used in this process. The speed at which the 3D-matrix forms defines how long cells have to sediment before being fixed in place. This is a temperature-sensitive process, which caused unsatisfactory sedimentation to be observed with rising ambient temperatures during Spring. Gels were henceforth refrigerated after preparation to slow down the polymerization process. The hydrogel-cell solution was kept at 4°C for 30 minutes and then at 37 °C for 30 minutes. In this way, satisfactory sedimentation for cell irradiation was observed.

After sedimentation, the covers are placed on petri dishes filled with medium. Its purpose is to minimize non-radation-induced cell death between irradiation and imaging. After inserting the petri dish and hydrogel-containing cover into the setup, the empty source holder is lowered onto the gel. It was observed that pressure on the cover could cause the medium to rise up through the gel. To avoid contact with liquids, sources are only inserted after visual confirmation that the holder did not come into contact with any medium. Additionally, as part of contamination mitigation, trials were performed with dummy sources made of paper to make sure that sources would not come into contact with liquid medium. After a technical incident that rendered foil M171 unusable, the practice of cleaning the source holder with ethanol between experiments was also adopted.

Two types of alpha sources were procured for cell irradiation. One source was the accelerator produced and mass-separated $^{225}$Ac source M171, whose characterization is described in section 2.3. Additionally, four $^{241}\mathrm{Am}(T_{1/2} = 432.2Y)$ sources of varying activity were made in-house with a liquid solution of $^{241}$Am(III)Chloride. An in-depth discussion of these sources will follow in section 4.4.

With a half-life of 9.92 days, $^{225}$Ac has the advantage that dose-rate-escalation studies can be performed by waiting in between each measurement. Because daughter nuclei recoil out of foil M171 though, decontamination time is necessary in between irradiation and imaging. This time is constrained by the half-life of the longest-lived daughter, being $^{213}$Bi with $T_{1/2} = 45.6$m. Samples were left in the incubator overnight for at least 15 hours and were checked with a surface monitor before being cleared. In the end, observed activity after a day was higher than expected, probably originating from sputtering of $^{225}$Ac at the surface of the foil. Nevertheless, activities were deemed safe by radio-protection services.

The $^{241}$Am sources on the other hand are long-lived and provide a constant source of alpha particles. Moreover, the absence of daughters recoiling out the source removed the need for a decontamination protocol and allowed for immediate imaging only 2-3 hours after irradiation.

Environmental factors such as humidity, temperature and airflow can have a profound effect on cell survival rates. Every irradiated sample was thus accompanied by at least one control sample for comparative analysis. Since samples were irradiated in a fume hood, cling film was wrapped around the setup during an experiment to prevent the airflow from dehydrating a gel. After irradiation, cells are submerged in medium and incubated to ensure minimal non-radiation-induced cell death in between irradiation and imaging.

Half an hour before microscopy, two types of dye are added to the samples. One (Calcein AM) which is only fluorescent in metabolically active cells and another (Ethidium Homodimer) cell-impermeant one that becomes fluorescent when bound to the DNA of dead cells. These two dyes fluoresce following absorption of light in different wavelength ranges, allowing for live and dead cells to be distinguished. When the dyes have had time to interact with their targets, samples are brought to a fluorescence microscope for imaging. Different wavelengths of light are shone upon the sample and images of the resulting fluorescence are taken for later analysis. After the imaging is completed, petri dish covers are submerged in an ethanol solution to cleanse them for later use.

The next sections of this work will focus on providing more context to this protocol. Section 4.3 will investigate the viability of the irradiations via simulations of the setup and by determining cell depth in a sample. A thorough discussion of the utilized $^{241}$Am sources will then follow in section 4.4. Finally, image analysis and the result of the experiments will be discussed in sections 4.5 and 4.6 respectively.

## 4.3 Simulating the DIRAC Setup with Geant4

To understand the behavior of alpha particles in a gel sample, simulations of the DIRAC setup were made. Geant4, an extensive toolkit for the simulation of particles through matter, was chosen for this task [37].

The decay chain of $^{241}$Am is shown in figure 4.16. Due to the very long half-life of its daughter $^{237}$Np, it features only one relevant decay[38]. Moreover, shielding on used sources prevents the redistribution of daughter isotopes contrary to foil M171. Simulations of $^{241}$Am will hence be discussed first. For the source geometry, a uniform circular source with a radius of 1 mm was assumed. Energies for the alpha particles after traversing the source shielding were obtained from later characterization in section 4.4 and determined to be $\sim$5.35 MeV. Isotropic emission was assumed but only half the solid angle facing towards the gel was considered to improve computational efficiency.

The setup geometry was simulated by the bottom plate of the source holder with a collimator of 7 mm in diameter. Under this plate, the gel is modelled as 9 layers of water,

each of 10 µm thickness representing roughly 1 cell diameter. For every simulated particle, the entry and exit points in these layers were recorded as well as their path lengths and deposited energies. A visualization of the simulation can be seen in figure 4.6. In this configuration, the trajectory and interaction of 100,000 alpha particles were simulated.

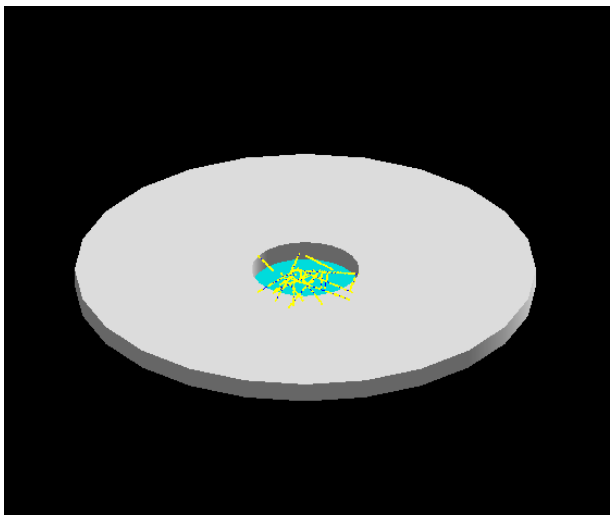

Figure 4.6: Visualization of a Geant4 simulation with tracks of alpha particles indicated in yellow. The source holder plate is indicated in grey with the layers of gel in cyan.

The energy loss or stopping power of a charged particle with energy $E$, traversing a distance $x$ through a target material, is described by the Bethe formula (4.1).

$$-\frac{dE}{dx} = \frac{4\pi}{m_e c^2} \cdot \frac{nz^2}{\beta^2} \cdot \left(\frac{e^2}{4\pi\epsilon_0}\right)^2 \cdot \left[ln\left(\frac{2m_e c^2 \beta^2}{I \cdot (1-\beta^2)}\right) - \beta^2\right] \tag{4.1}$$

Alpha particles are heavy and slow compared to other types of conventional nuclear radiation, never reaching more than ∼5-7% of light speed. Allowing the use of the non-relativistic version of the formula (4.2).

$$-\frac{dE}{dx} = \frac{4\pi n z^2}{m_e v^2} \cdot \left(\frac{e^2}{4\pi\epsilon_0}\right)^2 \cdot \left[ln\left(\frac{2m_e v^2}{I}\right)\right] \tag{4.2}$$

With $e$ and $m_e$ the electron charge and rest mass, $v$ the speed of the charged particle and $\epsilon_0$ the vacuum permittivity. $I$ and $n$ represent the average ionization potential and electron number density in the target material respectively.
As soon as particles enter the gel, the only variable at play is the speed $v$ on which the formula has a $ln(v^2)/v^2$ dependency. Meaning that the less velocity a particle has, the more energy it will lose per unit of distance travelled. A particle's stopping power will hence grow until eventually it is stopped and a sudden drop ensues. The characteristic Bragg peak, which is the result of this behavior, can be illustrated by plotting the simulated energy loss in the layers of gel. For this purpose, the energy losses of particles at incoming angles of 0 and 45 degrees are shown in figure 4.7.

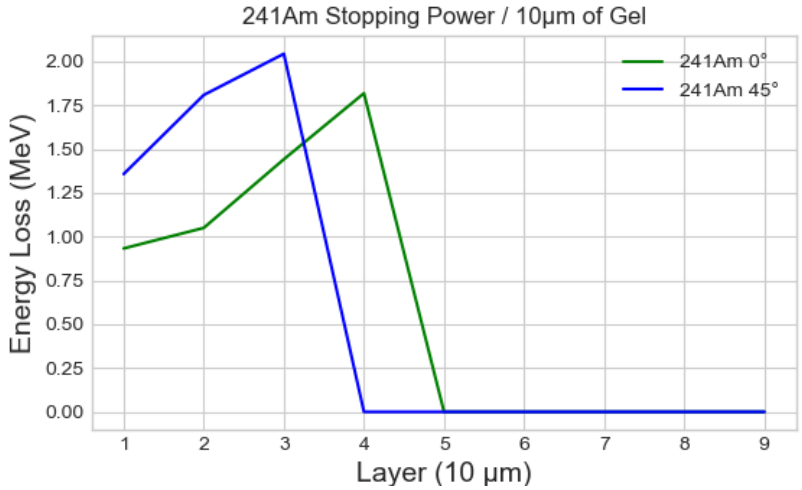


Figure 4.7: Energy loss of $^{241}$Am alpha particles travelling through 10 µm gel layers at 0 and 45 degree angles relative to the surface.

The Bragg peak can be observed as well as the difference between a particle emitted at a right angle or 45 degrees onto the gel. A shallower angle results in longer path lengths through each layer and thus more energy loss per layer. This causes the particles emitted at 45 degrees to be stopped in the third layer already while the others were stopped in the fourth.

Two-dimensional histograms were constructed to visualize the absorbed dose by each layer. For these, the average of the entry and exit points in a layer were used as coordinates while deposited energy was taken as the weights. Absorbed doses were distributed among a 40x40 grid with each square representing 0.2x0.2 mm to form the end result shown in figure 4.8. The source was taken as a 4 kBq $^{241}$Am source and the equivalent of 2 hours of irradiation was modelled.

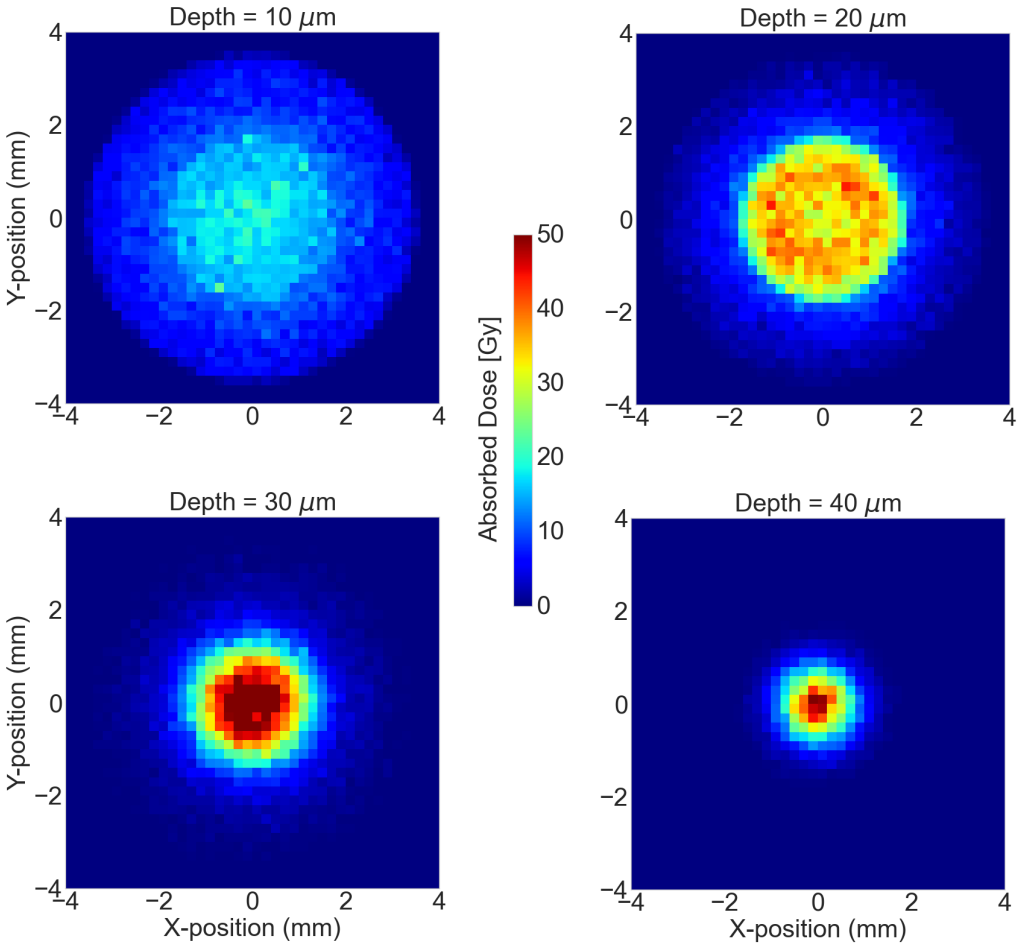


Figure 4.8: Absorbed energy in different gel layers displayed in a 2d histogram. Every pixel represents 0.2x0.2 mm and is weighted by absorbed dose in Grays. The Gray [Gy] is a derived unit of absorbed dose defined as $J \cdot kg^{-1}$ and 1 Gy is equal to 100 rad. Irradiation was simulated for a 4 kBq $^{241}$Am source and a duration of 2 hours.

The previously discussed Bragg peak is visible in these images, with the collimator defining the area at 7 mm in diameter. Cells in the center of a sample can be irradiated deeper in the gel, while shallower depths receive a more uniform dose over a larger area. For any cells to be irradiated at all by $^{241}$Am alpha particles, they would have to settle within the first 40 micrometers of the gel.

These results will now be compared to simulations of the $^{225}$Ac source used in experiments. The recoiling daughters emitted in the decay chain make this task more complex. Range simulations were performed in Geant4 for $^{221}$Fr with a kinetic energy of 100 keV in air. An average range of less than 100 µm was obtained. After these particles are stopped right outside of the foil, Brownian motion will dominate their further movement. A sizable portion will hence diffuse onto the gel and collimator, complicating simulations. A first-order approximation was made to model the resulting spatial distributions of daughter nuclei. The results of this approximation are shown schematically in figure 4.9, of which a description will now be provided.

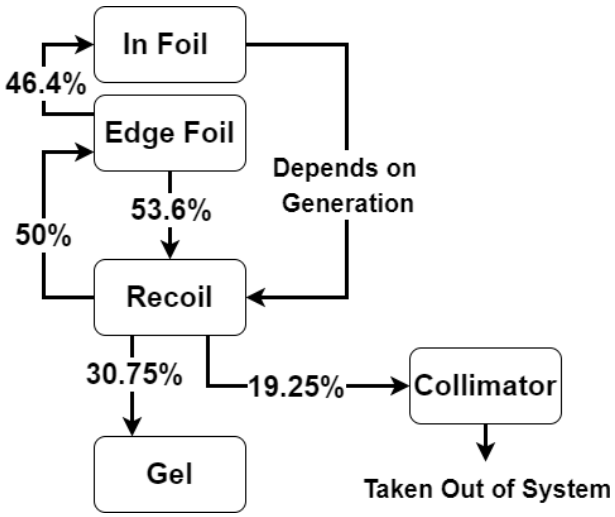


Figure 4.9: Scheme used to approximate the destination of a recoil before its decay.

For nuclei inside the foil, the probability of the daughter recoiling out of the foil is determined by its generation. Since recoiling daughters can also be stopped deeper into the foil, the probability of daughter recoil is reduced with each subsequent generation. Numbers of 53.6% for $^{221}$Fr, 27.6% for $^{217}$At and 14.3% for $^{213}$Bi were obtained from simulations by Heines [28]. More than 50% of the particles recoil out at the surface due to backscattering. In this process, a particle can be emitted towards the foil yet scatter and end up with a resulting displacement towards the foil-air interface.

If a daughter recoils out, it is assumed that it stops right outside the foil after which Brownian motion takes over. This motion was assumed to be isotropic and was simulated by radially projecting outwards from a Gaussian source of $\sigma$ =1.175 mm corresponding to the typically scanned beam profile in MEDICIS. These radial projections resulted in probabilities of 50% to diffuse back on the outer edge of the foil, 19.25% to settle on the collimator and 30.75% to settle on the gel. Particles that settle on the collimator are no longer considered while particles that settle on the gel are assumed to complete their decay chain there. If a particle settles on the outside of the foil, it 'joins' the population of first-generation daughters with a 53.6% chance to recoil out in the subsequent alpha decay.

Fractions of all isotopes in each location were calculated with this scheme. By normalizing them to the population of $^{225}$Ac on the sample, the results in table 4.3 were obtained.

Table 4.1: Fractions in percent of each isotope and their location after diffusing in the setup. All numbers are normalized to the original $^{225}$Ac population and $^{213}$Po was adjusted for the 97.8% branching ratio of $^{213}$Bi.

| Isotope | Fraction on foil [%] | Fraction on Gel [%] | Fraction on Collimator [%] |
|---|---|---|---|
| $^{225}$Ac | 100.00 | 0.00 | 0.00 |
| $^{221}$Fr | 73.20 | 16.48 | 10.32 |
| $^{217}$At | 59.61 | 24.84 | 15.55 |
| $^{213}$Bi | 52.68 | 29.10 | 18.22 |
| $^{213}$Po | 51.52 | 28.46 | 20.02 |

Finally, simulations with 40.000 emissions from each isotope were performed. Percentages listed in table 4.3 determine the chance for a particle to be emitted from either the foil or the Surface of the gel. To find the distribution of daughters on the gel, 10.000 particles were radially projected outwards like before with a Gaussian source of $\sigma$=1.175 mm. Positions, where particles hit the gel, were recorded and the result along the x-axis, shown in figure 4.10 agreed well with a Gaussian fit of $\sigma$ =1.628 mm. It was obtained via chi-squared minimization of a centroid $\mu$, standard deviation $\sigma$ and amplitude $A$. Emission on the gel was henceforth simulated by a source of the same standard deviation.

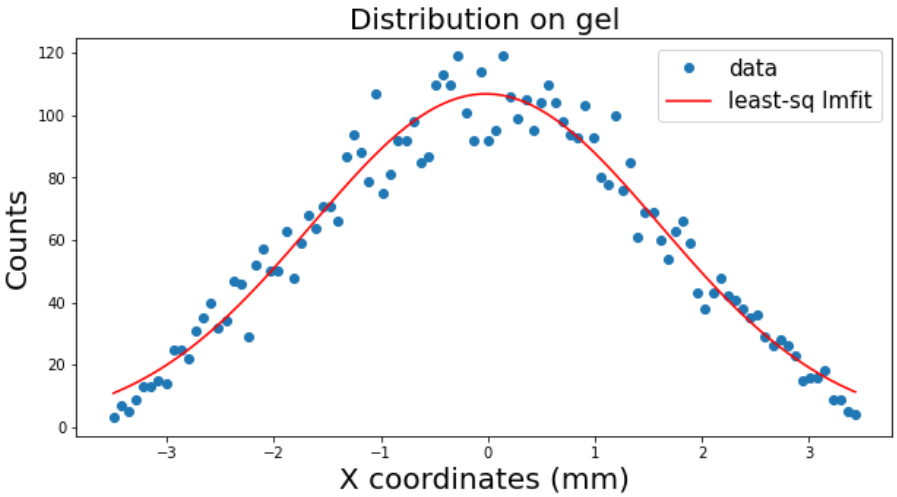


Figure 4.10: Fit of the distribution on a gel from isotropically emitted particles by a Gaussian source of $\sigma$ =1.175 mm.

Daughter isotopes of $^{225}$Ac emit alpha particles with energies that exceed those from the decay of $^{241}$Am. Combined with a fraction decaying on the surface of the gel, this results in alpha radiation from sample M171 having longer track lengths. Simulated energy losses from the main daughter isotopes are shown in figure 4.11.

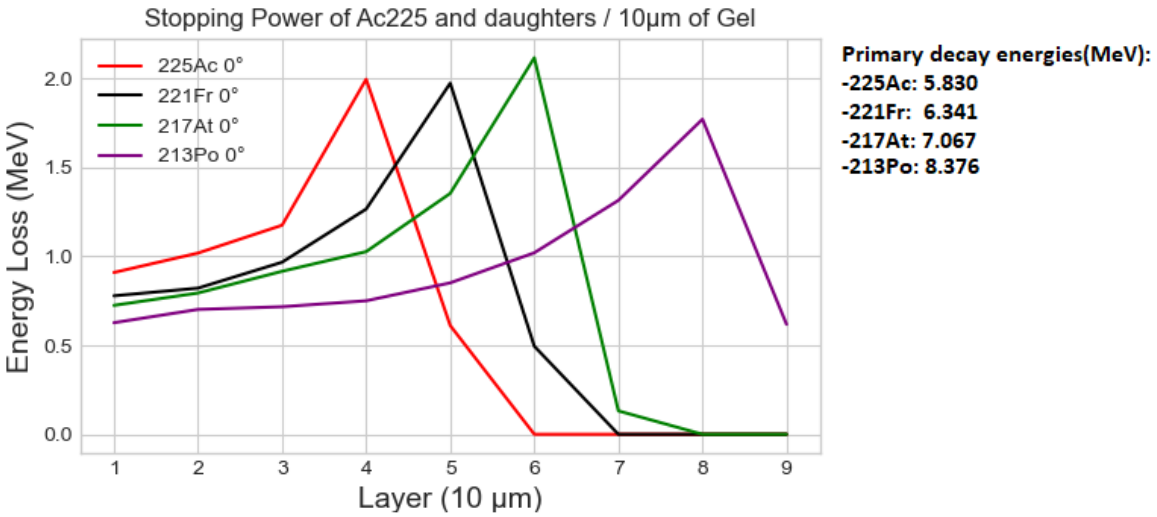


Figure 4.11: Energy loss of alpha particles from $^{225}$Ac and main daughters distributed on gel. They were simulated by a Gaussian source of 1.628 mm and relative populations are given by table 4.3. Each layer corresponds to 10um of hydrogel (water).

The energy loss from the alpha decay of $^{213}$Bi was omitted from this graph due to its low branching ratio and similar decay energy to $^{225}$Ac. Its decay is included in the simulations, however. For the other daughters, Bragg peaks much deeper in the gel can be observed. Alpha particles from the decay of $^{213}$Po even reach into the last simulated layer before being stopped.

Two-dimensional histograms were constructed in an identical way to the simulation of the $^{241}$Am source. The activity of $^{225}$Ac was taken as predicted by the coincidence measurements at the time of the first experiment. Resulting in a simulation of a 706.4 Bq source irradiating a gel for 3 hours. The dose absorbed in each layer in Grays is once more shown in figure 4.12.

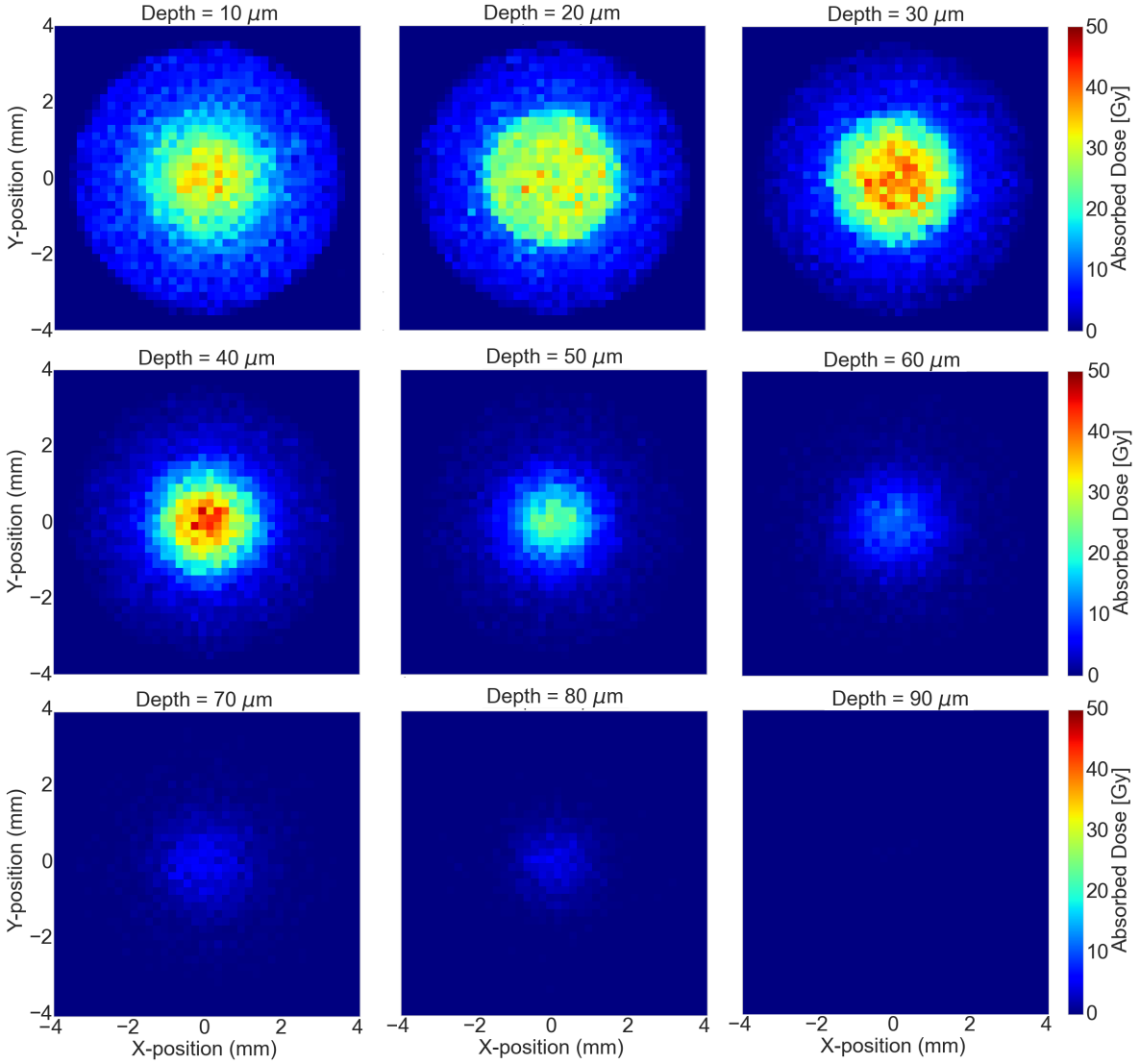


Figure 4.12: Absorbed energy in different gel layers displayed in a 2d histogram. Every pixel represents 0.2x0.2 mm and is weighted by absorbed dose in Grays. Irradiation was simulated for a 706.4 Bq $^{225}$Ac source and a duration of 3 hours.

Interplay between the various daughter isotopes, different geometry and differing decay energies paints a dissimilar picture compared to the $^{241}$Am source. The dose is distributed more evenly in each layer, being significant up to the 6th one with residual energy deposits from the $^{213}$Po decay reaching even further. This leads to the conclusion that the two sources must not be considered as interchangeable. Furthermore, many assumptions were made to construct the simulation of foil M171. In reality, a more complex Brownian motion, decay from the collimator as well as secondary recoils back out of the gel would have to be taken into account. The end result of which would be an even more evenly distributed dose than displayed in image 4.12.

In order to obtain meaningful insight into the dose actually received by cells, it is imperative to know how deeply they are sedimented in the gel. Confocal microscopy was performed on a test sample prepared with the latest protocol version. Two different techniques were used to image the collagen itself and the cells separately. By then comparing

the surface of the collagen to the depth of the cells, information on where they situate themselves could be obtained. Further details on the used settings and microscope can be found in appendix A.

To image the cells, fluorescent microscopy was performed by injecting the sample with a calcein-AM dye. This dye is converted to a fluorescent material in metabolically active cells. Fluorescence wavelengths are 496 nm and 516 nm for excitation and emission maxima respectively, which corresponds to blue visible light. Light from excitation and emission goes through band-gap filters so only the emitted light is detected by the microscope. Fluorescence photons can hence be detected at different wavelengths as shown in figure 4.13a. Since the dye only becomes fluorescent in metabolically active cells, these emissions can be used to count live cells.

To image the collagen, a different technique called 'Second Harmonic Generation microscopy' was used. When two photons induce dipole excitations in a material of non-linear polarizability, there is a probability that they combine into a photon with double the frequency or half the wavelength. This effect is known as Second Harmonic Generation (SHG) and is illustrated in figure 4.13b. The structure of collagen fibrils has effective non-linear susceptibilities and microscopes can use the second harmonic light generated to image them [39].

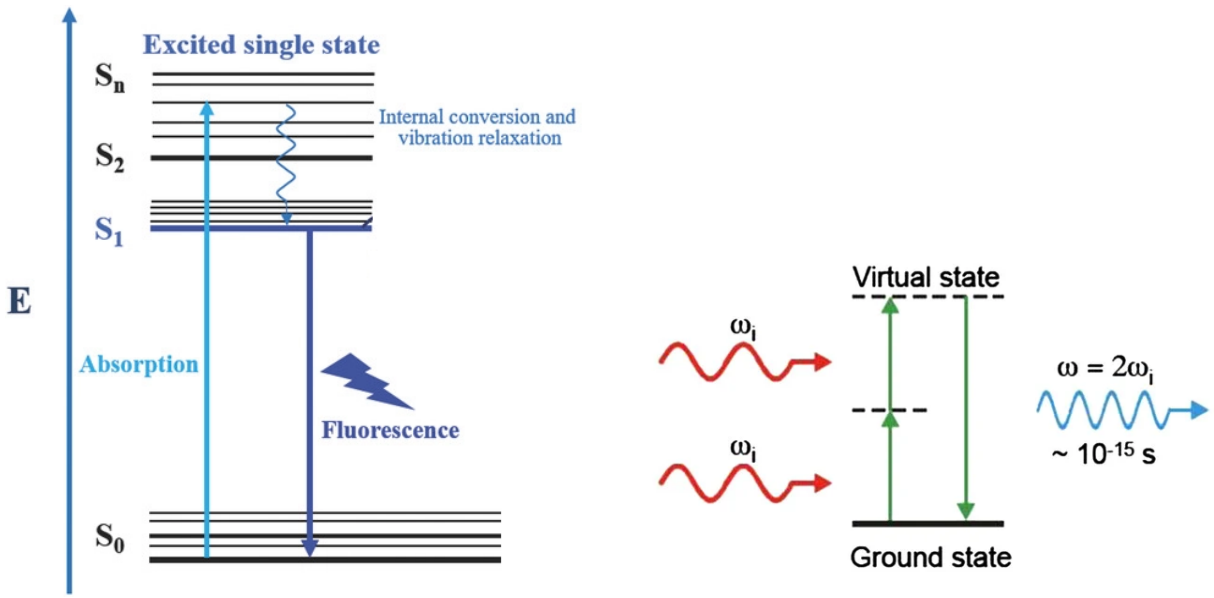


(a) (b)

Figure 4.13: Physical effects used to perform confocal microscopy: (a) Fluorescence [40] (b) Second harmonic generation[41].

Regions of a sample were scanned along the vertical axis with 2 µm increments. Imaging started above the collagen and ended after no cells were detected anymore. Afterwards, the first layer with collagen was compared to the layer with the centroids of the first cell layer. By imaging 6 regions this way, an estimate could be made of how deep the cells situate themselves in the gel. Example images of a region are shown in figure 4.14 and the results of these measurements are listed in table 4.3.

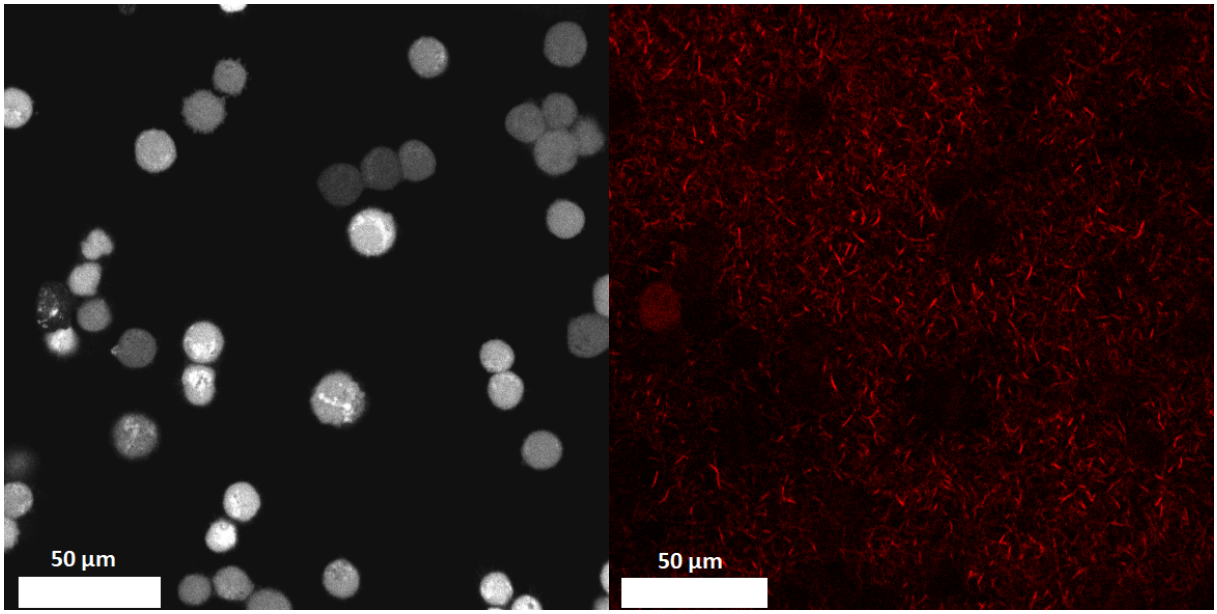


(a) (b)

Figure 4.14: (a) Cells imaged using fluorescent microscopy (b) Collagen imaged using second harmonic generation photons.

The images shown in figure 4.14 are of the same region and depth in the sample. Holes in the collagen indicate locations of cells or their sedimentation tracks. Moreover, stacks of images from both techniques along the vertical axis can be overlapped to reconstruct a 3D image. Cells from the sample, sitting in a 3D reconstruction of the collagen are shown in figure 4.15.

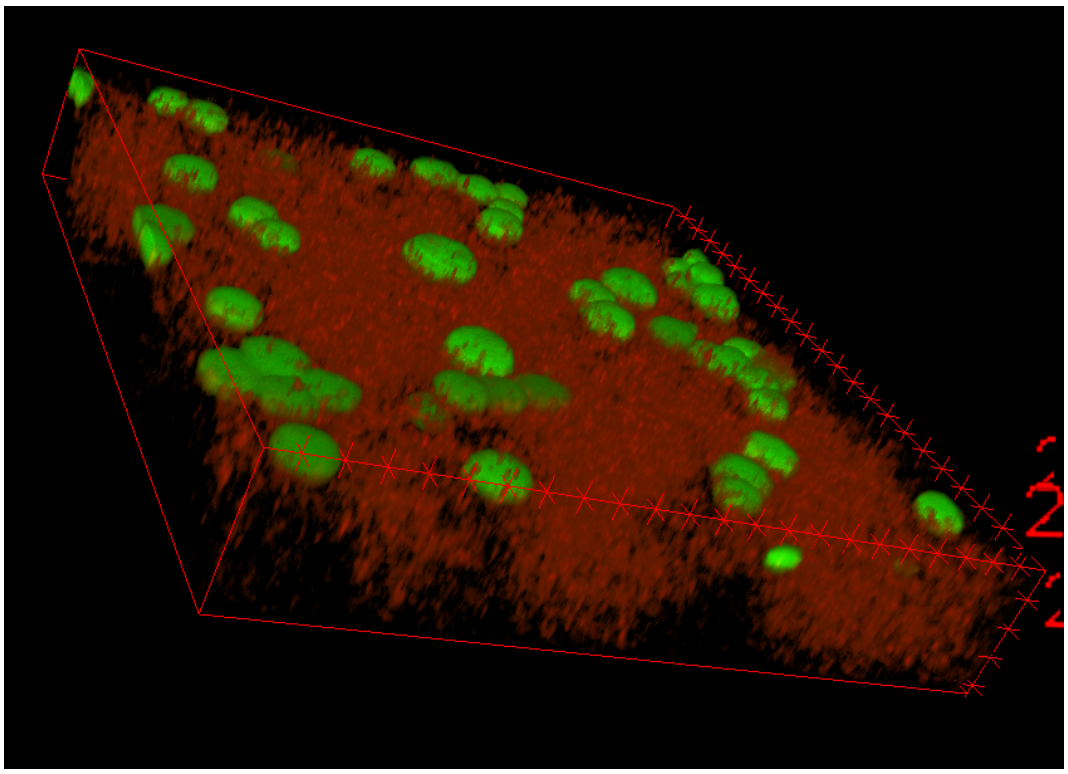

Figure 4.15: 3D representation of cells in a gel sample. Collagen is indicated in red while cells are indicated in green. The dimensions of the displayed box are 230x230x80 µm. It can be observed that most cells sediment within the first 20 micrometers after the collagen appears at the surface. The cells are thus within range of alpha particles impacting on the gel.

Table 4.2: Confocal microscope data

| First layer with collagen | Layer with centroids of first cells | Depth of first cells [µm] |
|---|---|---|
| 6±1 | 12±1 | 12.00±2.82 |
| 4±1 | 10±1 | 12.00±2.82 |
| 9±1 | 16±1 | 14.00±2.82 |
| 4±1 | 9±1 | 10.00±2.82 |
| 7±1 | 13±1 | 12.00±2.82 |
| 8±1 | 14±1 | 12.00±2.82 |

Average Depth = 12.00±2.82 µm

Compared to simulations, the majority of cells situate themselves in the second 10 µm layer. Furthermore, no cells were detected more than 13, 2 µm confocal layers behind the collagen. In conclusion: All cells sediment in the second and third simulated layers, with the vast majority situated in the former. Simultaneously, this is the optimal depth for both $^{241}$Am and $^{225}$Ac samples as it offers a large dose in both intensity and area.

Through simulations and microscopy, it has been shown that the developed protocol produces samples suitable for irradiation. In the next section, the characterization of sources used for these experiments will be discussed. Since sample M171 has already been analyzed in detail, this leaves only the sources of $^{241}$Am.

## 4.4 Characterizing Sources of $^{241}$Am

With the short half-life of the activity on foil M171 and its eventual disposal, it was deemed necessary to perform experiments with another source. The radionuclide chosen for this task is $^{241}$Am, a pure alpha emitter just like $^{225}$Ac. Sources of this isotope were readily available and custom ones could be manufactured in-house. Aside from these benefits, it was chosen for several reasons.

First of all, the half-life of this isotope is larger at $T_{1/2} = 432.6Y$ compared to the 9.92 days of $^{225}$Ac. Any decay over short time frames can hence be considered as negligible. While practical, the longer half-life does pose a possible contamination risk. Unlike $^{225}$Ac, waiting for contaminated materials to decay on their own is not an option. Extra care thus has to be taken to not spread any of the material around. Furthermore, when ingested, $^{241}$Am is an effective carcinogenic and so-called "surface seeker" which tends to settle on bones and in the liver [42].

Secondly, there is the decay chain shown in figure 4.16. While $^{241}$Am eventually decays to $^{225}$Ac, its daughter isotope $^{237}$Np has a half-life of over two million years. If the most powerful employed source (∼4 kBq) would decay for a century and all Neptunium would be collected, the resulting radiation from the Neptunium would only be of the order of ∼0.1 mBq. Since this is significantly lower than the uncertainties on these sources, effects from daughter nuclei can be considered as negligible. Furthermore, no daughter has sufficient energy to recoil out of any of the employed sources. This is in contrast to $^{225}$Ac which has multiple short-lived daughter isotopes and sample M171 where daughter nuclei recoil out in large numbers.

In summary, $^{241}$Am was a convenient source to procure and offered a suitable and constant source of alpha particles. With no risk of contamination by daughter isotopes, samples could be safely handled and imaged directly after irradiation.

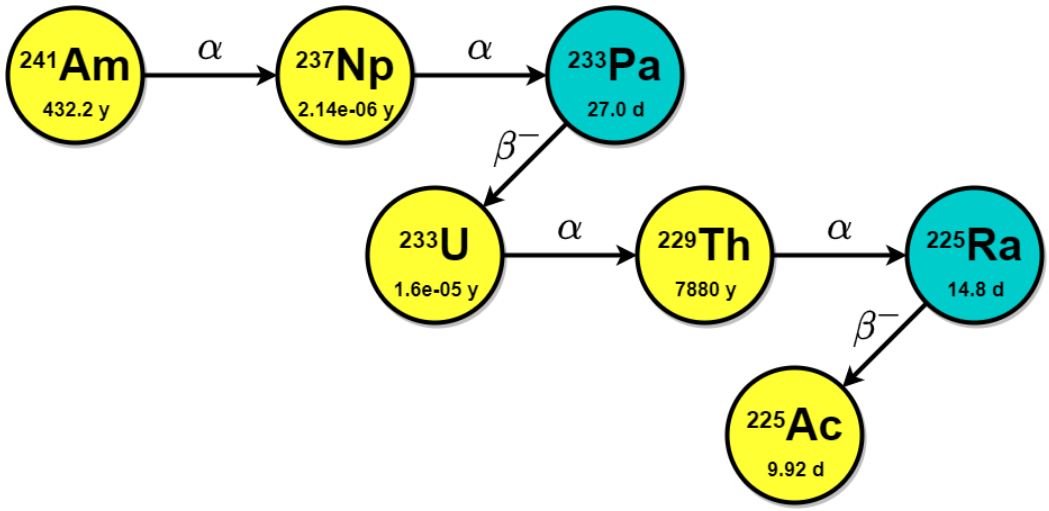


Figure 4.16: Decay chain of $^{241}$Am color coded in yellow and blue for $\alpha$ and $\beta^-$ decay respectively. Half lives are indicated in the bottom. The rest of the decay chain can be followed from the $^{225}$Ac decay onwards in figure 2.1.

Utilized sources of $^{241}$Am included four in-house manufactured ones for irradiation purposes and a fifth one with an activity of 50 Bq which was only used only for calibration purposes. It consists of a disc, 25 mm in diameter on which $^{241}$Am is Gaussian distributed in its center over a circle with a radius of 3.5 mm. This distance corresponds to two times the standard deviation.

While the source was produced to have an activity of 50 Bq, it was acquired non-calibrated and the manufacturer only gave a rough assurance of a maximal error of up to 30%. This necessitated measurements to determine its exact activity which was done via alpha spectroscopy in the ASET

To find the activity of a source, its relation to the count rate by the detector has to be known, which is given by equation 4.3.

$$\varepsilon_{Tot} = \frac{N}{A} = \varepsilon_{Geo} \cdot \varepsilon_{Int} \tag{4.3}$$

Here, $\varepsilon_{Tot}$ represents the total efficiency or the ratio of particles detected compared to particles emitted by the source. $\varepsilon_{Geo}$ is the geometric efficiency or the ratio of particles that impact on the detector compared to the emitted particles. Finally, $\varepsilon_{Int}$ represents the intrinsic efficiency or the number of particles counted by the detector compared to the amount that impacts on it. N and A represent the detector count rate and activity of the source respectively.

Unlike many other spectroscopic methods, Silicon-based detectors have a near 100% intrinsic efficiency for the detection of alpha radiation. This is the case because almost every alpha particle impacting on the detector is stopped in the active area and will thus induce an electric signal. This results in the geometric efficiency being the biggest contributor to the uncertainty when measuring activities.

It is of great importance to determine the geometric efficiencies as accurately as possible after the physical distances have been confirmed. If a source is positioned far enough from a detector, a point source approximation is typically used.

$$\varepsilon_{geo} = \frac{1}{2}\Big(1 - \frac{d}{\sqrt{r^2 + d^2}}\Big) \tag{4.4}$$

With $d$ the distance between source and detector and $r$ the detector radius. This is appropriate if the distance between source and detector is sufficiently larger than the source radius. During the measurements for M171 however, this was not the case since those distances were of the same order of magnitude. This meant that the size of the source and its distribution have to be taken into account. To do this, another piece of code written by Michael Heines was used [29]. This code uses Monte Carlo methods to determine a random starting point and direction of a particle given a source distribution. Since alpha particles travel in a straight line through a vacuum, a line can be drawn to determine whether the emitted particle would hit the detector. By repeating this process for many particles ($10^8$ for the calculations in this work), the geometric efficiency can be accurately determined given certain dimensions. The code supports uniform circular

sources and Gaussian distributed ones. A visual representation is shown in figure 4.17.

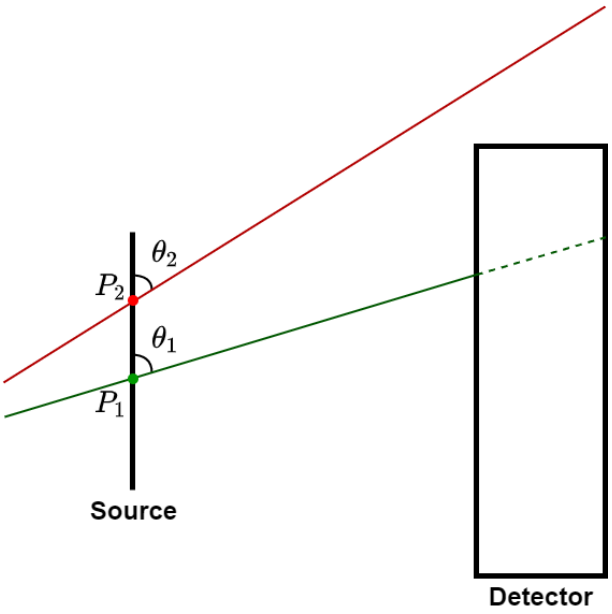


Figure 4.17: Visual representation of the code used to determine geometric efficiency. Points and angles are chosen on the detector surface via Monte Carlo methods depending on the source distribution. A line is drawn and the code checks whether it impacts on the detector surface or not.

To save computing time, the code only considers alpha particles emitted forwards to the detector ($\theta = 0° - 180°$). The geometric efficiency is hence calculated in the following way.

$$\varepsilon_{geo} = \frac{N_a}{2N_e} \tag{4.5}$$

With $N_a$ the particles arriving at the detector and $N_e$ the amount of emitted particles which was taken to be $10^8$ for all the calculations. The factor 2 accounts for the fact that only forward propagating particles are considered. Otherwise, double the real geometric efficiency would be calculated. The error can consequently be calculated as follows.

$$\Delta\varepsilon_{geo} = \frac{\varepsilon_{geo}}{\sqrt{2\varepsilon_{geo}N_e}} = \sqrt{\frac{\varepsilon_{geo}}{2N_e}} \tag{4.6}$$

### 4.4.1 Determining Activities of Used $^{241}$Am Sources

To determine the activity of the calibration source, alpha spectroscopy with the ASET was performed. The source was positioned in front of a Silicon surface-barrier Detector with a surface area of $300mm^2$ and distances were measured with a micrometer. Some considerations had to be taken into account when doing this, e.g. the source recessed in the ladder by $\sim 1mm$. Because the error on these measurements constitutes the largest uncertainty when calculating the activity, multiple measurements were made and an average was taken. The end result was a distance of $5.20 \pm 0.55mm$. After confirming the geometry, the ladder was placed in the vacuum chamber and it was pumped down to

a pressure of $10^{-6}mbar$. A reverse bias voltage of 60V was applied and the subsequent collection of data resulted in the following spectrum.

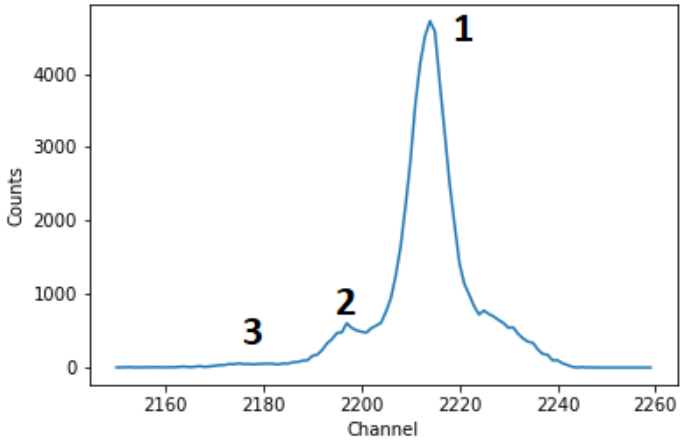


Figure 4.18: Spectrum of the $^{241}$Am calibration source. The three main peaks are indicated.

Considerable amounts of counts can be seen on the high-energy side of each peak that do not correspond with the expected shape. With a source of this relatively low activity, it is very unlikely that this is caused by pile-up effects of alpha particles. To illustrate this, assume that the dead time of the detector is $1 \cdot 10^{-6}$s and that the count rate would be 50 counts/s. Detection times were assumed to be entirely random and thus 50 random numbers between 0 and 1 were generated 3.6 million times for 1000 hours. By then checking whether these numbers are within the dead time of the detector, an estimate can be obtained which turns out to be $\sim$1 count per 10.000 seconds or roughly 1 pile-up event every 3 hours.

Instead, it is most likely the energies of emitted electrons during decay that are being summed. Since each of these events is the result of 1 alpha particle and an electron being detected, it does not change the count rate for alpha events. Hence, it is justified to include this region for the purpose of determining the activity.

Background measurements over 2 hours revealed less than 10 counts in the low energy regime. Hence, a background subtraction was deemed unnecessary. By summing over the relevant channels, 63464 alpha particles were registered over a time period of 4979 seconds. The geometric efficiency was calculated using the aforementioned code and its error by equation 4.6. Chosen parameters were a Gaussian distributed source with $\sigma = 1.75mm$, a distance of $5.20 \pm 0.55mm$ and a circular detector with a surface area of $300mm^2$ and radius $r = \sqrt{300mm^2/\pi}$. Results are listen in table 4.3.

Table 4.3: Geometric efficiencies for determining the activity of the calibration source

| $Distance[mm]$ | $Geometric\ efficiency$ [%] |
|---|---|
| 4.65 | $28.1536 \pm 0.0004$ |
| 5.20 | $26.1626 \pm 0.0004$ |
| 5.75 | $24.3129 \pm 0.0003$ |

From this, the activity of the source was calculated. The used detector was assumed to have an intrinsic efficiency of 100%, making the geometric efficiency equal to the total efficiency. The activity of the source can then be calculated with the following formula.

$$A = \frac{N}{\varepsilon_{Geo} * t} \tag{4.7}$$

With N the number of detected alpha particles and t the elapsed time during the measurements. Taking the geometric efficiencies from the previous calculations, an activity of $A = 48.66^{+3.69}_{-3.44} Bq$ is obtained. The production goal of 50 Bq thus lies well within the uncertainty of these measurements.

The previously discussed source was deemed unsuitable for later experiments due to contamination risks. Instead, four other closed sources of $^{241}$Am were manufactured in-house for this purpose. The production process begins by taking a drop of liquid Americium(III)Chloride and depositing it on a PolyEthylene Terephthalate(PET) film metalized with 40 nm of aluminium. The drop is then dried under an infrared light, leaving a residue of $^{241}$Am, approximately 1-2 mm in diameter. Subsequently, this spot is pressed between 2 layers of this foil, spun over a metal ring and fixed in place. The metal ring was then cut down to be 25mm in diameter, compatible with the source holder in the DIRAC setup. A schematic of the finalized product is shown in figure 4.19 together with a cross-section of a source. The foil in question is thick enough to contain the americium while thin enough to let alpha particles through with minimal energy loss. In the end, 4 such sources were procured with requested activities of 100, 500, 1000 and 4000 Bq.

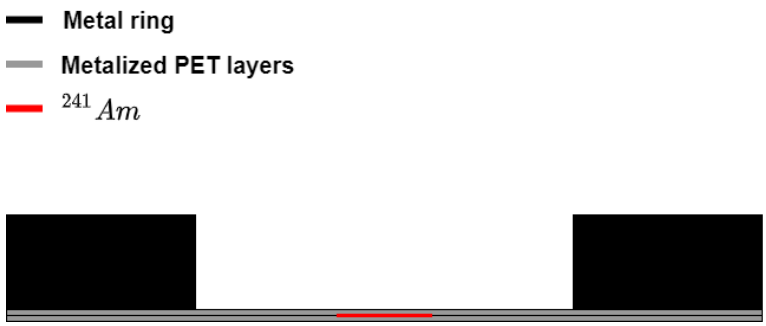


Figure 4.19: Schematic representation of a source manufactured with a liquid solution.

While ideal for all irradiation purposes, these sources do have a large error margin on their activity. The manufacturer of the liquid americium solution set a ±15% margin on the activity in the liquid. Moreover, the pipette used to create the droplets also has an uncertainty of ±5% added on top of possible human error. Due to these uncertainties, it was deemed necessary to fully characterize the activity. Ideally, these measurements

would take place in the ASET but by the time these sources were acquired, it was transported to another facility. This left the COSY chamber which was used in its stead.

Source and detector are positioned very close to each other in this small vacuum chamber, just like in the ASET. This means that any human or systematic error when measuring the distance would have large repercussions on the obtained activity. Furthermore, the design also makes a reliable distance measurement challenging to obtain. To avoid dealing with the geometry of the setup, a different approach was chosen. Efficiencies would instead be obtained by first making a measurement with the calibration source. By using its now known activity and using equation 4.3, the geometric efficiency can be obtained and thus also the distance. Using these distances and the previously used code, relative activities can be calculated without the need to rely on human measurement.

First, an approximate measurement of the distance was taken, giving $\sim 5mm$. Since the geometry of the droplets while drying is not known, it was approximated by a uniform circular source with a radius of $1mm$ compared to the calibration source with a Gaussian distributed activity of $\sigma = 1.75mm$. Error margins on the geometric efficiency of the droplet were obtained by varying the distance between 4.8-5.2 mm and approximating the drop as a uniform circular source of radius 0.5-1.5 mm. By then using equation 4.7 once more, the activity is found. Results are listed in table 4.4.

Table 4.4: Activities of the liquid sources relative to

| Source | Activity $[Bq]$ |
|---|---|
| $'100'Bq$ Source | $88.6^{+7.0}_{-6.5}$ |
| $'500'Bq$ Source | $423^{+32}_{-30}$ |
| $'1000'Bq$ Source | $954^{+72}_{-67}$ |

The listed activities are not absolute activities measured individually but rather activities relative to the original measurement with the calibration source. This means that any inaccuracies in this measurement will have a large effect, as can be seen in their uncertainties. All obtained activities are lower than what was requested. Assuming that the measurement for the calibration source is reliable, this is probably due to a systematic error in the liquid source or production method.

Later in the experimental campaign, it was deemed necessary to use an even stronger source than the three that were discussed now. A 4000 Bq source was commissioned and delivered yet no time for alpha spectroscopy remained. It was assumed that the lower activity from the three other sources came from the production process. The activity for the 4000 Bq source was hence estimated by taking the average of the three others following $\langle A^i_{measured}/A^i_{intended}\rangle \cdot 4000 = 3583^{+275}_{-257}$ Bq.

### 4.4.2 Energy Loss of Alpha Particles in $^{241}$Am Sources

Up to this point, only alpha particles travelling in a straight line through a vacuum were discussed. During experiments, however, they will have to pass through the PET film and aluminium layer of the sources. In later dosimetry experiments, another layer of 1.27mm of air will have to be traversed as well before hitting their target. To know how much energy is deposited in the targets, it is imperative to know how much energy the particles lose while traversing these materials.

First, the energy straggle of the particles was simulated in the Stopping Range of Ions in Matter (SRIM) software package [43]. This is a widely used software that can accurately simulate the behavior of ions in matter and has a large library of target materials to choose from. These materials can also be layered to create more complex systems like in the case of the liquid sources. An example simulation can be seen in figure 4.20 where 10000 alpha particles were simulated while travelling through the metalized film and 5 mm's of air.

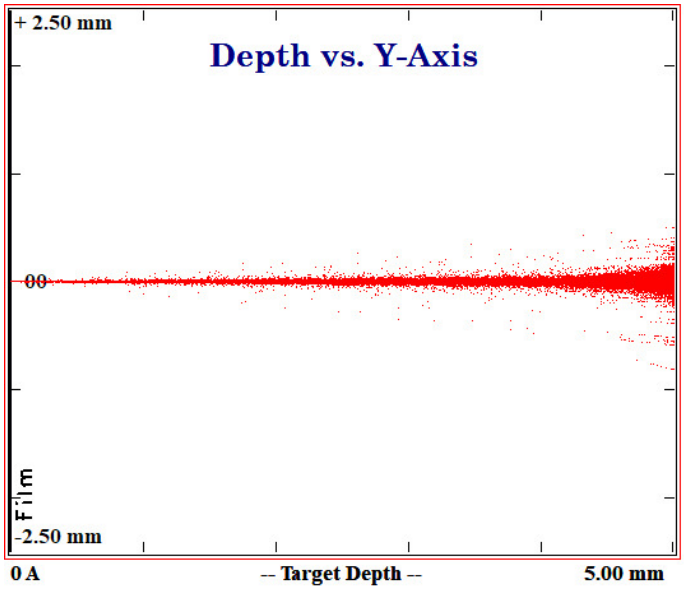


Figure 4.20: Simulation of 10000 alpha particles travelling through a metalized foil and layer of air.

To supplement simulations, spectra were obtained from all three manufactured $^{241}$Am sources and compared to the calibration source. The spectra obtained with this source for calibration purposes are shown in figure 4.21.

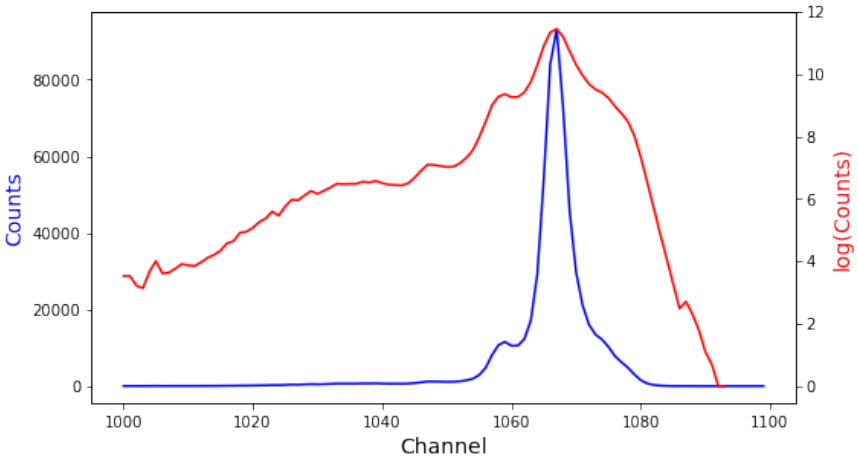


Figure 4.21: Spectrum of the calibration source, measured in the COSY chamber. Both a linear and logarithmic scale is shown.

In order to obtain information on the energy, a calibration must first be performed to convert channel numbers to energy values. This calibration was done by fitting the 3 main peaks of $^{241}$Am and mapping the obtained values to literature. A linear fit through the obtained points is often an excellent way to do this.

Unlike in e.g. gamma-spectroscopy, peaks obtained from alpha particles are not Gaussian. It can be illustrated by looking at the logarithmic plot of the spectrum shown in red on the same figure. On the high energy side of the main peak, there are excess counts due to alpha-electron summing but then a sharp drop. On the low energy side, however, a large tail of counts trailing behind their peaks is present. This effect is caused by the non-active surface or 'dead layer' of the detector that particles have to traverse before exciting electron-hole pairs. Depending on the angle by which these particles enter the dead layer, they lose varying amounts of energy which results in energy straggling. This straggling is thus the cause for the trail of counts on the low-energy side.

Due to these effects, a Gaussian fit is inappropriate. Typically, a so-called 'Crystal Ball function' is used instead. Often used to model various loss effects, this function consists of a Gaussian modified with a low energy tail. The form of which is shown in equation 4.8

$$f(x; N, \alpha, n, \mu, \sigma) = N \cdot \begin{cases} \exp(-\frac{(x-\mu)^2}{2\sigma^2}) & for\ \frac{x-\mu}{\sigma} > -\alpha \\ A \cdot (B - \frac{x-\mu}{\sigma})^{-n} & for\ \frac{x-\mu}{\sigma} \leq -\alpha \end{cases} \tag{4.8}$$

Where

$$A = (\frac{n}{|\alpha|})^n \cdot \exp(-\frac{|\alpha|^2}{2})$$
$$B = \frac{n}{|\alpha|} - |\alpha|$$

Crystal Ball functions are divided into 2 parts, the first of which is identical to a typical Gaussian. N represents the amplitude, $\mu$ the centroid of the peak and $\sigma$ the standard

deviation. As soon as the point on the low energy side of the peak is reached where $x - \mu < -\alpha \cdot \sigma$ or the position corresponding to $\alpha$ times the standard deviation, the tailing effect is described. Here, n describes the magnitude of this tail where smaller values of n correspond to larger tails. This leaves 5 fitting parameters to take into account, namely $N, \alpha, n, \mu$ and $\sigma$.

The obtained spectrum in figure 4.21 contains many displaced counts due to the effect of alpha-electron summing. Since $^{241}$Am is a pure alpha emitter, these electrons do not come from the nucleus and are therefore not to be confused with beta-particles. Instead, they originate from 2 other sources: the Auger effect and internal conversion. The former effect happens when a vacancy occurs in an electron shell and it is filled by an electron from a higher orbital. The released energy is mostly converted into gamma rays but it is also possible that the energy is transferred to an outer shell electron. It is subsequently ejected from the atom and is called an Auger electron. Internal conversion on the other hand happens when electrons interact with the nucleus instead. If the wave function of an electron overlaps with a nucleus in an excited state, it can couple to this energy level. When the nucleus de-excites, this energy is then transferred directly to the electron which is subsequently emitted from the atom. This effect is most common among inner shell electrons and is often followed up by the Auger effect due to the created vacancy in an inner shell. The most common electron emissions in the decay of $^{241}$Am are listed in table 4.5.

Table 4.5: Electron emission origins in the decay of $^{241}$Am

| Origin and Shell | Energy range [$keV$] | Absolute Intensity [%] |
|---|---|---|
| AU L | 6.1-22.2 | ≈35 |
| CE L | 3.9-8.7 | 12.5 |
| CE L | 10.8-15.6 | 17.4 |
| CE M | 20.6-22.7 | 2.2 |
| CE L | 21.0-25.8 | 9.0 |
| CE M | 27.5-29.5 | 4.4 |
| CE L | 37.1-41.9 | 13.8 |
| CE M | 37.7-39.8 | 2.4 |
| CE M | 53.8-55.9 | 1.5 |

Most emitted electrons have energies of approximately ≈4-23keV with an appreciable amount emitted in higher energies. Trying to fit all these emissions separately would result in unrealistic amounts of fitting parameters. Instead, it was decided to try and account for these effects with their own Crystal Ball functions. The LMfit package was chosen for this task [44].

Fitting 6 Crystal Ball functions through the data still gives a lot of fitting parameters and the need to constrain them. For example, the standard deviations of the main peaks were fixed to each other since they would experience similar broadening effects. The end result is shown in figure 4.22.

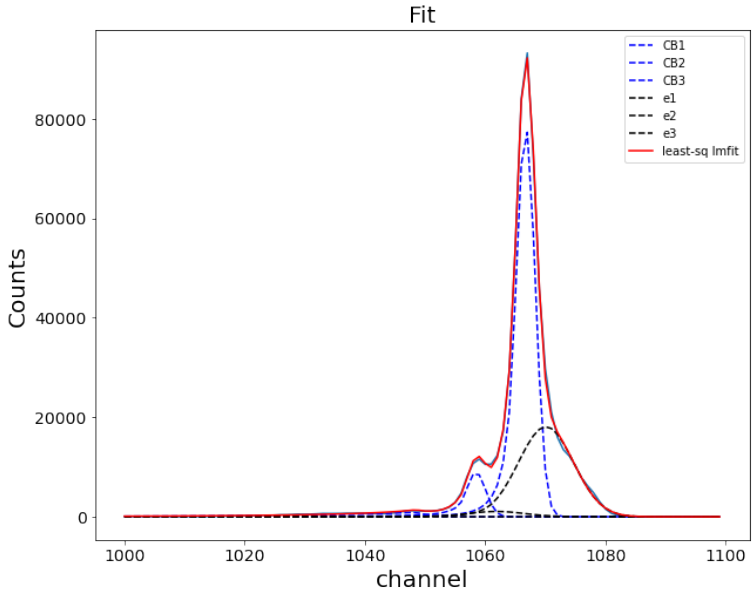


Figure 4.22: Fit of the 3 $^{241}$Am peaks with electron summing modelled separately.

The LMfit package first accepts starting values and constraints on these values. It will then start varying them in an attempt to reach the ideal fit given the constraints. Values for the parameters and their uncertainties are obtained by minimization of the $\chi^2$-function through the data.

The fit shown in figure 4.22 is not ideal, certainly on the high energy side. Not taking the summing into account, however, would result in larger standard deviations for the peak and possibly shifted positions. Electron summing can be avoided by using a vacuum chamber where the source can be positioned further from the detector. Geometric efficiency scales following $1/\mathrm{d}^2$ while the chance to detect particles in coincidence scales by $1/\mathrm{d}^4$. Unfortunately, this option was not available when making these measurements.

Giving the electron summing their own Crystal Ball functions, gave the best overall fit. Nevertheless, it is an unrealistic representation since e.g. the electron peaks overlap significantly with the americium peaks, even beyond their centroids. Instead, it was decided to not model the electrons separately but to add an energy tail to the high-energy side of the Crystal Ball function as well. This resulted in a modified function, the form of which is given in equation 4.9.

$$f(x;N,\alpha,n,\mu,\sigma,\beta,m) = N \cdot \begin{cases} \exp(-\frac{(x-\mu)^2}{2\sigma^2}) & for\ \frac{x-\mu}{\sigma} > -\alpha,\beta \\ A\cdot(B-\frac{x-\mu}{\sigma})^{-n} & for\ \frac{x-\mu}{\sigma} \leq -\alpha \\ C\cdot(D-\frac{x-\mu}{\sigma})^{-m} & for\ \frac{\mu-x}{\sigma} \leq -\beta \end{cases} \tag{4.9}$$

Where

$$A = (\frac{n}{|\alpha|})^n \cdot \exp(-\frac{|\alpha|^2}{2}) \qquad B = \frac{n}{|\alpha|} - |\alpha|$$

$$C = (\frac{m}{|\beta|})^m \cdot \exp(-\frac{|\beta|^2}{2}) \qquad D = \frac{m}{|\beta|} - |\beta|$$

This modification adds a tail to the high-energy side of the Gaussian peak that behaves identically to the tail from a normal Crystal Ball function. To make sure that the result would be as accurate as possible, the form of these tails was fixed among all 3 peaks during the fit.

The positions of the centroids obtained with this fit, their uncertainties and their theoretical energy values are displayed in table 4.6. The less intense the peak, the greater the uncertainty. Especially in the case of the least intense one which is heavily influenced by the tails of the larger peaks and its own electron summing effect. Now that the positions of the centroids are known, a linear fit can be made by plotting it against energy values obtained from literature. Parameters of the obtained fit can subsequently be used to calibrate the energy spectrum. This fit and the spectrum on a calibrated energy scale are shown in figure 4.23.

Table 4.6: The obtained channels, uncertainties and their corresponding literature values.

| Obtained Channels | Literature Values $[keV]$ |
|---|---|
| $1047.77 \pm 1.83$ | 5388.0 |
| $1058.51 \pm 0.37$ | 5442.8 |
| $1066.78 \pm 0.03$ | 5485.6 |

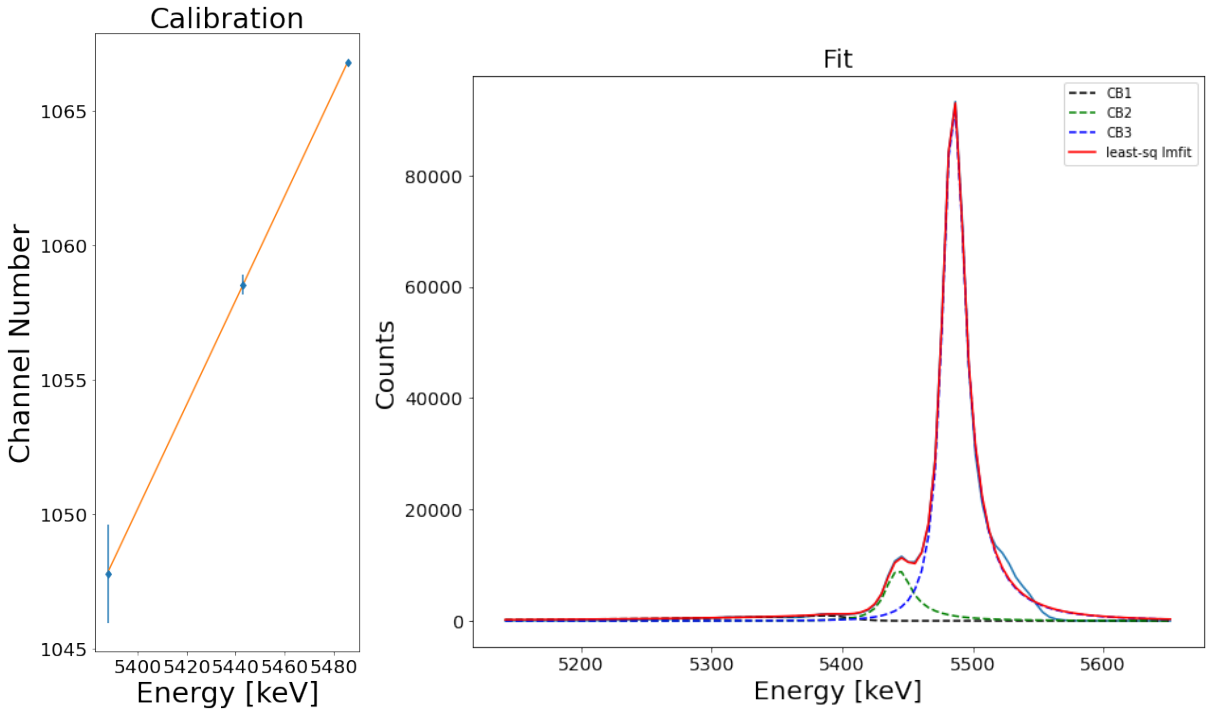


(a) (b)

Figure 4.23: (a): Calibration fit with the obtained centroid values from the fit. (b):The fit with a calibrated energy scale. The 3 peaks of $^{241}$Am are indicated separately.

After calibration was performed, spectra of the 3 liquid $^{241}$Am sources were analyzed.

The foil that the particles have to traverse causes significant energy straggling. It can be compared to the dead layer of a detector but on a much larger scale than is typically the case with modern detectors. The effect is so severe that the separate peaks completely disappear as shown in figure 4.24. This is no problem however as calibration is no longer the goal of these measurements. Instead, it is the extent of energy loss and energy straggling through the metalized foil. To this end, alpha decay spectra of the liquid $^{241}$Am sources were measured in both vacuum and air.

Since the peaks can't be distinguished anymore, it was decided to fit them with a single Crystal Ball function. The peak of this fit can then be used to give an estimate of how much energy is lost compared to the main peak of the calibration source. SRIM simulations were made of the ions travelling through the foil and an optional 5mm of air to complement these measurements. The end results are listed below in table 4.7. Unfortunately, SRIM doesn't offer any built-in options to model a source or detector. Instead, the particles originate from a point source and are fired at a set incidence angle through the layers. This is of course not realistic for this setup, but it does provide a good reference for energy straggling. 10.000 particles were simulated this way and the mean energy loss through the foil was obtained.

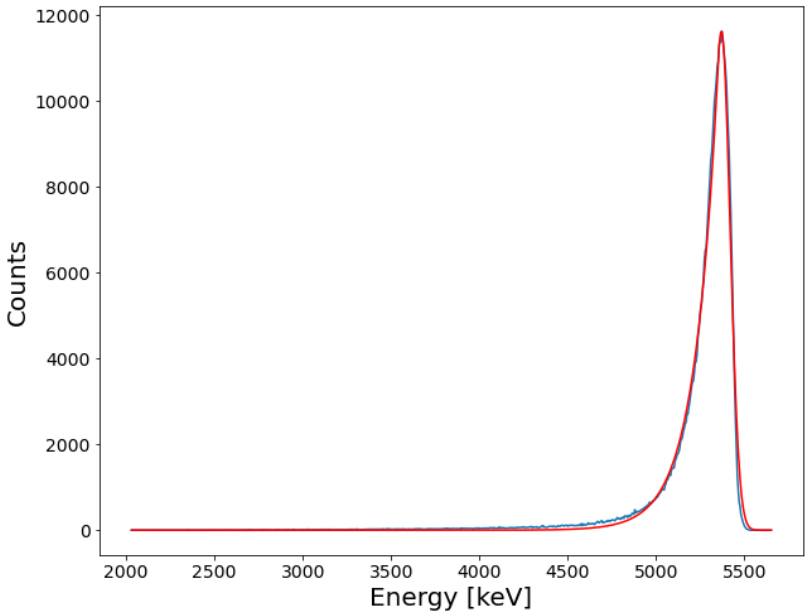


Figure 4.24: Spectrum of the '500' Bq liquid source in vacuum.

Table 4.7: Energy peaks of liquid $^{241}$Am sources. Note that the SRIM data is from perpendicularly fired particles with an optional 5mm of air. Energy straggle compares the lost energy with the main peak of $^{241}$Am.

| Source | Peak in vacuum $[keV]$ | Energy straggle $[keV]$ |
|---|---|---|
| SRIM | 5255.97 | $229.59 \pm 0.12$ |
| '100' Bq Source | $5355.75 \pm 0.74$ | $129.81 \pm 0.75$ |
| '500' Bq Source | $5370.60 \pm 0.49$ | $114.96 \pm 0.50$ |
| '1000' Bq Source | $5160.59 \pm 1.01$ | $324.97 \pm 1.02$ |

| Source | Peak in air $[keV]$ | Energy straggle $[keV]$ | Energy straggle air-vacuum $[keV]$ |
|---|---|---|---|
| SRIM | 4797.34 | $688.22 \pm 0.12$ | $548.63 \pm 0.17$ |
| '100' Bq Source | $4743.41 \pm 3.68$ | $742.15 \pm 3.68$ | 612.34±3.76 |
| '500' Bq Source | $4756.28 \pm 3.45$ | $729.28 \pm 3.45$ | 614.32±3.48 |
| '1000' Bq Source | $4584.23 \pm 3.07$ | $901.33 \pm 3.07$ | 576.36±3.23 |

There are 3 notable phenomena in this data. First of all, the particles from the '1000' Bq source lose noticeably more energy in the metalized foil. When this source was delivered, it was reported that there was a manufacturing mistake resulting in an imperfection of the foil. Most probably, this is the direct cause of this extra energy loss. A picture of this source in the DIRAC holder is shown in figure 4.25 for illustration purposes. Secondly, the particles don't seem to lose as much energy in vacuum as predicted by SRIM but lose more in air. To understand this, it is important to remember that energy calibration was done with particles that also lose energy before being detected. Energy lost exiting the source and traversing the dead layer of the detector cause peaks to be calibrated at a higher energy compared to the actual particles during measurements. In air, SRIM's limitation to perpendicularly fired particles then, makes them lose less energy on average.

Figure 4.25: '1000' Bq source in DIRAC source holder.

With energies of 5.35+ MeV, if manufactured correctly, these sources have the same

profile as shown in previous simulations such as figure 4.8. Combined with the confocal microscope data which shows cells sedimenting within the first 30 μm of a gel. It can be concluded that alpha particles from the $^{241}$Am sources do indeed have the energy required to reach cells in a gel sample and to deposit meaningful amounts of energy in said cells. In the next section, the analysis of cell irradiation experiments will be discussed after which results will be presented in section 4.6.

## 4.5 Image Analysis

The previous sections have shown the feasibility of the in vitro irradiation of cells with an external source. Simulations combined with the characterization of the sources and confocal microscope data show that the cells absorb significant doses from the alpha particles in the DIRAC setup. Because of the half-life of $^{225}$Ac, only 706.4 Bq remained on the foil when the first experiment was performed on 25/02/2022. This is the activity at which simulations were performed as shown in image 4.12. Due to the rapidly decaying activity, foil M171 was used exclusively for the first cell irradiations. The findings of these and later experiments will be discussed in section 4.6. Here, the process by which these results were obtained will be explained.

After preparation of the gel in one of the petri dish covers, the sample is inserted into the DIRAC setup. Insertion of the source and irradiation follows after which the sample is incubated. When it is deemed ready for imaging, it is stained with two different dyes. The first of which is the same calcein-AM dye from section 4.3 with excitation and emission maxima of 496 and 516 nm respectively. Since this dye only becomes fluorescent in metabolically active cells, dead cells won't emit light under this wavelength. The second dye is Ethidium Homodimer-1 which is a weakly fluorescent dye until bound to DNA. The absorption spectrum has a peak wavelength of 528 nm while the peak wavelength of its emission spectrum is 617 nm. It is thus excited under exposure to green light and then fluoresces in the red part of the visible spectrum. This dye can not permeate through the membrane of living cells and thus only becomes fluorescent when bound to the DNA of dead cells. More specifically, cells that have died due to programmed cell death or apoptosis. The excitation and emission spectra of both dyes are shown in figure 4.26.

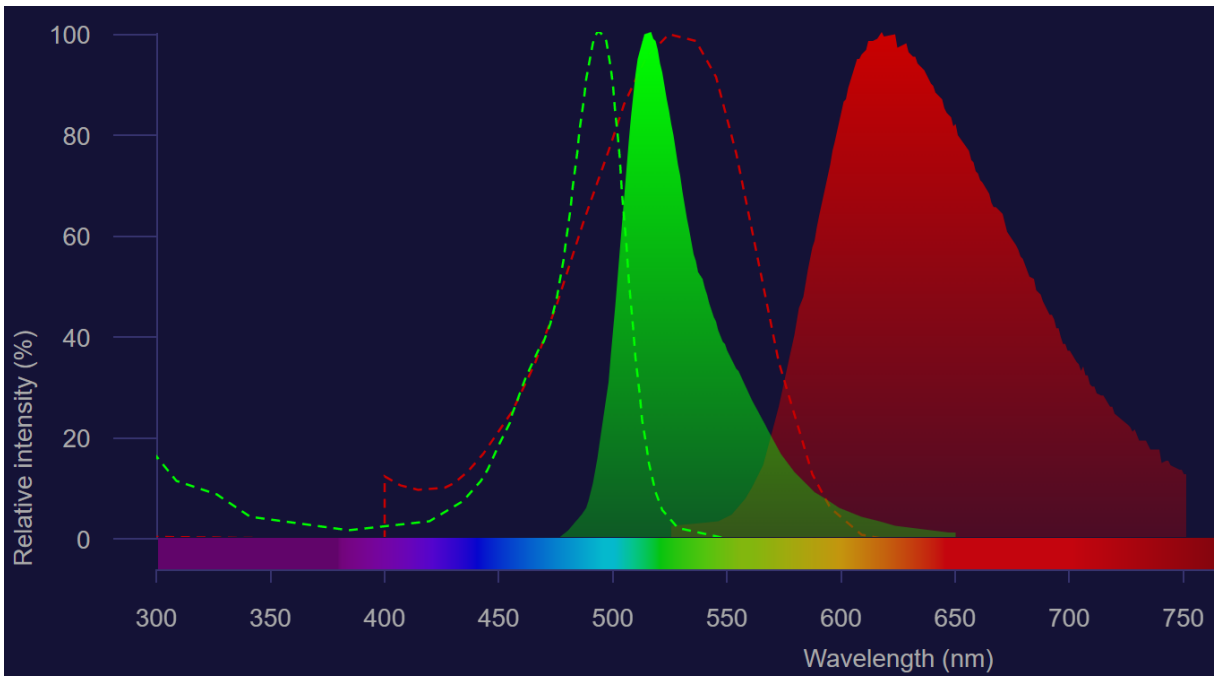


Figure 4.26: Excitation and emission spectra in dotted and full lines respectively. Calcein-AM is displayed in green while Ethidium-Homodimer is displayed in red [45].

After staining, the dyes are given time to metabolize and permeate through the gel for 30 minutes. Afterwards, fluorescent microscopy takes place by shining green and blue light onto the sample. A schematic of how this process works is shown in figure 4.27 This light originates from an X-Cite Exacte fluorescence lamp that passes through a band-pass filter in order to produce desired wavelengths. Three filters are present in the Olympus IX81 microscope. First, the band-pass filter for the fluorescence lamp, then a dichroic mirror which serves as a high-pass filter for emission to block out light from the lamp used in excitation. Finally, a band-gap filter for the emitted light. The ranges of used filters are listed in table 4.5.

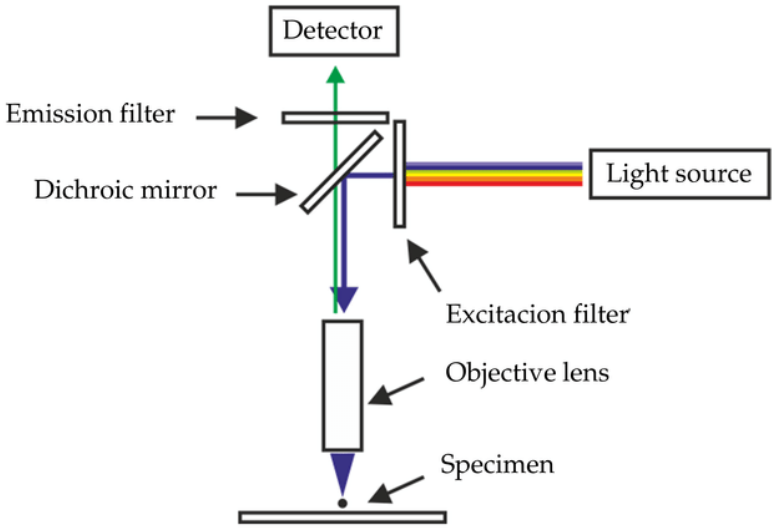


Figure 4.27: Fluorescence microscopy scheme used in imaging [46].

Table 4.8: Wavelength ranges of the various filters used in fluorescence microscopy.

| Filter | Calcein-AM (blue light) [nm] | Ethidium-homodimer (green light) [nm] |
|---|---|---|
| Excitation Filter | 460-495 | 530-550 |
| Dichroic mirror | 505-$\infty$ | 570-$\infty$ |
| Emission filter | 520-550 | 572.5-647.5 |

Under the green light, only dead cells can be seen because the wavelengths used for excitation fall completely out of the range for calcein-AM as shown in figure 4.26. Under the blue light, on the other hand, light from both dyes is detected. Ethidium homodimer also excites under the blue wavelengths and its weak emission in the lower wavelengths passed through the emission filter. Because precise positioning of the microscope over the gel was not possible, imaging was performed on arbitrary regions in the center of a sample. Two images of each region were recorded illuminated with blue and green light respectively. Because dead cells also fluorescence under blue light, however, several steps have to be undertaken before the images are suitable for counting cells. All of these were performed in the ImageJ-Fiji software package, which is specifically tailored for biological-image processing[47]. The first step involves overlapping both images of a region in an RGB picture with separate channels. Dead cells are assigned to red and the alive cells are assigned to green. The result is an image as shown in figure. 4.28a. Next, brightness and contrast values are adjusted for both red and green channels until alive and dead cells are clearly visible and distinguishable from one another as shown in figure 4.28b. The difference between the dyes can also be observed, with the calcein-AM dye showing the outlines of the entire cell while the ethidium-homodimer only shows the nucleus where DNA is located.

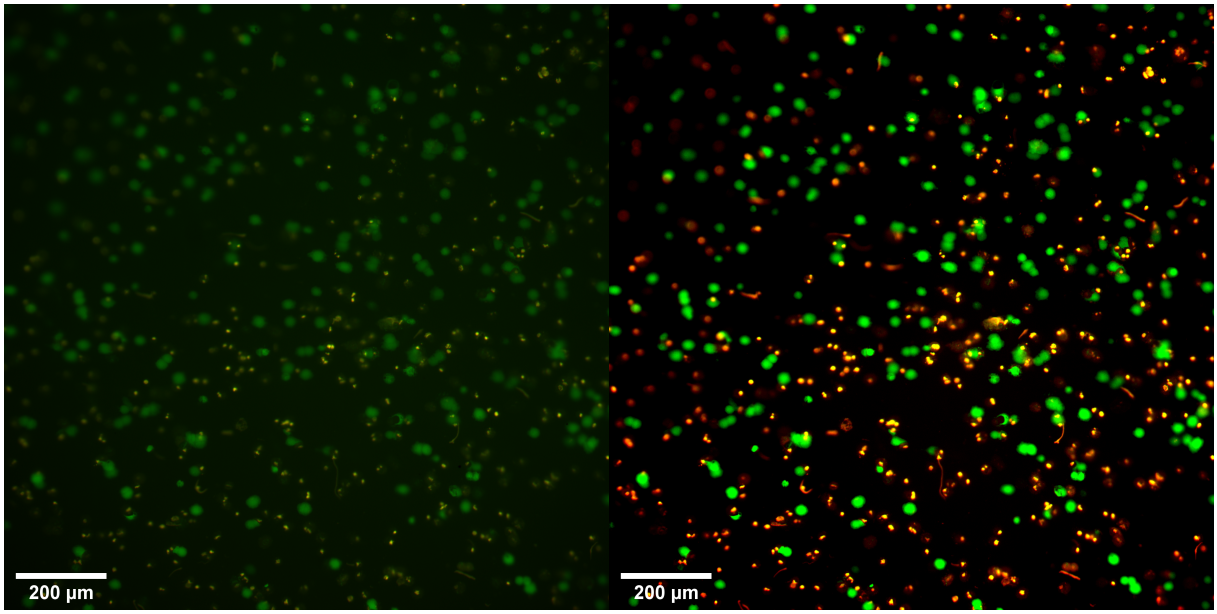


(a) (b)

Figure 4.28: (a) Raw images after microscopy, overlapped with green for alive and red for dead cells (b) Image with adjusted brightness and contrast values to make the cells distinguishable from one another.

Both channels in processed pictures like Figure 4.28b undergo an automated background

subtraction with the built-in rolling ball algorithm of ImageJ-Fiji. Afterwards, they are overlapped to create a single composite RGB picture. These images are now ready for a color threshold, where a selection of the image can be made based on RGB values. An example of such a selection for live cells is shown in figure 4.29a. Everything not included in this selection is deleted from the image which is then converted to a black/white 8-bit image format. The reason for this is that the boundaries of cells in such a threshold can overlap. This is especially true for the alive cells that emit fluorescent light in a larger area. Since cell counting is done per shape, many live cells would not be included in the tally if these overlapping cells aren't separated. This is why the built-in 'watershed' function is used to draw lines between these cells. Examples of the end result after applying this function are shown in figure 4.29b. It can only be applied to 8-bit images, however, hence the conversion.

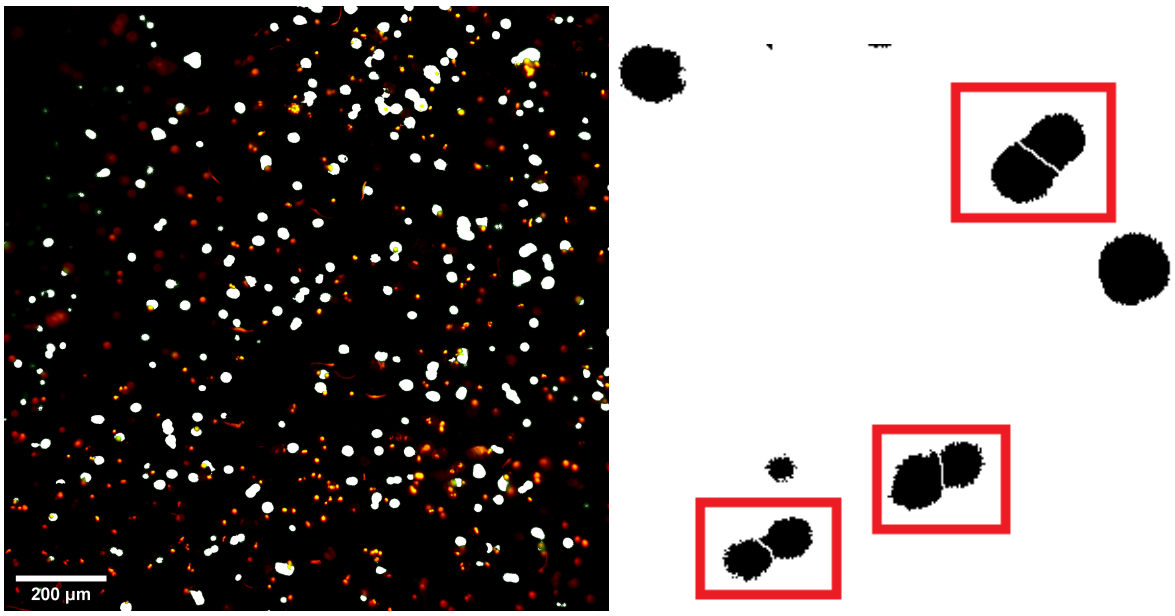


(a) (b)

Figure 4.29: (a) Color tresholding for live cells shown in white(b) Examples of cells separated by the watershed function outlined in red.

After the watershed function, the automated cell counter of ImageJ-Fiji is used to find the number of cells in the picture. The end result is then confirmed by eye to make sure counting was performed correctly. This color thresholding is then repeated for the dead cells as well and the entire process is performed for each image that was taken for a certain sample. Afterwards, the amount of live and dead cells in all pictures is summed to obtain a dead/live percentage for the sample. Since it is a Poisson process, statistical errors are calculated assuming that the number of dead and alive cells is given by the Poisson distribution.

All the images taken for this work were manually processed by the author. To remove as much human bias as possible, macros were written to perform all steps automatically except for one. The step that could not be automated was the brightness/contrast adjustment. Before refrigeration was added to the protocol, sedimentation quality differed significantly between samples. Brightness values depend on this sedimentation as well as

how much time the dyes had to interact with the cells and other environmental factors. This meant that in between experiments, pictures don't necessarily need the same adjustments for analysis. To respond to this problem, a random selection of images was given from both well and badly sedimented samples to 2 other people with experience in image processing. The results from cell counting after the adjustments by these two people and the author are displayed in table 4.5.

Table 4.9: Results of counting cells over 5 images. brightness/contrast values were chosen by the author and 2 others to test for human bias. Pictures 1,2 and 3 are from well sedimented samples while pictures 4 and 5 are from badly sedimented ones.

| Picture | Live cell counts by Author | Person 1 | Person 2 |
|---|---|---|---|
| 1 | 601±25 | 598±24 | 599±24 |
| 2 | 492±22 | 494±22 | 492±22 |
| 3 | 449±21 | 455±21 | 451±21 |
| 4 | 828±29 | 801±28 | 798±28 |
| 5 | 115±11 | 120±11 | 114±11 |
| Picture | Dead cell counts by Author | Person 1 | Person 2 |
| 1 | 173±13 | 173±13 | 174±13 |
| 2 | 158±13 | 155±12 | 160±13 |
| 3 | 69±8 | 67±8 | 69±8 |
| 4 | 50±7 | 50±7 | 50±7 |
| 5 | 101±10 | 99±10 | 103±10 |

From these figures, it seems that human bias has minimal impact on the obtained values. It was hence decided to not include uncertainties from these effects and use the Poisson statistical error instead. With all steps in the cell irradiation experiments thoroughly discussed, results will now be presented in section 4.6.

## 4.6 Results From Cell Irradiation Experiments

Over the course of the first experimental campaign for the DIRAC setup, 17 batches were imaged for a total of 61 samples. Originally, these were performed with 2 samples at a time. One for irradiation and one control sample. Three major setbacks were encountered in the form of foil M171 being rendered unusable and the entire cell line dying out twice. Over the course of the campaign, extra petri dish covers were procured so 5 samples could be made at once. The source also changed from foil M171 to the $^{241}$Am sources characterized in section 4.4. An overview of all experiments and their conclusion is shown in figure 4.30. This figure serves only as context for the results to be presented. Due to difficulties in the development of a suitable protocol and the cell lines dying out, only 8 out of 17 batches resulted in a successful experiment. The other 9 had to be discarded due to most or all of the control sample dying out.

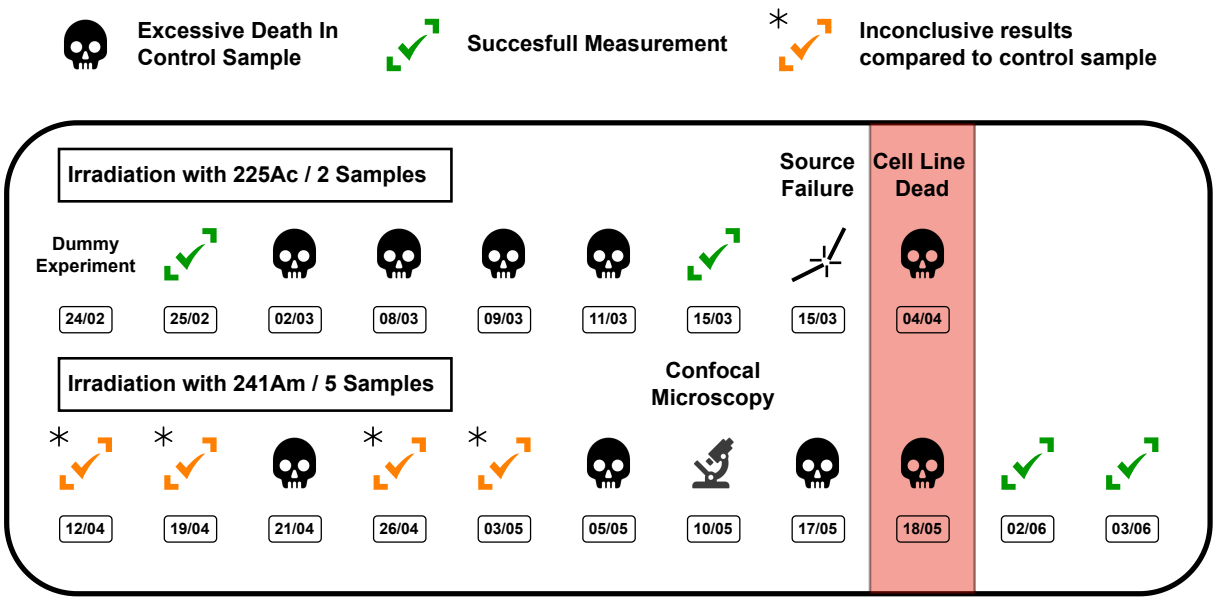


Figure 4.30: Overview of all cell irradiation experiments performed during the first measuring campaign of the DIRAC setup. Major events are indicated as well as the general conclusion from an experiment.

As explained in section 4.5, cells were counted from pictures taken of arbitrary positions in the centre of a sample. This was done because the dose received by cells is heavily reliant on their location. Cells located at the edge receive a lower dose, especially in the case of $^{241}$Am sources as shown in figures 4.8 and 4.12. After all live and dead cells are counted, they are summed and a death/live percentage is calculated. The raw data of which is shown in figure 4.31a. To understand the possible impact of radiation on these percentages, the cell death in irradiated samples has to be compared to their control. This excess death, defined as the difference between an irradiated sample and its control is shown in figure 4.31b.

Experiments for the 8 batches shown in these figures were performed in 3 different ways. Batch 1 and 2 were irradiated with foil M171 for 3 hours. From the coincidence measurements, $^{225}Ac$ activity on the foil was 706.4 and 291.0 Bq for batches 1 and 2 respectively. Batches 3 through 6 feature 2 irradiated samples (2h-1h) each with the 1 kBq $^{241}Am$ source. Batches 7 and 8 then, were prepared and irradiated at the same time with the 4kBq source for 2 hours. They were then imaged at varying times after irradiation.

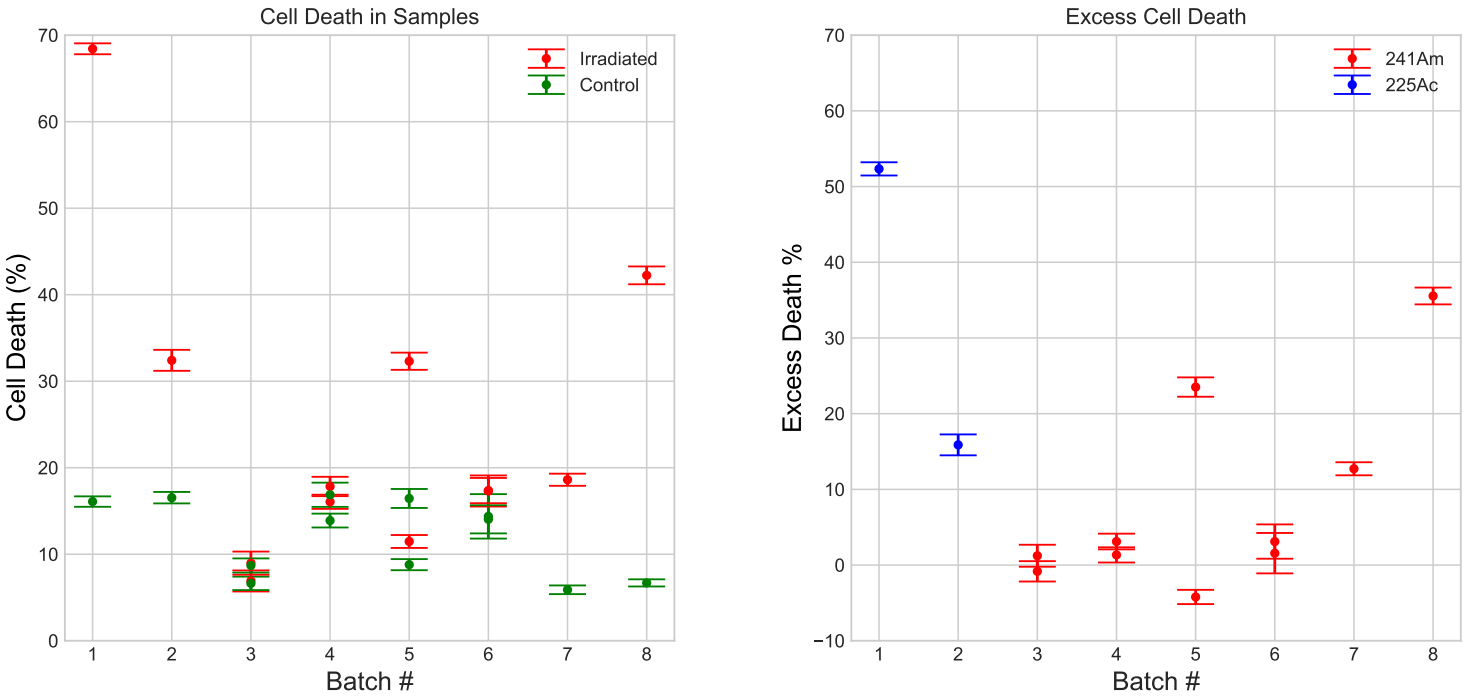


(a) (b)

Figure 4.31: (a) Raw data on cell death of all imaged samples from successful experiments. (b) Excess death in irradiated samples compared to their control sample. Experiments with $^{241}$Am and $^{225}$Ac indicated separately.

From figure 4.31b, 5 batches show statistically significant cell death. Namely batches 1,2,5,7 and 8. However, batch 5 was characterized by faulty preparation, resulting in gels with unstable 3d-matrices and bad sedimentation. The sample irradiated for 2 hours in this batch showed less cell death than its control while the sample irradiated for 1 hour shows significant excess death. Since the effect of the preparation on cell death is difficult to determine, this batch is excluded from further discussion. Leaving batches 1,2,7 and 8.

In a recent review paper, possible mechanisms for cell death by alpha radiation were discussed [2]. Pathways that are relevant for in vitro radiation include:

- Double Strand Breaks (DSB) in DNA located in the nucleus of a cell
- Clustered DNA damage, defined as two or more modifications per helix turn
- Membrane damage leading to the release of fatty acids
- Damage to cell organelles

Because of the cell-impermeable nature of the ethidium-homodimer dye, it only stains cells that have undergone apoptosis or programmed cell death. When faced with DNA damage, a cell will first go into a cell cycle arrest. This means the cell pauses its natural cycle to divide and reproduce. Natural DNA-repair mechanisms will then attempt to fix

any damage done by radiation. If unsuccessful, the cell will undergo apoptosis. Subsequent degradation of the cell membrane will allow the ethidium-homodimer dye to stain the DNA of the dead cell. This process can take hours if not days and is dependent on cell and radiation types. Alpha particles are particularly well suited to induce DNA damage because of their high linear energy transfers. This allows the radiation to overcome the hydrogen bonds in DNA and possibly cause DSB or clustered DNA damage. To investigate how long it takes for apoptosis to set in after induced radiation damage, excess death can be plotted against the time in between irradiation and imaging. The result is shown in figure 4.32a.

Not a single sample that was imaged less than 5 hours after irradiation showed statistically significant cell death. Batches 1,2,7 and 8 on the other hand, which were imaged at least 17 hours later, all showed an excess of cell death in the irradiated samples. This result seems to lead to the conclusion that in vitro, radiation-induced apoptosis takes several (5+) hours at the very least to be observable. Moreover, the number of cells undergoing apoptosis rises over time as an increase could be observed in samples imaged 24 and 42 hours after irradiation. It is hence likely that many cells in batches 3 through 6 have undergone radiation-induced damage, yet it can't be observed because of the restrictions of the used dye.

To test this hypothesis, batches 7 and 8 were prepared simultaneously and both were irradiated for 2 hours with the 4 kBq $^{241}$Am source coupled to a control sample. Additionally, a sample was prepared and immediately incubated to test possible environmental influence on cell death. The sample for batch 7 was then imaged 24.5 hours later and the sample for batch 8 was imaged 42 hours after irradiation together with the control that was incubated from the start. All three control samples were consistent over time with $5.9 \pm 0.5\%$, $6.7 \pm 0.4\%$ and $6.9 \pm 0.5\%$ cell death for batch 7, 8 and immediately incubated control respectively. A large increase in cells that underwent apoptosis is observed over time with $18.6 \pm 0.7\%$ cell death after 24.5 hours and $42.2 \pm 1.0\%$ cell death after 42 hours.

All samples from batches 7 and 8 were made and irradiated under identical conditions. Furthermore, control samples show only a marginal increase in cell death over time compared to a clear response in irradiated samples. This leads to the conclusion that samples do indeed need at least several hours to days before significant apoptosis can be observed. However, further experiments need to be conducted to characterize this behavior as well as to determine when cell death saturates.

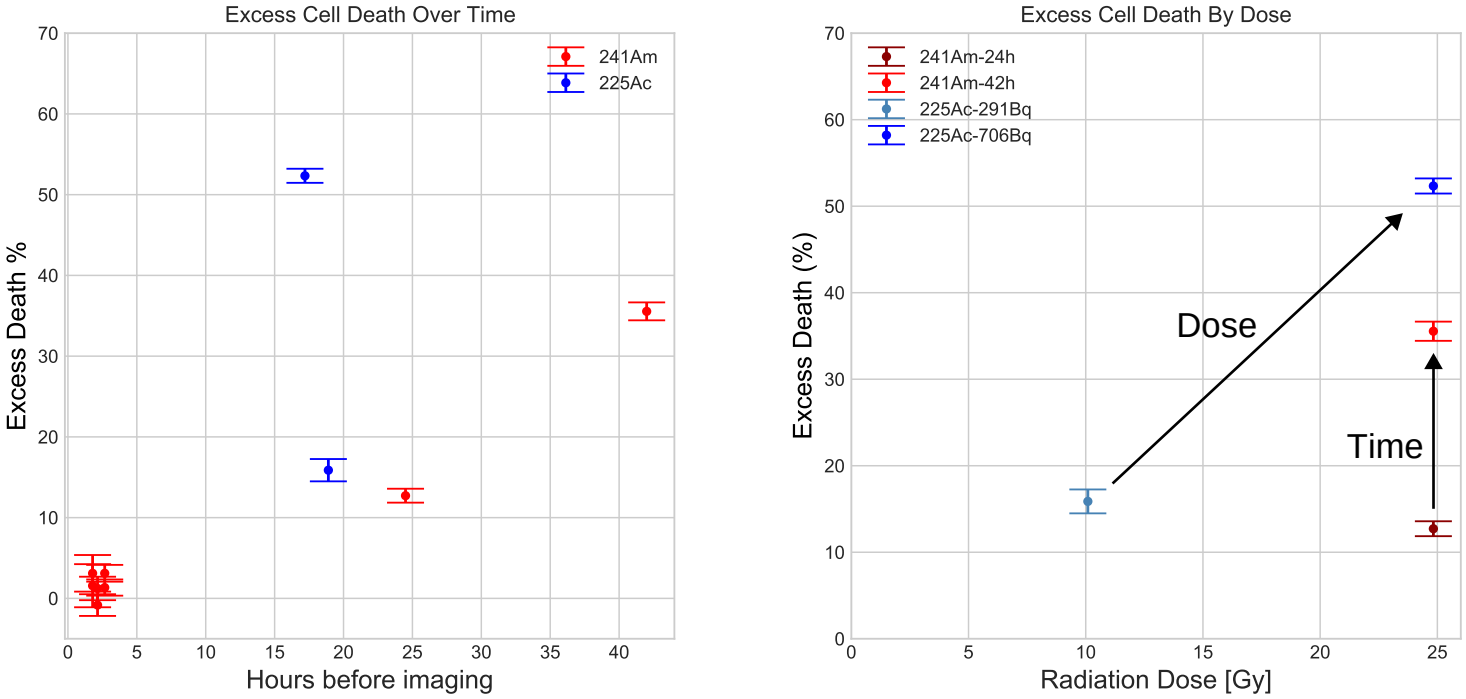


(a) (b)

Figure 4.32: (a) Excess death plotted against time in between irradiation and imaging (b) Excess death plotted against received dose in Grays. The legend displays time in between irradiation and imaging for $^{241}$Am samples and the activity on foil M171 at time of irradiations for $^{225}$Ac samples.

Samples with insufficient time in between irradiation and imaging will be excluded from the discussion from this point. When looking at the four relevant experiments, they can also be plotted against the received dose in Grays as shown in image 4.32b. These doses were obtained by averaging energies from the simulations in section 4.3. Because images for analysis are taken in the centre of a sample, averages were taken in a circle of radius 2 mm. Moreover, because of the results from confocal microscopy, only the radiation deposited in the second 10 µm layer is considered.

Two phenomena can be observed in image 4.32b. On one hand, both $^{225}$Ac batches were irradiated for 3 hours and imaged roughly at the same time after irradiation. However, significantly higher cell death was observed with increasing dose. On the other hand, there is the already discussed increase in cell death over time in the $^{241}$Am sources. Less cell death seems to be observed in $^{241}$Am samples compared to similar doses with $^{225}$Ac irradiation. This is probably an interplay caused by limitations in the simulations, the higher penetrating power of $^{225}$Ac daughters and the effect of recoiling daughters being present in the gel, even after it has been taken out of the setup. This once again warrants future investigation.

In conclusion, radiation-induced death was observed in multiple samples which serves as a proof of concept for the DIRAC setup. However, sufficient time is needed (5+ hours)

in between irradiation and imaging before statistically significant apoptosis can be observed. To get reliable estimates of this cell death, further investigation is warranted to determine the time at which saturation is reached. Furthermore, future experiments will have to be conducted to confirm these preliminary results and to characterize the effects of time and dose on samples.

# Chapter 5

# Conclusions & Future Prospects

The goal of the research presented in this work was to gain insight into the promising medical applications of the radionuclide $^{225}$Ac. To this end, 2 major goals were laid out and achieved. The first was to investigate the purity of a foil with implanted, laser-ionized and mass separated $^{225}$Ac from CERN-MEDICIS. This was done to determine whether accelerator-based production routes for the isotope could achieve the purity necessary for medical application. The second goal was to develop a setup for the in vitro irradiation of cancer cells with alpha emitters. This endeavour culminated in the 'Direct IRradiation with Alphas on Cells' or DIRAC setup which underwent extensive testing. Proof of concept for this setup as well as valuable insight was gained during its first experimental campaign.

To investigate the purity of MEDICIS foil M171, it was characterized using $\gamma$-$\gamma$ coincidence measurements and alpha spectroscopy. The coincidence measurements served the purpose of obtaining $^{225}$Ac activity on the foil. Despite the relatively low activity for coincidences, multiple data points were obtained which yielded a satisfactory result in agreement with gamma-spectroscopy performed in MEDICIS. This result was then used in conjunction with alpha spectroscopy over various weeks to determine the suppression factor of $^{227}$Ac. A preliminary result obtained with a first-order approximation yielded an activity of 0.80 Bq or 0.00000058% of the total activity. A suppression well below the maximal advised ratio of 0.01% was thus achieved[15]. This leads to the conclusion that laser-ionized and mass-separated $^{225}$Ac yields a product with sufficient suppression of $^{227}$Ac for medical applications.

Properties of collagen hydrogels were exploited to make cell samples, susceptible to alpha particles. A new setup was designed and built to utilize these samples and to study the effects of alpha radiation on cells. Baptized as DIRAC, it was used to irradiate HeLa cancer cells with sources of $^{225}$Ac and $^{241}$Am. Simulations in Geant4 served the purpose of understanding the behavior of radiation in this setup. These simulations were then compared to live-death assays from irradiated hydrogel samples with cancer cells suspended near the gel-air interface. A clear response of the cells to alpha particles was observed, resulting in excess death compared to control samples. This response increased with dose and time after irradiation. A proof of concept for the setup was obtained as a result. Moreover, to the knowledge of the author, DIRAC is the first-ever setup designed to perform irradiations with alpha particles on cells suspended in a hydrogel.

Despite the promising preliminary results, further investigation is needed. Firstly, more studies are needed to understand the effect of incubation time following irradiation and before performing microscopy. Then, dose-escalation and dose rate studies can be performed to understand the radiobiology of direct irradiation with alpha particles. The presented research was also constrained to one cell line and a cell-impermeable dye to measure radiation damage. It is advised that in the future, irradiations are expanded to other cell lines as well. Additionally, other staining methods should be employed to measure DNA damage and cell arrest as well besides apoptosis. Hydrogel-based cell irradiation could potentially provide a much-needed, accessible research method to study the radiobiological effects of alpha particles in vitro. To this end, procurement of a new sample from MEDICIS is warranted for further cell irradiation experiments. Not only would it lead to valuable radiobiological data, but the presented purity could be verified as well.

In conclusion, this work achieved both its goals and provided valuable insight and tools for the development of targeted alpha therapy.

# Bibliography


[1] Prac. "Xofigo EMEA-H-A20-1459 - PRAC Assessment Report". In: (2018). URL: www.ema.europa.eu/contact.

[2] Jean Pierre Pouget and Julie Constanzo. "Revisiting the Radiobiology of Targeted Alpha Therapy". In: *Frontiers in Medicine* 8 (July 2021), p. 1125. ISSN: 2296858X. DOI: 10.3389/FMED.2021.692436/BIBTEX.

[3] M. Lassmann and U. Eberlein. "Targeted alpha-particle therapy: imaging, dosimetry, and radiation protection". In: *Annals of the ICRP* 47.3-4 (Oct. 2018), pp. 187–195. ISSN: 1872969X. DOI: 10.1177/0146645318756253. URL: https://journals.sagepub.com/doi/10.1177/0146645318756253.

[4] Attila Keresztes, Attila Borics, and Csaba Tömböly. "Therapeutic and diagnostic radiopharmaceuticals #". In: (2015).

[5] *Radiotherapy in skin disease : Joseph Belot : Free Download, Borrow, and Streaming : Internet Archive*. URL: https://archive.org/details/radiotherapyins00belogoog.

[6] Xiufang Tian et al. "The evolution of proton beam therapy: Current and future status". In: *Molecular and Clinical Oncology* 8.1 (Nov. 2018), p. 15. ISSN: 2049-9450. DOI: 10.3892/MCO.2017.1499. URL: /pmc/articles/PMC5772792/%20/pmc/articles/PMC5772792/?report=abstract%20https://www.ncbi.nlm.nih.gov/pmc/articles/PMC5772792/.

[7] Thomas N. Seyfried and Leanne C. Huysentruyt. "On the Origin of Cancer Metastasis". In: *Critical reviews in oncogenesis* 18.1-2 (2013), p. 43. ISSN: 08939675. DOI: 10.1615/CRITREVONCOG.V18.I1-2.40. URL: /pmc/articles/PMC3597235/%20/pmc/articles/PMC3597235/?report=abstract%20https://www.ncbi.nlm.nih.gov/pmc/articles/PMC3597235/.

[8] *Colourful Nuclide Chart*. URL: https://people.physics.anu.edu.au/~ecs103/chart/.

[9] A. K. Jain, R. Raut, and J. K. Tuli. "Nuclear Data Sheets for A = 225". In: *Nuclear Data Sheets* 110.6 (June 2009), pp. 1409–1472. ISSN: 0090-3752. DOI: 10.1016/J.NDS.2009.04.003.

[10] Katerina T. Xenaki, Sabrina Oliveira, and Paul M.P. van Bergen en Henegouwen. "Antibody or Antibody Fragments: Implications for Molecular Imaging and Targeted Therapy of Solid Tumors". In: *Frontiers in Immunology* 8.OCT (Oct. 2017). ISSN: 16643224. DOI: 10.3389/FIMMU.2017.01287. URL: /pmc/articles/PMC5643388/%20/pmc/articles/PMC5643388/?report=abstract%20https://www.ncbi.nlm.nih.gov/pmc/articles/PMC5643388/.

[11] Ashok Kumar Jain et al. "Nuclear Data Sheets for A = 221". In: *Nuclear Data Sheets* 108.4 (Apr. 2007), pp. 883–922. ISSN: 0090-3752. DOI: 10.1016/J.NDS.2007.03.002.

[12] F. G. Kondev et al. "Nuclear Data Sheets for A=217". In: *Nuclear Data Sheets* 147 (Jan. 2018), pp. 382–458. ISSN: 0090-3752. DOI: 10.1016/J.NDS.2018.01.002.

[13] M. S. Basunia. "Nuclear Data Sheets for A = 213". In: *Nuclear Data Sheets* 108.3 (Mar. 2007), pp. 633–680. ISSN: 0090-3752. DOI: 10.1016/J.NDS.2007.02.002.

[14] J. Chen and F. G. Kondev. "Nuclear Data Sheets for A = 209". In: *Nuclear Data Sheets* 126 (May 2015), pp. 373–546. ISSN: 0090-3752. DOI: 10.1016/J.NDS.2015.05.003.

[15] Joao Alberto Osso Junior et al. "NUCLEAR SCIENCES AND APPLICATIONS; DIVISION OF PHYSICAL AND CHEMICAL SCIENCES; RADIOISOTOPE PRODUCTS AND RADIATION TECHNOLOGY SECTION; VIENNA; AUSTRIA". In: ().

[16] Andrew Kyle Henderson Robertson et al. "Development of 225Ac Radiopharmaceuticals: TRIUMF Perspectives and Experiences". In: *Current Radiopharmaceuticals* 11.3 (Apr. 2018), p. 156. ISSN: 18744710. DOI: 10.2174/1874471011666180416161908. URL: /pmc/articles/PMC6249690/%20/pmc/articles/PMC6249690/?report=abstract%20https://www.ncbi.nlm.nih.gov/pmc/articles/PMC6249690/.

[17] Francisco D.C. Guerra Liberal et al. "Targeted Alpha Therapy: Current Clinical Applications". In: *Cancer Biotherapy and Radiopharmaceuticals* 35.6 (Aug. 2020), pp. 404–417. ISSN: 15578852. DOI: 10.1089/CBR.2020.3576/ASSET/IMAGES/LARGE/CBR.2020.3576{_}FIGURE5.JPEG. URL: https://www.liebertpub.com/doi/full/10.1089/cbr.2020.3576.

[18] Soghra Farzipour et al. "Recent Achievements about Targeted Alpha Therapy-Based Targeting Vectors and Chelating Agents". In: *Anti-cancer agents in medicinal chemistry* 22.8 (July 2021), pp. 1496–1510. ISSN: 1875-5992. DOI: 10.2174/1871520621666210727120308. URL: https://pubmed.ncbi.nlm.nih.gov/34315393/.

[19] Mohamed Hegazi et al. "AML-253: Trials in Progress: A Phase I/II Study of Venetoclax and Lintuzumab-Ac225 in Patients with Refractory or Relapsed AML". In: *Clinical Lymphoma, Myeloma and Leukemia* 20 (Sept. 2020), S196. ISSN: 2152-2650. DOI: 10.1016/S2152-2650(20)30742-4. URL: http://www.clinical-lymphoma-myeloma-leukemia.com/article/S2152265020307424/fulltext%20http://www.clinical-lymphoma-myeloma-leukemia.com/article/S2152265020307424/abstract%20https://www.clinical-lymphoma-myeloma-leukemia.com/article/S2152-2650(20)30742-4/abstract.

[20] Clemens Kratochwil et al. "225Ac-PSMA-617 for PSMA-Targeted $\alpha$-Radiation Therapy of Metastatic Castration-Resistant Prostate Cancer". In: *Journal of nuclear medicine : official publication, Society of Nuclear Medicine* 57.12 (Dec. 2016), pp. 1941–1944. ISSN: 1535-5667. DOI: 10.2967/JNUMED.116.178673. URL: https://pubmed.ncbi.nlm.nih.gov/27390158/.

[21] Benedikt Feuerecker et al. “Activity and Adverse Events of Actinium-225-PSMA-617 in Advanced Metastatic Castration-resistant Prostate Cancer After Failure of Lutetium-177-PSMA”. In: *European urology* 79.3 (Mar. 2021), pp. 343–350. ISSN: 1873-7560. DOI: 10.1016/J.EURURO.2020.11.013. URL: https://pubmed.ncbi.nlm.nih.gov/33293081/.

[22] B. Zielinska et al. “An improved method for the production of Ac-225/Bi-213 from Th-229 for targeted alpha therapy”. In: *Solvent Extraction and Ion Exchange* 25.3 (May 2007), pp. 339–349. ISSN: 07366299. DOI: 10.1080/07366290701285108.

[23] C. Apostolidis et al. “Cyclotron production of Ac-225 for targeted alpha therapy”. In: *Applied radiation and isotopes : including data, instrumentation and methods for use in agriculture, industry and medicine* 62.3 (Mar. 2005), pp. 383–387. ISSN: 0969-8043. DOI: 10.1016/J.APRADISO.2004.06.013. URL: https://pubmed.ncbi.nlm.nih.gov/15607913/.

[24] O. D. Maslov, A. V. Sabel’nikov, and S. N. Dmitriev. “Preparation of 225Ac by 226Ra($\gamma$,n) photonuclear reaction on an electron accelerator, MT-25 microtron”. In: *Radiochemistry* 48.2 (Mar. 2006), pp. 195–197. ISSN: 10663622. DOI: 10.1134/S1066362206020184.

[25] Charlotte Duchemin et al. “CERN-MEDICIS: A Review Since Commissioning in 2017”. In: *Frontiers in Medicine* 8 (July 2021), p. 1068. ISSN: 2296858X. DOI: 10.3389/FMED.2021.693682/BIBTEX.

[26] “PRISMAP The European medical isotope programme: PRoduction of high purity Isotopes by mass Separation for Medical Application”. In: (). URL: https://ec.europa.eu/info/law/better-regulation/have-your-say/initiatives/12154-Europe-s-Beating-Cancer-Plan.

[27] V. M. Gadelshin et al. “MELISSA: Laser ion source setup at CERN-MEDICIS facility. Blueprint”. In: *Nuclear Instruments and Methods in Physics Research, Section B: Beam Interactions with Materials and Atoms* 463 (Jan. 2020), pp. 460–463. ISSN: 0168583X. DOI: 10.1016/J.NIMB.2019.04.024.

[28] Michael Heines. “Mass separation of 225 Ac for medical applications: First proof of principle at CERN-MEDICIS”. In: (2020).

[29] *MichaelHeines · GitHub*. URL: https://github.com/MichaelHeines.

[30] Miroslav Morháč et al. “Background elimination methods for multidimensional coincidence $\gamma$-ray spectra”. In: *Nuclear Instruments and Methods in Physics Research Section A: Accelerators, Spectrometers, Detectors and Associated Equipment* 401.1 (Dec. 1997), pp. 113–132. ISSN: 0168-9002. DOI: 10.1016/S0168-9002(97)01023-1.

[31] Leslie D Galloway et al. “Bateman Equation Adaptation for Solving and Integrating Peak Activity into EPA ELCR and Dose Models”. In: (2020). URL: www.osti.gov.

[32] “Simulating decay chains using spreadsheets”. In: (2012). URL: http://wordpress..

[33] Filip Kondev et al. “Nuclear Data Sheets for A = 227”. In: *Nuclear Data Sheets* 132 (Feb. 2016), pp. 257–354. ISSN: 0090-3752. DOI: 10.1016/J.NDS.2016.01.002.

[34] C. Maples. “Nuclear data sheets for A = 223”. In: *Nuclear Data Sheets* 22.2 (Oct. 1977), pp. 243–274. ISSN: 0090-3752. DOI: 10.1016/S0090-3752(77)80007-0.

[35] Kristina Bannik et al. "Radiobiological effects of the alpha emitter Ra-223 on tumor cells". In: *Scientific Reports 2019 9:1* 9.1 (Dec. 2019), pp. 1–11. ISSN: 2045-2322. DOI: 10.1038/s41598-019-54884-7. URL: https://www.nature.com/articles/s41598-019-54884-7.

[36] Xiaolin Wang et al. "Nanostructured Dense Collagen-Polyester Composite Hydrogels as Amphiphilic Platforms for Drug Delivery". In: *Advanced Science* 8.7 (Apr. 2021), p. 2004213. ISSN: 2198-3844. DOI: 10.1002/ADVS.202004213. URL: https://onlinelibrary.wiley.com/doi/full/10.1002/advs.202004213%20https://onlinelibrary.wiley.com/doi/abs/10.1002/advs.202004213%20https://onlinelibrary.wiley.com/doi/10.1002/advs.202004213.

[37] S. Agostinelli et al. "Geant4—a simulation toolkit". In: *Nuclear Instruments and Methods in Physics Research Section A: Accelerators, Spectrometers, Detectors and Associated Equipment* 506.3 (July 2003), pp. 250–303. ISSN: 0168-9002. DOI: 10.1016/S0168-9002(03)01368-8.

[38] C. D. Nesaraja. "Nuclear Data Sheets for A = 241". In: *Nuclear Data Sheets* 130 (Dec. 2015), pp. 183–252. ISSN: 0090-3752. DOI: 10.1016/J.NDS.2015.11.004.

[39] Xiyi Chen et al. "Second harmonic generation microscopy for quantitative analysis of collagen fibrillar structure". In: *Nature Protocols 2012 7:4* 7.4 (Mar. 2012), pp. 654–669. ISSN: 1750-2799. DOI: 10.1038/nprot.2012.009. URL: https://www.nature.com/articles/nprot.2012.009.

[40] Qianqian Li et al. "Fluorescence of Nonaromatic Organic Systems and Room Temperature Phosphorescence of Organic Luminogens: The Intrinsic Principle and Recent Progress". In: *Small* 14.38 (Sept. 2018), p. 1801560. ISSN: 1613-6829. DOI: 10.1002/SMLL.201801560. URL: https://onlinelibrary.wiley.com/doi/full/10.1002/smll.201801560%20https://onlinelibrary.wiley.com/doi/abs/10.1002/smll.201801560%20https://onlinelibrary.wiley.com/doi/10.1002/smll.201801560.

[41] Periklis Pantazis et al. "Second harmonic generating (SHG) nanoprobes for in vivo imaging". In: *Proceedings of the National Academy of Sciences of the United States of America* 107.33 (Aug. 2010), pp. 14535–14540. ISSN: 00278424. DOI: 10.1073/PNAS.1004748107/SUPPL{_}FILE/SM03.MOV. URL: www.pnas.org/lookup/suppl/.

[42] N. D. Priest et al. "Pattern of uptake of americium-241 by the rat skeleton and its subsequent redistribution and retention: implications for human dosimetry and toxicology". In: *Human toxicology* 2.1 (1983), pp. 101–120. ISSN: 0144-5952. DOI: 10.1177/096032718300200109. URL: https://pubmed.ncbi.nlm.nih.gov/6840786/.

[43] James F Ziegler, M D Ziegler, and J P Biersack. "SRIM – The stopping and range of ions in matter (2010)". In: *Nuclear Inst. and Methods in Physics Research, B* 268 (2010), pp. 1818–1823. DOI: 10.1016/j.nimb.2010.02.091. URL: www.SRIM.org..

[44] Matthew Newville et al. "LMFIT: Non-Linear Least-Square Minimization and Curve-Fitting for Python". In: (Sept. 2014). DOI: 10.5281/ZENODO.11813. URL: https://zenodo.org/record/11813.

[45] *Fluorescence SpectraViewer*. URL: https://www.thermofisher.com/order/fluorescence-spectraviewer?SID=srch-svtool&UID=SVehDNA#!/.

[46] Tomáš Majtner and David Svoboda. "Comparison of 3D texture-based image descriptors in fluorescence microscopy". In: *Lecture Notes in Computer Science (including subseries Lecture Notes in Artificial Intelligence and Lecture Notes in Bioinformatics)* 8466 LNCS (2014), pp. 186–195. ISSN: 16113349. DOI: 10.1007/978-3-319-07148-0{_}17.

[47] Johannes Schindelin et al. "Fiji: an open-source platform for biological-image analysis". In: *Nature Methods 2012 9:7* 9.7 (June 2012), pp. 676–682. ISSN: 1548-7105. DOI: 10.1038/nmeth.2019. URL: https://www.nature.com/articles/nmeth.2019.

# Appendices

# Appendix A

# Confocal Microscopy Settings

Image: **Image 2**

Size: **46,14 MB**

File Location:

Start Time: **10/05/2022 15:10:36.858**

End Time: **10/05/2022 15:13:24.793**

Total Exposures: **44 (1 channels, 44 frames)**

Data from: **LAS X 3.5.7.23225**

| |
|---|
| Settings used for the imaging of collagen. |

### Dimensions

| Dimension | Logical Size | Physical Length | Start Position | End Position | Pixel Size / Voxel Size |
|---|---|---|---|---|---|
| X | 1024 | 228.66 µm | 0 µm | 228.66 µm | 0.224 µm |
| Y | 1024 | 228.66 µm | 0 µm | 228.66 µm | 0.224 µm |
| Z | 44 | 86.06 µm | 0 µm | 86.06 µm | 2.001 µm |

### Channels

| LUT | Resolution | Min | Max | STED: DetectorMode / Huygens saturation factor / Wavelength |
|---|---|---|---|---|
| Red | 8 | 0 | 255 | --- / --- / --- |

### Time Stamps:

| Frame (Show All) | Relative Time (s) | Absolute Time (h:m:s.ms) | Date |
|---|---|---|---|
| 1 | 0,000 | 15:10:36.858 | 10/05/2022 |
| 44 | 167,935 | 15:13:24.793 | 10/05/2022 |

### Confocal Settings

| Name | Value |
|---|---|
| Rotator Angle | 0 ° |
| Scan Mode | xyz |
| Scan Direction X | Bidirectional |
| Scan Speed | 400 Hz |
| Version Number | 15 |
| StagePosX | 67,478.46 µm |
| StagePosY | 37,550.01 µm |
| ZPosition | 3,318.2 µm |
| IsSuperZ | 0 |
| Magnification | 25 |
| ObjectiveName | Fluotar VISIR 25x/0.95 WATER |
| Immersion | WATER |
| Numerical Aperture | 0.95 |

| | |
|---|---|
| RefractionIndex | 1.33 |
| Zoom | 2.03 |
| Pinhole | 20 µm |
| PinholeAiry | 358.02 mAU |
| EmissionWavelength for PinholeAiry Calculation | 580 nm |
| FrameAverage | 1 |
| LineAverage | 3 |
| FrameAccumulation | 1 |
| Line_Accumulation | 1 |
| IsUserSettingNameSet | 0 |
| IsRoiScanEnable | 0 |

## Filter Wheels / Other Motorized Devices

| **Device Name** | **Filter Name/Position** |
|---|---|
| RLD Blocking Slider | SP 800 |
| Excitation Beam Splitter | Substrate |
| Galvo Slider | Galvo X Normal |
| Multi Function Port | SP 815 |
| Notch FW 2 | OPO SP 800 |
| Polarization FW | Empty |
| Galvo Resonant Pan | Galvo X Pan Center |
| Target Slider | Target Park |
| X2 Lens Changer | CS2 UV Optics 1 |
| VariableBeamExpander 900nm | Factor: 1.03,  Z Color Correction Offset: 0 |

## Lasers

| **LaserName** | **OutputPower** |
|---|---|
| **OPSL 488** | **On** |
| **OPSL 514** | **On** |
| **MP** | **On , Power: 2,7700 W** |

## Laser Lines

| **Laser Line** | **Intensity** |
|---|---|
| ( 900 nm) | Shutter: on, Intensity: 10.0013% |

## Detectors

| **Name** | **Channel** | **Type** | **Location** | **Active** | **Gain** | **Offset** | **Gate Start** | **Gate End** | **Gate Ref. Wavelength** |
|---|---|---|---|---|---|---|---|---|---|
| HyD-RLD1 | NDD1 | HyD (436nm - 468nm)  Standard mode | RLD | Active | 208.9 | -0.01 | -- Time Gating not supported -- | | |

Image: **Image 1**

Size: **46,14 MB**

File Location:

Start Time: **10/05/2022 15:07:11.656**

End Time: **10/05/2022 15:09:59.591**

Total Exposures: **44 (1 channels, 44 frames)**

Data from: **LAS X 3.5.7.23225**

Settings used for the imaging of cells.

### Dimensions

| Dimension | Logical Size | Physical Length | Start Position | End Position | Pixel Size / Voxel Size |
|---|---|---|---|---|---|
| X | 1024 | 228.66 µm | 0 µm | 228.66 µm | 0.224 µm |
| Y | 1024 | 228.66 µm | 0 µm | 228.66 µm | 0.224 µm |
| Z | 44 | 86.06 µm | 0 µm | 86.06 µm | 2.001 µm |

### Channels

| LUT | Resolution | Min | Max | STED: DetectorMode / Huygens saturation factor / Wavelength |
|---|---|---|---|---|
| Gray | 8 | 0 | 255 | --- / --- / --- |

### Time Stamps:

| Frame (Show All) | Relative Time (s) | Absolute Time (h:m:s.ms) | Date |
|---|---|---|---|
| 1 | 0,000 | 15:07:11.656 | 10/05/2022 |
| 44 | 167,935 | 15:09:59.591 | 10/05/2022 |

### Confocal Settings

| Name | Value |
|---|---|
| Rotator Angle | 0 ° |
| Scan Mode | xyz |
| Scan Direction X | Bidirectional |
| Scan Speed | 400 Hz |
| Version Number | 15 |
| StagePosX | 67,478.46 µm |
| StagePosY | 37,550.01 µm |
| ZPosition | 3,318.2 µm |
| IsSuperZ | 0 |
| Magnification | 25 |
| ObjectiveName | Fluotar VISIR 25x/0.95 WATER |
| Immersion | WATER |
| Numerical Aperture | 0.95 |

| | |
|---|---|
| RefractionIndex | 1.33 |
| Zoom | 2.03 |
| Pinhole | 20 µm |
| PinholeAiry | 358.02 mAU |
| EmissionWavelength for PinholeAiry Calculation | 580 nm |
| FrameAverage | 1 |
| LineAverage | 3 |
| FrameAccumulation | 1 |
| Line_Accumulation | 1 |
| IsUserSettingNameSet | 0 |
| IsRoiScanEnable | 0 |

## Filter Wheels / Other Motorized Devices

| **Device Name** | **Filter Name/Position** |
|---|---|
| RLD Blocking Slider | SP 800 |
| Excitation Beam Splitter | DD 488/552 |
| Galvo Slider | Galvo X Normal |
| Multi Function Port | Substrate |
| Notch FW 2 | Empty |
| Polarization FW | Empty |
| Galvo Resonant Pan | Galvo X Pan Center |
| Target Slider | Target Park |
| X2 Lens Changer | CS2 UV Optics 1 |
| VariableBeamExpander 900nm | Factor: 1.03,  Z Color Correction Offset: 0 |

## Lasers

| **LaserName** | **OutputPower** |
|---|---|
| **OPSL 488** | **On** |
| **OPSL 514** | **On** |
| **MP** | **On , Power: 2,7700 W** |

## Laser Lines

| **Laser Line** | **Intensity** |
|---|---|
| ( 488 nm) | Shutter: on, Intensity: 7.0015% |

## Detectors

| **Name** | **Channel** | **Type** | **Location** | **Active** | **Gain** | **Offset** | **Gate Start** | **Gate End** | **Gate Ref. Wavelength** |
|---|---|---|---|---|---|---|---|---|---|
| PMT 1 | Channel 1 | PMT (494nm - 650nm) | Internal | Active | 600.4 | 0 | -- Time Gating not supported -- | | |

# Appendix B

# Incident Report of Foil M171

# Report on incident concerning Ac-225 source ks-27.

Since 22/02/2022, the Ac-225 source KS-27 has been used for the experiment named CELLRAD, performed in IKS room 00.80. The experiments were always performed with Jake Johnson and Viktor Van Den Bergh present. Precautions described in the risk assessment (in appendix) were followed. Special care was given to contamination monitoring due to working with the open source.

In this experiment the open source is removed from the glass vial, placed in an aluminium source holder which is itself held on a support structure. The source can then be lowered and raised by means of an actuator to sub mm precision. In the experiments performed, the source is placed very close to cells that are suspended in a collagen-based gel that lie flush with a Teflon cover. This cover is placed on top of a petri dish containing cell medium (= sugar, water, collagen). The setup is shown in the figure below.

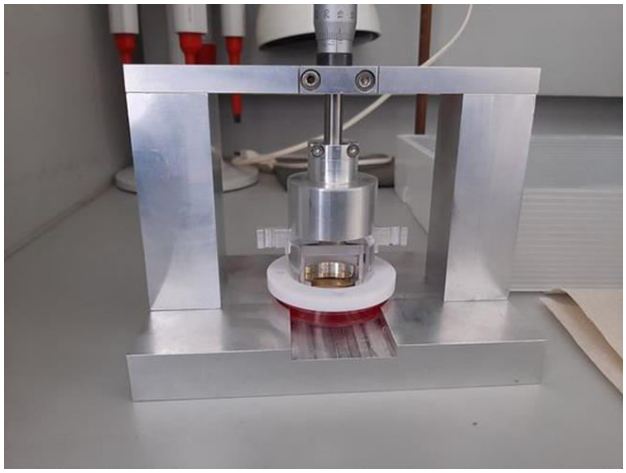

Two times each week since 22/02/22, the source has been placed in such a configuration, irradiating the cells before being removed 3 hours later. The source is then always placed in its glass vial until the following irradiation. No damage of the source was ever observed from 22/02/22 until 15/03/22.

Before performing these experiments, fake sources were placed in the source holder in the configuration described above to test whether the presence of the medium nearby the source could damage the surface and cause unexpected dispersion. The tests showed that the source remained dry and unaffected by its use in the experiment.

Following some recurrent problems with the drying-out of the hydrogel, it was then decided from 11/03/22, that parafilm or clingfilm could be placed around the source holder in order to better control the humidity of the environment and thus avoid the drying of the gel.

In the first instance, the use of parafilm did not affect the source after irradiation, but solved the drying out of the hydrogel problem. Therefore it was decided that the parafilm should be used from thereon in the irradiation experiments. An observation was made after the first use of parafilm that

some pink-coloured medium had condensed on the parafilm interior, and residues were found at the bottom of the setup at the base of the petri dish.

In the second instance of parafilm usage, on 15-03-2022, the parafilm was wrapped more tightly around the source holder, and also blocked the ventilation holes in the Teflon. The source was placed inside the setup by Jake Johnson following the procedure established. At this point it was estimated that the Ac-225 activity of the source was of the order of 50 Bq.

At the end of the 3-hour irradiation, Jake Johnson was not present due to his 21 month evaluation taking place. Viktor Van Den Bergh was in the laboratory. He removed the source foil, and upon doing so, realized that the thin aluminium film in which the source was implanted had been highly damaged. He immediately placed the damaged foil back in the glass vial, and did not leave the room 00.80.

Some minutes later, Wiktoria Wojtaczka arrived, and performed thorough contamination measurements of Viktor's lab-coat, hands, and nearby surface and found nothing. Michael Heines and Hilde de Witte also soon joined and performed contamination measurements around the fume cupboard in room 00.80 and found no obvious spillage or dispersion of the source.

20 minutes later Jake Johnson arrived in the laboratory, and measured the surface of the source, where many counts (30 per second) were still observed on the contamination monitor. The source holder was also inspected, and from visual inspection, it could be seen that a significant quantity of the aluminium had stuck to the source holder surface. Significant alpha activity could also be measured on this surface. Alpha activity could be measured nowhere else in the fume cupboard, nor on the tweezers used for source handling. The source holder was then placed in a zip-lock bag pending HSE antenna advice.

All people present were thoroughly checked for contamination before leaving the room 00.80. None was found with the exception of ~ 1 alpha count / 6 seconds on Viktor Van den Bergh's shoe. This was washed in the sink of the source room as a precautionary measure. The room was then closed and locked.

The following day on 16-03-2022, Ludwig Henderix was informed of the incident, and he and Jake decided that the ks-27 source should no longer be used due to the dispersion of the activity. The source has been deposited in the Actinium-225 waste bucket, still contained in its glass vial.

It is foreseen that the source holder be washed with isopropanol, to remove the adhered radioactive material. The cleaning materials shall then also be placed in the Ac-225 waster container in room 00.80. The source holder shall then be measured for contamination before being re-used for further experiments.

17-03-22.

Report written by Jake Johnson

# Appendix C

# Risk Assessment for The DIRAC Setup

DIENSTEN ALGEMEEN BEHEER
DIRECTIE STAFDIENSTEN ALGEMEEN BEHEER
**DIENST VGM**
WILLEM DE CROYLAAN 58 BUS 5530
3001 LEUVEN, BELGIË

# APPLICATION FORM SPECIFIC RISK ANALYSIS FOR AN EXPERIMENT WITH OPEN RADIOACTIVE SOURCES

*Use this guide to prepare a specific risk assessment for experiments with biological materials.*
*Complete this form in consultation with your HSE Network Contact Radioprotection (RP)[1].*

## 1. Identification of the unit (users)

| | | | |
|---|---|---|---|
| Applicant/contact person: | Jake Johnson | Unit: | IKS |
| Phone: | +32 16 33 06 12 | Warehouse code[2]: | Fill in. |
| E-mail address: | jake.johnson@kuleuven.be | Manager[3]: | Fill in. |
| | | Promotor: | Thomas Elias Cocolios |

| Persons who will initially perform the activity | | |
|---|---|---|
| **Name – first name** | **u-/s-number/…** | **Staff group** |
| Johnson Jake | U0138006 | ■ KU ☐ Student KU ☐ UZ ☐ VIB ☐ External: Fill in. |
| Van den Bergh Viktor | r0629142 | ☐ KU ■ Student KU ☐ UZ ☐ VIB ☐ External: Fill in. |
| Deschaume Olivier | u0079541 | ■ KU ☐ Student KU ☐ UZ ☐ VIB ☐ External: Fill in. |
| Dedroog Lens | u0140738 | ■ KU ☐ Student KU ☐ UZ ☐ VIB ☐ External: Fill in. |
| Carmen Bartic | u0005394 | ■ KU ☐ Student KU ☐ UZ ☐ VIB ☐ External: Fill in. |
| Thomas Cocolios | u0051261 | ■ KU ☐ Student KU ☐ UZ ☐ VIB ☐ External: Fill in. |
| Fill in. | Fill in. | ☐ KU ☐ Student KU ☐ UZ ☐ VIB ☐ External: Fill in. |
| Fill in. | Fill in. | ☐ KU ☐ Student KU ☐ UZ ☐ VIB ☐ External: Fill in. |

## 2. Identification of the experiment

2.1. **Title** (name) (max. 40 characters): CellRad

2.2. **This risk analysis shall include:**

■ a new experiment,

☐ a change/extension of an existing experiment,

- This change/extension concerns (please indicate and describe further in the form):
  - ☐ Premises where the experiment takes place
  - ☐ Agents or devices that generate ionizing radiation
  - ☐ Extension
  - ☐ Other risks: Describe briefly.
- File or reference number previously submitted risk analysis (if known): Fill in.

2.3. **Desired start date** 19/01/2022 **Scheduled finish date:** 31/05/2022

[1] *You can find the members of your local HSE Network via KU Loket > VGM & Ruimtes > Mijn VGM > Mijn VGM-antenne*
[2] *If you do not know the warehouse code, please contact your HSE Network*
[3] *This is the hierarchically responsible person according to the official organization chart.*

## 3. Identification of agents

### 3.1. Description of the radioactive sources used: products and quantities

- Radionuclides used: Ac-225 and daughters, Am-241
- Products: Am-241 source 'coin'. Ac-225 source 'foil'
- Activity per experiment per radionuclide (MBq): uBq / mBq Ac-225, Bq- tens Bq Ac-225, 50Bq Am-241, kBq Am-241
- Purchased activity per radionuclide (MBq): Fill in.

## 4. Description of the experiment and the risk analysis

### 4.1. Description of the actions, techniques and location:

| Number sub-experiment | Description of sub-experiment – actions and techniques (e.g., preparing the samples, carrying out the measurements, storing samples, measurements, …) |
|---|---|
| 1 | Cell preparation and insertion of cells into petri dish irradiation plate |
| 2 | Irradiation of cells with open alpha sources using Cellrad setup |
| 3 | Incubation and fixation of cells. preparation of immunofluorescence microscopy solutions |
| 4 | Performance of 2d immunofluorescence microscopy with widefield microscope |
| 5 | Performance of 3d immunofluorescence microscopy with leica confocal microscope |

| Number sub-experiment | Building | Room | Containment level | Specifications room |
|---|---|---|---|---|
| 1. | 200d | 00.29 | L2 | ☐ own unit<br>■ space allocated to another unit: Soft matter physics |
| 2. | IKS (200d) | 00.80A | Red<br>Chemical c2<br>Radiation: KL2-OB | ■ own unit<br>☐ space allocated to another unit: Fill in. |
| 3. | 200d | 00.29 | L2 | ☐ own unit<br>■ space allocated to another unit: Soft matter physics |
| 4. | 200d | 00.41 | Fill in. | ☐ own unit<br>■ space allocated to another unit: Soft matter physics |
| 5. | 200J | Nanocentre microscopy room | Fill in. | ☐ own unit<br>■ space allocated to another unit: Chemical engineering DPT: SMaRT group |

**Type experiment:**

☐ Binding experiment (adding radioactive material, incubation, separation, measurement)
☐ Commercial experiment (with standard protocol: RIA…)
☐ Radioactive marking (with 125I, 131I, …)
■ Other (specify): Irradiation of non-pathogenic biological material in order to perform micro-dosimetry study,

### 4.2. Frequency experiment execution: ■ Daily

☐ Weekly
☐ Monthly
☐ Less than monthly

4.3. **Add more information essential for performing the risk analysis (e.g., description, photos, reaction sceheme) or refer to an appendix:**

In this experiment, neuroblastoma cells / fibroblasts will be suspended in hydrogel disk ~1cm diameter, prepared in a Teflon holder in room 00.29 200D

The Teflon holder containing hydrogel will be placed on a petri dish (that in some cases may contain agar cell medium) in the room 00.80a (IKS bunker).

The radioactive alpha source ( Am-241 or Ac-225) will be positioned in a source holder, fixed in place by the irradiation setup. The micrometer screw will bring the source into position (~0.5mm above the hydrogel) where it will be held from 1 time of a few seconds to a few minutes before being retracted.

The hydrogel holder will be removed and tested for radioactive contamination.

In the case of no contamination, the hydrogel and holder will be taken back to room 00.29 200D for biological tests.

In the case of contamination, the hydrogel will be left in the fume cupboard and monitored for activity. If no >background radioactivity is detected for repeated subsequent ~15 minute measurements, the hydrogel and holder will be considered uncontaminated and then the hydrogel and holder will be taken back to room 00.29 200D for biological tests. In case of contamination lasting > 1 day, the sample will be considered contaminated with Ac-225 and will be placed in the appropriate waste container. If the Teflon hydrogel holder is contaminated it will be stored in a zip-lock bag and placed behind lead shielding for ~ 2 months for decay. In case of Am-241 contamination, HSE will be notified).

See annex in attachment for PDF drawings of the setup proposed for irradiation.

See below the Ac-225 decay chain where the daughters are what may cause contamination.

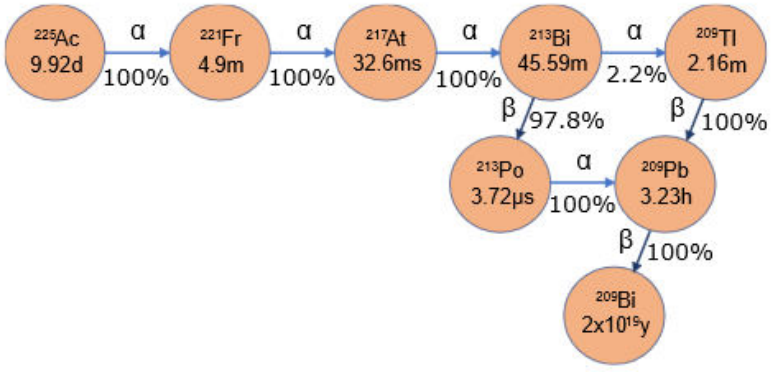


Note that during the irradiations, while alpha particles can penetrate 1mm air with little energy loss, the recoiling nuclei will no longer be ionizing (range in nitrogen <150 um) after this range and should not be implanted in the hydrogel sample in theory.
Note that another risk assessment will be drawn up and submitted for sub experiment 5.

4.4. **Risks associated with the experiment:**

**Risks associated with the use of ionizing radiation:**

☐ Risk of inhalation / inhalation (powders / aerosols / volatile substances)
☐ Chance of splashing
■ Chance of contamination of measuring equipment / devices
☐ Reuse glassware
☐ Transport of radioactive material:
  ☐ inside building or building complex: Describe the measures: Fill in.
  ☐ between KU Leuven buildings (not on public roads): Describe the measures: Fill in.
  ☐ external transport (on public road)
☐ Other: Fill in.

**Other risks associated with the experiment**

☐ Incineration, freezing (☐ high or low temperatures, ☐ cryogenic substances, …)
☐ Implosion, explosion (☐ high pressures, ☐ low pressures, ☐ negative pressure, …)
☐ Fire (☐ ovens, ☐ heating coils, ☐ Bunsen burner, ☐ oil baths …)
☐ Non-ionizing radiation (☐ NMR, ☐ lasers, ☐ UV lamps, ...)
☐ Electrocution (☐ naked contacts, ☐ humid environment, ☐ high powers, ...)
☐ Secluded employment remote room or place.
  Describe the conditions (e.g. with 2 present, dead man's alarm,…): Fill in.
☐ Risk of falling (☐ installations at a height, ☐ in height, ☐ difficult to reach, ...)
☐ Chemical risk: (products: ☐ flammable, ☐ toxic, ☐ carcinogenic,
  ☐ teratogenic, ☐ mutagen, …)
  Specify (name, CAS-nr., concentration, used quantity): Fill in.
☐ Biological risk (☐ pathogenic µ-organisms (specify): Fill in., ☐ GGO (specify host-vector-insert): Fill in.,
  ■ cells (specify type and origin: Neuroblastoma SH-SY5Y / Fibroblast 3T3. Cells stocked in cell lab (00.29, 200D), ☐ blood (specify origin): Fill in., ☐ lab animals (specify species, wild-type/knock-out, ...): Fill in., …)
☐ Gasses: Fill in.
☐ There is a chance that in the event of a serious incident, an independent alarm can **NOT** be given (e.g. use of highly toxic vapors or gases, risk of explosion, presence of suffocating gas, ...)
☐ Other: Fill in.

## 5. Precautions to be applied

*If not all precautions can be applied, the HSE Department advises not to start the activities.*

5.1. **Collective protective equipment**

| **Number sub-experiment[4]:** | **1** | **2** | **3** | **4** | **5** |
|---|---|---|---|---|---|
| Environmental Dosimetry | ☐ | ☐ | ☐ | ☐ | ☐ |
| Safety screen:<br>- Plexi screen | ☐ | ■ | ☐ | ☐ | ☐ |

[4] *Number of the sub-experiment as indicated in section 4.1.*

| | | | | | |
|---|---|---|---|---|---|
| - Lead shielding (wall of lead blocks, lead glass, …)<br>- Other: Fill in. | ☐<br>☐ | ☐<br>☐ | ☐<br>☐ | ☐<br>☐ | ☐<br>☐ |
| Closed system | ☐ | ☐ | ☐ | ☐ | ☐ |
| Fume cupboard | ☐ | ■ | ☐ | ☐ | ☐ |
| Ventilated cupboard | ☐ | ☐ | ☐ | ☐ | ☐ |
| Reactor cabinet | ☐ | ☐ | ☐ | ☐ | ☐ |
| Local extractor | ☐ | ☐ | ☐ | ☐ | ☐ |
| Spatial extractor | ☐ | ☐ | ☐ | ☐ | ☐ |
| Drip tray underneath the installation / liquid waste | ☐ | ☐ | ☐ | ☐ | ☐ |
| Signage (pictograms) | ☐ | ☐ | ☐ | ☐ | ☐ |
| Other: Fill in. | ☐ | ☐ | ☐ | ☐ | ☐ |

## 5.2. **Personal protective equipment**[5]

| **Number sub-experiment**[4]: | **1** | **2** | **3** | **4** | **5** |
|---|---|---|---|---|---|
| General protection: | | | | | |
| - Lab apron / work clothes | ☐ | ☐ | ☐ | ☐ | ☐ |
| - Disposable overshoes | ☐ | ☐ | ☐ | ☐ | ☐ |
| - Personal Dosimeter[6] (to be worn at chest height) | ☐ | ■ | ☐ | ☐ | ☐ |
| - Ring Dosimeter[7] | ☐ | ☐ | ☐ | ☐ | ☐ |
| - Disposable hygiene hair net | ☐ | ☐ | ☐ | ☐ | ☐ |
| - Disposable overall | ☐ | ☐ | ☐ | ☐ | ☐ |
| - Disposable lab coat | ☐ | ☐ | ☐ | ☐ | ☐ |
| - Other: Fill in. | ☐ | ☐ | ☐ | ☐ | ☐ |
| Eye and face protection: | | | | | |
| - Safety glasses | ☐ | ☐ | ☐ | ☐ | ☐ |
| - Global vision safety glasses | ☐ | ☐ | ☐ | ☐ | ☐ |
| - Face shield | ☐ | ☐ | ☐ | ☐ | ☐ |
| - Other: Fill in. | ☐ | ☐ | ☐ | ☐ | ☐ |
| Respiratory protection: | | | | | |
| - Disposable dust mask P1 | ☐ | ☐ | ☐ | ☐ | ☐ |
| - Disposable dust mask P3 | ☐ | ☐ | ☐ | ☐ | ☐ |
| - Disposable hygiene mask / surgical mask | ☐ | ■ | ☐ | ☐ | ☐ |
| - Other: Fill in. | ☐ | ☐ | ☐ | ☐ | ☐ |
| Gloves: | | | | | |
| - Disposable nitrile EN 374 | ☐ | ■ | ☐ | ☐ | ☐ |
| - Disposable vinyl EN 374 | ☐ | ☐ | ☐ | ☐ | ☐ |
| - Nitrile EN 374 | ☐ | ☐ | ☐ | ☐ | ☐ |
| - Cryogenic gloves | ☐ | ☐ | ☐ | ☐ | ☐ |
| - Other: Fill in. | ☐ | ☐ | ☐ | ☐ | ☐ |

[5] *Guidelines on obtaining Personal Protective Equipment (PPE's): via your HSE Network or the website of the HSE Department.*

[6+7] *More info on dosimeters can be found on the website of the HSE Department.*

| | | | | | |
|---|---|---|---|---|---|
| Hearing protection:<br>- Disposable earplugs<br>- Banded earplugs<br>- Ear muffs<br>- Other: Fill in. | ☐<br>☐<br>☐<br>☐ | ☐<br>☐<br>☐<br>☐ | ☐<br>☐<br>☐<br>☐ | ☐<br>☐<br>☐<br>☐ | ☐<br>☐<br>☐<br>☐ |

5.3. **Specific preventative measures:**

- ■ Check for radioactive contamination:
  - ■ immediate measuring by means of a contamination monitor (vb. Geiger-Müller, NaI, …)
  - ☐ indirect measuring by means of rub/wash samples for liquid scintillation counts
- ■ Check operation of the contamination monitor (battery voltage and background signal)
- ☐ Presence of decontamination material
- ■ Check operation of fume cupboard
- ☐ Check glassware for cracks
- ☐ Other: Fill in.

5.4. **Work practices**

- ■ Apply the Code of Good Lab Practice
- ■ Follow the Course Radiation Protection (Basic Training)
  - ☐ Provide internal training and guidance
- ☐ Organization of Purchase and acquisition of radioactive substances via SAP
- ■ Apply precautions when working with radioactive materials
- ■ Organization of selective collection waste - radioactive waste

## 6. Disposal of waste – radioactive waste

6.1. **Indicate the expected waste fractions:**

| **Waste fraction + container**<br>*- Only 1 radionuclide is collected per container (with the exception of $^{3}H$ and $^{14}C$).* | | **Container present** |
|---|---|---|
| Disposable waste<br>$t_{1/2}$ > 180 days and<br>$^{3}H$-$^{14}C$-waste | ☐ Solid flammable: black plastic barrel 30 l | ☐ |
| | ☐ Solid non-combustible: metal bucket 30 l | ☐ |
| | ☐ Liquid scintillation counting vials: blue plastic barrel 30 l | ☐ |
| | ☐ Liquid aqueous and liquid organic: plastic jerrycan 10 l<br>(Collect aqueous waste separately from organic waste.) | ☐ |
| | ☐ Injection needles: needle container and full needle containers in metal bucket 30 l | ☐ |
| | ☐ Animal cadaver of mice and rats: in two separately hermetically sealed polyethylene zip bags and then:<br>- *disposable* in white plastic bucket<br>- *$^{3}H$ and $^{14}C$*: in black plastic container 30 l<br>(The unit provides the polyethylene zip bags.) | ☐<br>☐ |
| Perishable waste<br>$t_{1/2}$ < 180 days | ■ Solid (flammable, non-flammable, filled needle containers): red plastic barrel 50 l | ■ |
| | ☐ Liquid scintillation counting vials: blue plastic barrel 30 l | ☐ |
| | ☐ Liquid aqueous and liquid organic: plastic jerrycan 10 l<br>(Collect aqueous waste separately from organic waste.) | ☐ |

| | | |
|---|---|---|
| | ☐ Animal cadaver of mice and rats: in two separately hermetically sealed transparent plastic bags and then in a black plastic barrel 30 l.<br>(The unit provides the polyethylene zip bags.) | ☐<br>☐ |
| Special waste | ☐ Special waste<br>→ The container and the cost price are specifically determined by the HSE Department. | |

## 7. Measures in special situations

### 7.1. In case of failure and reactivation of utilities (incl. deviation from specifications):

| Utilities | Consequence(s) of failures | Is this a HSE problem: yes/no? | If yes, describe the measures |
|---|---|---|---|
| Electricity | nul | No | Fill in. |
| Ventilation | In case of fume hood failure during irradiation, recoil daughters from semi-open Ac-225 source will no longer be extracted. Experiment will stop immediately and source will be returned to its glass vial to contain the recoil daughters | No | Fill in. |
| Gas supply | nul | No | Fill in. |
| (Cooling)water | nul | No | Fill in. |
| Compressed air | nul | No | Fill in. |
| Inert atmosphere | nul | No | Fill in. |
| Vacuum | nul | No | Fill in. |
| Other: Fill in. | Fill in. | No | Fill in. |

| Utilities | Consequence(s) when reactivating | Is this a HSE problem: yes/no? | If yes, describe the measures |
|---|---|---|---|
| Electricity | Fill in. | Choose Yes/No | Fill in. |
| Other: Fill in. | Fill in. | Choose Yes/No | Fill in. |

### 7.2. Can the experiment continue if the setup is left unattended (= continuous tests)?

■ Not applicable: the setup is never left unattended.

☐ Yes.
In this case, the procedure "Continuous activities - unsupervised" is applied.

☐ No, additional measures are necessary.
Describe the additional measures: Fill in.
In addition, the procedure "Continuous activities - unsupervised" is applied.

7.3. **Is working outside normal working hours allowed?**

- ■ No.
- ☐ Yes. Describe which additional measures have been taken for this (e.g.: ventilation, presence second person, dead man's alarm,… ): Fill in.

7.4. **Describe your procedure for a quick shutdown or the measures you will take when the building is evacuated:**

In case of quick shut-down, the Ac-225 source will be returned to its glass vial, and then placed in its tin. The rest of the experimental setup requires no further security measures.
Standard evacuation procedure will then be followed.

7.5. **Describe the guidelines in case of a spill incident:**

In case of a spill (radioactive contamination), the experimenter will stay in place and attempt to decontaminate by measuring first, then cleansing, and then re-measuring. If decontamination by cleansing does not work, then the contaminated area will be covered and labelled and HSE antenna for IKS will be contacted.

In order to mitigate possibility of spill incident, the experiment will be performed in a shallow-edged box in the fume cupboard.

In case of spill of cell medium, this can be cleansed and then disposed of in the regular waste.

## 8. Conclusion / Comments / Questions

Write down any additional comments or questions here

**Send the completed application / risk analysis form to**
**your HSE Network Coordinator, your supervisor and the HSE Department.**

## 9. Advice HSE Department

*This space is reserved for advice from the HSE Department:*

Institute for nuclear and radiation physics
Celestijnenlaan 200D
3001 LEUVEN, BELGIË
tel. + 32 16 32 72 63
www.kuleuven.be